Changes in the Cation Ordering of Layered O3 $Li_xNi_{0.5}Mn_{0.5}O_2$
During Electrochemical Cycling to High Voltages

by

Hayley Han Li

B.S., Mechanical Engineering
University of California - Berkeley, 2005

Submitted to the Department of Mechanical Engineering
in Partial Fulfillment of the Requirements for the Degree of
Master of Science in Mechanical Engineering

at the

Massachusetts Institute of Technology

February 2007

Signature of Author.....
Department of Mechanical Engineering
January 19, 2007

Certified by .....
Yang Shao-Horn
Assistant Professor of Mechanical Engineering
Thesis Supervisor

Accepted by .....
Lallit Anand
Professor of Mechanical Engineering
Chairman, Department of Graduate Committee

Changes in the Cation Ordering of Layered O3 $Li_xNi_{0.5}Mn_{0.5}O_2$
During Electrochemical Cycling to High Voltages

by

Hayley Han Li

Submitted to the Department of Mechanical Engineering
On January 19, 2007 in Partial Fulfillment of the
Requirements for the Degree of Master of Science in
Mechanical Engineering

ABSTRACT

Selected area electron diffraction patterns were collected from a pristine $LiNi_{0.5}Mn_{0.5}O_2$ sample and cycled $Li_xNi_{0.5}Mn_{0.5}O_2$ samples to 4.5 V and 5.3 V in the charged and discharged states. In the pristine sample, the single-crystal diffraction patterns clearly revealed superlattice reflections consistent with a $\sqrt{3}\boldsymbol{a}_{Hex.} \times \sqrt{3}\boldsymbol{a}_{Hex.} \times \boldsymbol{c}_{Hex.}$ supercell that is characteristic of cation ordering in the transition metal layer. Furthermore, these superlattice reflections were found to have considerably weakened or completely disappeared in the charged samples. Comparing the 4.5 V and 5.3 V charged samples, fewer crystals in the 5.3 V charged sample were found to exhibit these superlattice reflections. Another difference is that additional superlattice reflections consistent with the O1 phase with hexagonal-close-packed oxygen array were detected in the 5.3 V but not in the 4.5 V charged sample. Therefore, electron diffraction evidence was found to support the concept of Ni migration from the Li to the transition metal layer, and to confirm the increased Ni occupancy in the transition metal layer upon charging. In addition, electron diffraction data showed that Ni migration was in part reversible upon discharge as demonstrated by the increase in the fractions of crystals exhibiting the $\sqrt{3}\boldsymbol{a}_{Hex.} \times \sqrt{3}\boldsymbol{a}_{Hex.} \times \boldsymbol{c}_{Hex.}$ superlattice reflections from the charged to the discharged samples. The excellent electrochemical activity and reversibility of $LiNi_{0.5}Mn_{0.5}O_2$ having Ni in the Li layer may be attributed to the mobility of Ni ions upon electrochemical cycling. It has been found that high voltage exposure has resulted in higher discharge capacity and better rate capability.

In the cycled samples, a new type of superlattice reflections was observed in addition to the $\sqrt{3}\boldsymbol{a}_{Hex.} \times \sqrt{3}\boldsymbol{a}_{Hex.} \times \boldsymbol{c}_{Hex.}$ superlattice reflections. These superlattice reflections are similar for both the charged and the discharged samples, but their origins were believed to differ. For the charged samples, it was proposed that Li, Ni, and vacancies are partially ordered in the tetrahedral sites in a $2\boldsymbol{a}_{Hex.} \times 2\boldsymbol{a}_{Hex.} \times \boldsymbol{c}_{Hex.}$ supercell with the space group $R\bar{3}m$. Such ordering may improve the stability of the O3 layered structure upon charging to high voltages. For the discharged samples, Li, Ni, and vacancies order mostly in the octahedral sites in an $\boldsymbol{a}_{Mon.} \times \boldsymbol{a}_{Mon.} \times \boldsymbol{c}_{Mon.}$ cell with the space group P2/m. It was believed that this arrangement may facilitate Li diffusion in the interlayer slab space upon discharge.

Thesis Supervisor: Yang Shao-Horn
Title: Assistant Professor of Mechanical Engineering

LIST OF PUBLICATIONS

Hayley H. Li, Naoaki Yabuuchi, Ying S. Meng, Sundeep Kumar, Julien Breger, Clare P. Grey, and Yang Shao-Horn, *Changes in the Cation Ordering of Layered O3 $Li_xNi_{0.5}Mn_{0.5}O_2$ During Electrochemical Cycling to High Voltages: An Electron Diffraction Study.* Submitted to Chemistry of Materials, 2007.

Naoaki Yabuuchi, Sundeep Kumar, Hayley H. Li, Yong-Tae Kim, and Yang Shao-Horn, *Changes in the Crystal Structure and Electrochemical Properties of $Li_xNi_{0.5}Mn_{0.5}O_2$ during Electrochemical Cycling to High Voltages.* Submitted to Journal of the Electrochemical Society, 2006.

ACKNOWLEDGMENTS

I would like to give my deepest gratitude to my family: my grandma, mom, and dad. You have given me so much that words cannot express – thank you for your constant love and inspiration. I also want to thank Leo Chan, my pillar and partner in life, for your love, understanding, and for just being you.

I am very thankful for Dr. Yang Shao-Horn, my research advisor. Thank you for your guidance, patience, and for challenging me to always aim higher. In addition, I would like to thank Dr. Sundeep Kumar, Dr. Naoaki Yabuuchi, Anjuli Appapillai, and the coauthors of my two publications. I have learned so much from every one of you.

As I close the last chapter of my student life, I am excited to start my career, but at the same time sad to leave the memories behind. Looking back, I have been very fortunate to have mentors who guided, challenged, and inspired me. I would like to thank Dr. John Henshaw and Dr. Gordon Purser of the University of Tulsa for helping me with science fair projects in high school. I also want to thank Dr. Van Carey, Dr. Kyriakos Komvopoulos, and Dr. Hari Dharan of the University of California – Berkeley. You have been both excellent lecturers and caring advisors for me.

This work was supported by the MIT Presidential Fellowship and the MRSEC Program of the National Science Foundation under award number DMR 02-13282.

ABOUT THE AUTHOR

I was born in Beijing, China, on March 7, 1983, and attended the No. 3 Elementary School in the Chaoyang District. After the 6th grade, I moved to Edmond, Oklahoma where my parents attended graduate school. In Oklahoma, I learned English and studied at the Sequoyah Middle School. Two years later, my family moved again to Bartlesville, Oklahoma, where I went to the Bartlesville High School. My most memorable moments in high school were being very involved in sports (cross-country, tennis, soccer, and karate), and attending summer camps at various local universities.

In 2001, I graduated from high school, and moved to Berkeley, California, to study Mechanical Engineering at the University of California – Berkeley. I loved the culture, academic rigor, and beautiful campus of Berkeley where many happy memories were made. During the summers, I interned at Lockheed Martin in Sunnyvale, California, Motorola in Plantation, Florida, and ExxonMobil in Torrance, California. Though I enjoyed these internships, I realized that I do not find my passion in the traditional mechanical engineering field.

Upon graduation in 2005, I decided to further my study in Mechanical Engineering at the Massachusetts Institute of Technology in Cambridge, Massachusetts. Over the past one and a half years, I have spent a lot of energy searching for my interests and an exciting career path to follow. I am very happy to have moved to the east coast, and have made many good friends here in Boston.

Looking ahead, I am excited to start working as an investment banking analyst in the media and communications group of Morgan Stanley in New York City, New York. I also look forward to starting a new chapter in my life as a young working professional. It is really true that time flies faster as I get older. In the future, I am certain that I will look back to my school days and remember the good old times...

TABLE OF CONTENTS

LIST OF FIGURES

LIST OF TABLES

1.0 INTRODUCTION

1.1 $LiNi_{0.5}Mn_{0.5}O_2$ as a Positive Electrode Material

The rechargeable battery technology has traditionally been used to power portable electronics such as cell phones and laptops that require only moderate amounts of energy and power. For the high-energy and high-power applications, such as a car, fossil fuel based technologies have been predominantly utilized. As the society is becoming more aware of the negative environmental impacts of these technologies, research has been focused on improving the batteries technology as an alternative source of energy.

In particular, $LiNi_{0.5}Mn_{0.5}O_2$ has been studied as attractive positive electrodes for high-energy, high-power advanced Li-ion batteries[3-13]. Compared to the standard cathodes used in commercial applications, namely $LiCoO_2$, $LiNi_{0.5}Mn_{0.5}O_2$ has a higher discharge capacity and better rate capability[14]. More specifically, its discharge capacity has been reported to be ~190 mAh/g upon cycling between 4.5 V and 2.0 V at 11.0 mA/g[4, 15, 16]. $LiNi_{0.5}Mn_{0.5}O_2$ has a similarly O3 layered structure as $LiCoO_2$ (Figure 1). The main difference is that ~0.08 to 0.12 Ni per formula unit is present in the Li layer, and displaces the same amount of Li ions into the transition metal layer[15, 17-19]. The mixing of Li and Ni ions may be a result of their similar ionic radii[20] of 0.76 Å and 0.69 Å, respectively. It has been shown that reducing the size differences between the cations increases the extent of interlayer mixing[21]. Usually, having Ni ions in the Li layer impedes Li diffusion and results in a significantly larger polarization and irreversible capacities[22]. However, in $LiNi_{0.5}Mn_{0.5}O_2$, excellent reversible capacity and cycleability have been observed[3-5, 17]. This may be related to the different ways its structure changes upon Li removal and electrochemical cycling. In order to understand the electrochemical

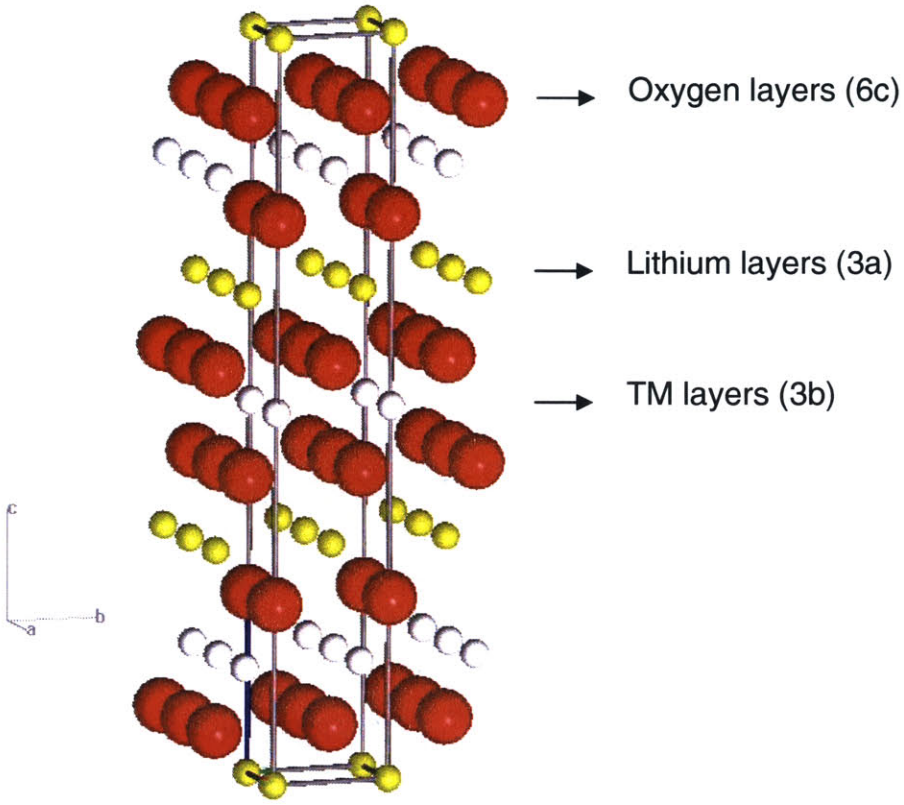

Figure 1[1]: Ideal structural model of $LiNi_{0.5}Mn_{0.5}O_2$ based on $LiCoO_2$ (α-$NaFeO_2$ structure, space group $R\bar{3}m$, $a_{Hex.} = b_{Hex.} = 2.8874$ Å, $c_{Hex.} = 14.2825$ Å and $\gamma = 120°$). Each atom in every layer is surrounded by 6 atoms in the same layer. Li atoms are on the 3a sites, Ni and Mn atoms share the 3b sites, and oxygen atoms are on the 6c sites.

behavior of $LiNi_{0.5}Mn_{0.5}O_2$, several research groups have studied the local environment of Li and the long range cation arrangements in the material.

1.2 Local Environment of Li and Long Range Cation Distribution in $Li_xNi_{0.5}Mn_{0.5}O_2$

1.2.1 Pristine $LiNi_{0.5}Mn_{0.5}O_2$

In the pristine sample, the Li ions in the transition metal layer are electrochemically active, and are preferentially surrounded by six Mn ions or five Mn and one Ni ions[8]. The local interactions amongst the Li, Ni, and Mn ions determine the long range cation arrangement of the material. Previous electron diffraction studies have revealed long range ordering in the pristine sample that is consistent with a $\sqrt{3}\boldsymbol{a}_{Hex.} \times \sqrt{3}\boldsymbol{a}_{Hex.} \times \boldsymbol{c}_{Hex.}$ supercell with the space group $P3_112$[23, 24]. This type of ordering is based on two different octahedral sites in the transition metal layer, similar to those found in Li_2MnO_3[25], $Li_{0.33}CoO_2$[26, 27], and $Li_{0.33}NiO_2$[28]. One type of the octahedral sites is Li-rich, and the other one Li-deficient (Figure 2a). Previous first-principles studies[6] have employed a $2\sqrt{3}\boldsymbol{a}_{Hex.} \times 2\sqrt{3}\boldsymbol{a}_{Hex.} \times \boldsymbol{c}_{Hex.}$ supercell that commensurates with the $\sqrt{3}\boldsymbol{a}_{Hex.} \times \sqrt{3}\boldsymbol{a}_{Hex.} \times \boldsymbol{c}_{Hex}$ cell found experimentally[15, 23, 24] to examine the mechanism of Li de-intercalation from $Li_xNi_{0.5}Mn_{0.5}O_2$. In the proposed structure, each Li ion is surrounded by six Mn ions that are further enveloped by 12 Ni ions. This type of ordering forms a flower-like cation arrangement in the transition metal layer (Figure 3). However, experimental evidence for this structure has not been reported.

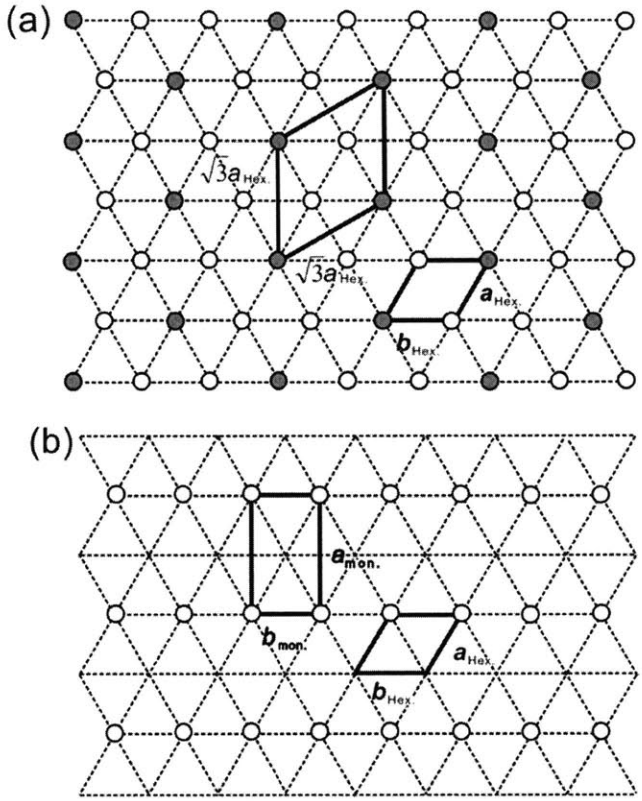

Figure 2: (a) In-plane ordering of two different sites on a triagonal lattice to form a $\sqrt{3}\boldsymbol{a}_{\mathrm{Hex.}} \times \sqrt{3}\boldsymbol{a}_{\mathrm{Hex.}} \times \boldsymbol{c}_{\mathrm{Hex.}}$ super cell. (b) Schematic of the octahedral site ordering under the P2/m symmetry.

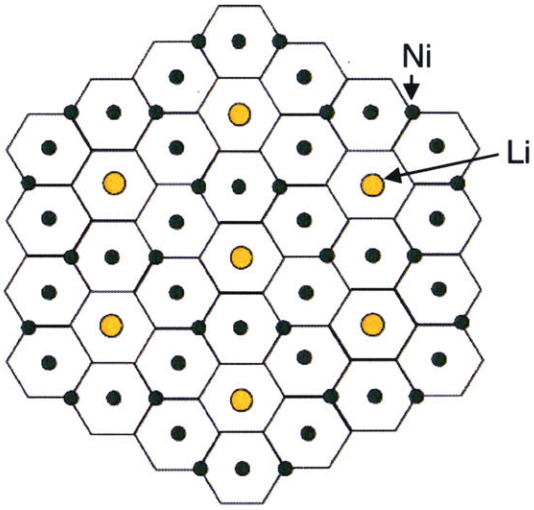

Figure 3[1]: The flower ordering as predicted by first-principles calculations. The Li, Ni, and Mn atoms are in yellow, green, and at the empty corners of the hexagons, respectively.

1.2.2 Cycled $Li_xNi_{0.5}Mn_{0.5}O_2$

Diffraction and Li magic angle spinning (MAS) nuclear magnetic resonance (NMR) data[1, 8, 29] suggest that the arrangement of cations changes upon electrochemical cycling. At the beginning of charge, Li ions from the transition metal and the Li layer are simultaneously removed (Figure 4), a process that is associated with the ~3.9 V plateau on the galvanostatic charge profile[6, 8, 29]. Then, the remaining Li ions can migrate and fill the tetrahedral sites adjacent to the vacant Li octahedral sites in the transition metal layer[29] (Figure 4). Li migration is first inferred from the Rietveld refinement of synchrotron powder X-ray diffraction data[19, 30] of charged $Li_xNi_{0.5}Mn_{0.5}O_2$ samples, and also confirmed by neutron diffraction measurements[1]. In addition to the Li ions, synchrotron X-ray data have detected some Ni ions (~0.01 per formula unit) in the tetrahedral sites of the Li layer[19, 30]. The tetrahedral sites of the Li layer are available for occupancy only if they share faces with vacant octahedral sites in the transition metal layer. This is because the face-sharing tetrahedral and octahedral sites cannot be simultaneously occupied as the interatomic distances between the cations are too small. As shown in Figure 4, Li and Ni ions in the Li layer that share faces with these available tetrahedral sites can migrate into them, and further into the octahedral sites of the transition metal layer[1, 29]. Such migration is highly unfavorable in Li_xCoO_2 and $Li_{1-z-x}Ni_{1+z}O_2$ because there are no vacancies in the transition metal layer. Furthermore, neutron powder diffraction data have correlated the migration of Ni ions from the Li to the transition metal layer with charging to high voltages[1].

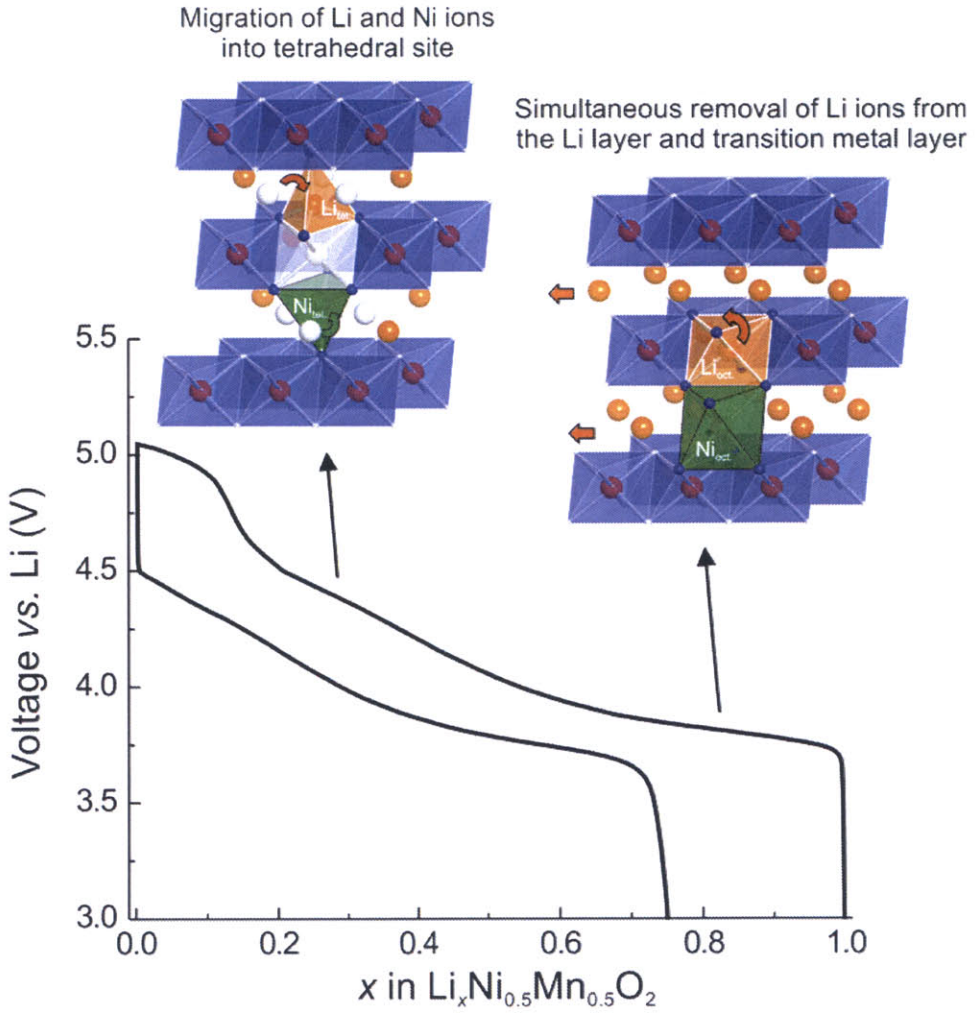

Figure 4: A representative galvanostatic charge and discharge voltage profile of $Li_xNi_{0.5}Mn_{0.5}O_2$ and schematics of the structures at selected Li contents. At the beginning of charge, Li ions are simultaneously removed from the Li and transition metal layers. Upon further de-intercalation of Li ions, Li and Ni ions migrate into the tetrahedral sites.

1.3 Effect of High Voltage Cycling[2]

1.3.1 Effect on Electrochemical Properties

1.3.1.1 Reversible Capacity and Rate Capability

Figure 5a compares the voltage profiles of two $Li/LiNi_{0.5}Mn_{0.5}O_2$ cells in the first cycle. The cells have been cycled between 4.5 V and 2.0 V and between ~5.0 V and 2.0 V, respectively. Typically, ~0.78 Li per formula unit can be removed by charging to 4.5 V in the first cycle. Charging to voltages greater than 5.0 V removes additional Li ions from $Li_xNi_{0.5}Mn_{0.5}O_2$. However, the exact amount of Li removal at voltages greater than 4.5 V cannot be accurately estimated from the voltage profiles, due to the electrolyte decomposition process that occurs simultaneously at voltages greater than ~4.6 V. More specifically, the ~5 V plateau in the charge profile can be attributed to the intercalation of PF_6^- into the Super P carbon particles in the cathode, as PF_6^- ions can be incorporated into the graphene sheets at ~5 V[31]. OCV data suggest that Li intercalation into $Li_xNi_{0.5}Mn_{0.5}O_2$ begins at ~4.55 V regardless of the charging voltage limits (Figure 5b). Although no reversible Li intercalation and de-intercalation process has been found at voltages greater than 4.55 V, increasing the upper charging voltage limits has consistently resulted in higher discharge capacities in the voltage range between 4.5 V and 2.0 V. For example, the cell that has been charged to ~5.0 V shows a higher discharge capacity (~218 mAh/g) than the cell that has been charged to 4.5 V (~185 mAh/g), as shown in Figure 6a. Moreover, charging to ~5 V leads to the appearance of a new process at ~4.3 V upon the first discharge, as shown in the inset of Figure 5a. Therefore, these results suggest that Li de-intercalation and cycling to high voltages may result in some permanent structural changes in $Li_xNi_{0.5}Mn_{0.5}O_2$.

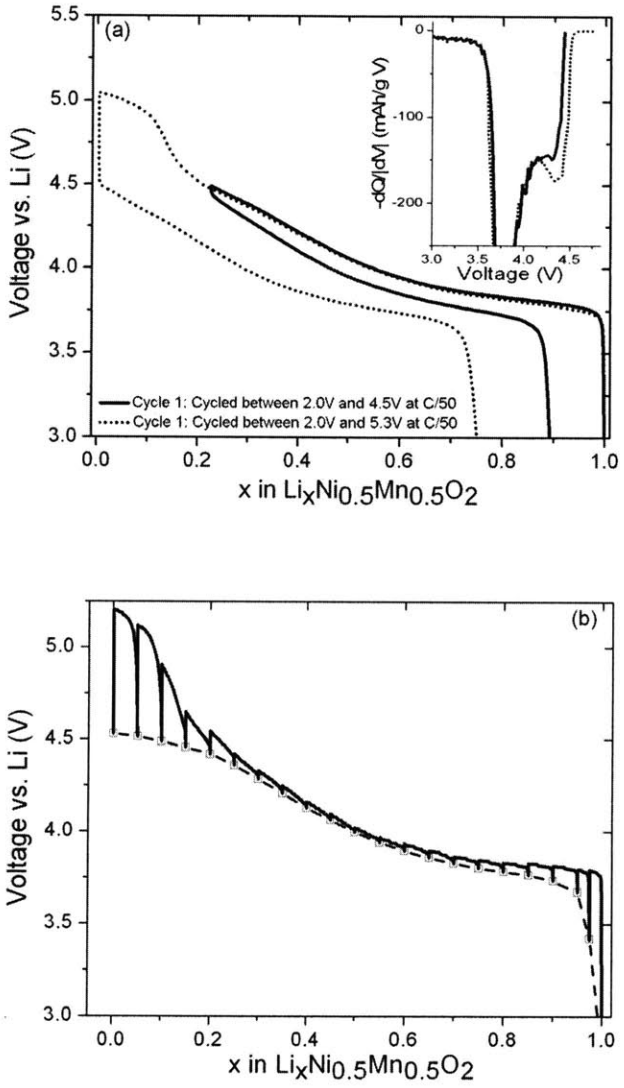

Figure 5[2]: (a) The voltage profiles of two $Li/Li_xNi_{0.5}Mn_{0.5}O_2$ cells in the first cycle. The inset shows the differential capacity plots of these two cells on discharge. (b) Voltage profile on the first charge of a $Li/Li_xNi_{0.5}Mn_{0.5}O_2$ cell with intermittent OCV steps of 5 hrs. The cell was cycled between 5.3 V and 2.0 V at 14 mA/g.

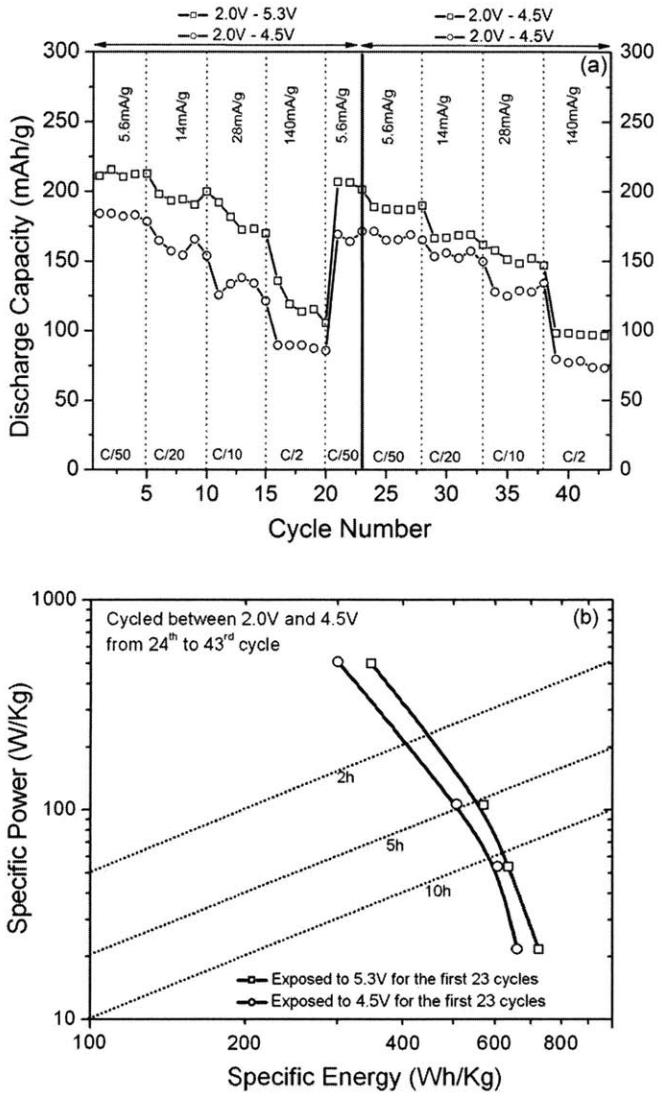

Figure 6[2]: (a) Discharge capacities of two representative $Li/Li_xNi_{0.5}Mn_{0.5}O_2$ cells that were cycled from 5.3 V to 2.0 V and from 4.5 V to 2.0 V for 23 cycles, and subsequently cycled from 4.5 V to 2.0 V at different rates. (b) Gravimetric power and energy density comparison of two $Li/LiNi_{0.5}Mn_{0.5}O_2$ cells upon discharge, which were cycled between 4.5 V and 2.0 V from the 24th to the 43rd cycle. For the first 23 cycles, one cell (squares) was cycled between 5.3 V and 2.0 V, and the other (circles) was cycled between 4.5 V and 2.0 V.

Current density also has an effect on the discharge capacity of the electrodes regardless of the upper voltage limit. The discharge capacities of the two cells shown in Figure 6a are for cycling to 4.5 V and 5.3 V, respectively, under the following rates: C/50, C/20, C/10, and C/2. As expected, the discharge capacities decrease considerably with increasing current densities. The reversible capacities of these cells are maintained with minimal capacity fade upon cycling. The cells that have been cycled to 5.3 V have higher discharge capacities in comparison to those that have been cycled to 4.5 V at all current densities. Moreover, the cells that are exposed to 5.3 V in the first 23 cycles show higher discharge capacities upon subsequent cycling from the 24^{th} to the 43^{rd} cycle, when the upper voltage limit is lowered to 4.5 V, than the cells that have been cycled to 4.5 V for an identical number of cycles without exposure to voltages higher than 4.5 V, as shown in Figure 6a. Therefore, exposure to ~5 V and higher has led to increased specific power and energy densities upon subsequent cycling in the voltage range between 4.5 V and 2.0 V, which is clearly revealed in the Ragone plot in Figure 6b.

1.3.1.2 The Reversible Process at 4.3 V

Upon cycling to 5.3 V, a reversible process at ~4.3 V is observed. Charging to voltages equal or greater than 4.8 V has led to the appearance of a reversible voltage plateau at ~4.3 V, as shown in the differential capacity plots of Figures 5a inset and 7a. In contrast, the redox process at ~4.3 V is less pronounced in the electrodes cycled between 4.5 V and 2.0 V (Figures 5a inset and 7b). To verify that high voltage exposure has resulted in the development of the ~4.3 V process, the charge and discharge voltage profiles of two cells in the second cycle between 4.5 V and 2.0 V are compared in Figure

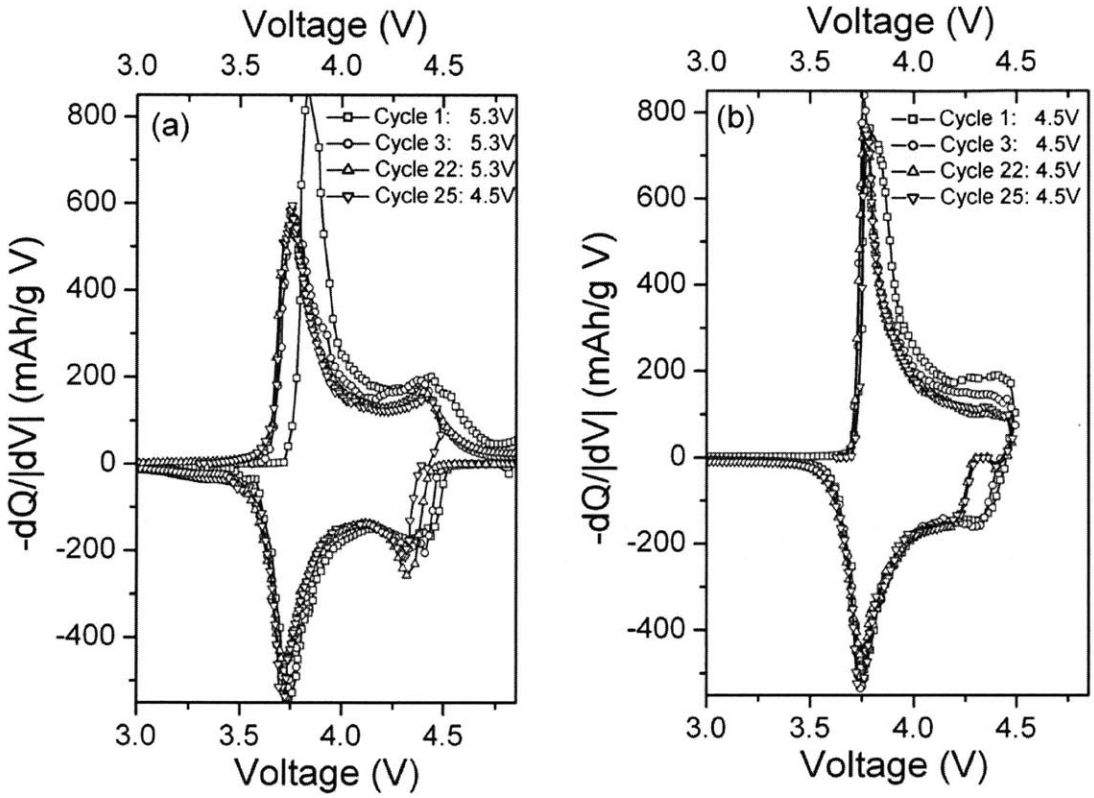

Figure 7[2]: (a) Differential capacity plots of a Li/$Li_xNi_{0.5}Mn_{0.5}O_2$ cell cycled between 5.3 V and 2.0 V on the 1st, 3rd, and 22nd cycle, and cycled between 4.5 V and 2.0 V on the 25th cycle; and (b) differential capacity plots of a cell cycled between 4.5 V and 2.0 V on the 1st, 3rd, 22nd, and 25th cycles.

8a. One of the cells has been first charged to ~5.3 V, held at 5.3 V for 6 hrs, and discharged to 2.0 V in the first cycle. The other cell has been cycled between 4.5 V and 2.0 V in the first cycle. As shown in Figure 8a, the cell that was exposed to 5.3 V in the first cycle exhibited a flatter slope at ~4.3 V in the charge and discharge voltage profiles during the second cycle in comparison to the cell without the 5.3 V exposure. Although the ~4.3 V peak appears to grow upon cycling to 5.3 V (without any holds), additional high voltage holds at 5.3 V in the subsequent cycles do not lead to more increase in the 4.3 V peak intensity in the differential plots, as shown in Figure 8b. This suggests that the development of the 4.3 V plateau on discharge can be enhanced by exposure to 5.3 V.

1.3.2 Synchrotron X-Ray Diffraction Studies of Changes in Structure From High Voltage Cycling

Lattice parameters of the O3 layered $Li_xNi_{0.5}Mn_{0.5}O_2$ structure changes considerably with Ni oxidation upon Li de-intercalation. Synchrotron X-ray diffraction data have shown that the $c_{Hex.}$ parameter of the rhombohedral O3 structure in the 4.5 V charged $Li_{0.2}Ni_{0.5}Mn_{0.5}O_2$ sample (14.373 Å) is greater than that of the monoclinic O3 phase in the 5.3 V charged sample (14.14 Å), in good agreement with previous diffraction studies[15, 30]. In addition, the bond length between the transition metal and the oxygen ions (Me-O) is calculated to be 1.979 Å in the pristine sample. As expected, the Me-O bond length decreases with the oxidation of Ni^{2+} upon charge to 4.5 V, and increases upon discharge to 2.0 V (Table 1). Moreover, the Me-O bond length decreases again upon further charging from 4.5 V to 5.3 V. The Me-O bond length of the 5.3 V charged sample (1.916 Å) is similar to that observed for a ~4.9 V charged $Li_xNi_{0.5}Mn_{0.5}O_2$ (x = ~0) sample by EXAFS measurements (1.912 Å)[32], and that

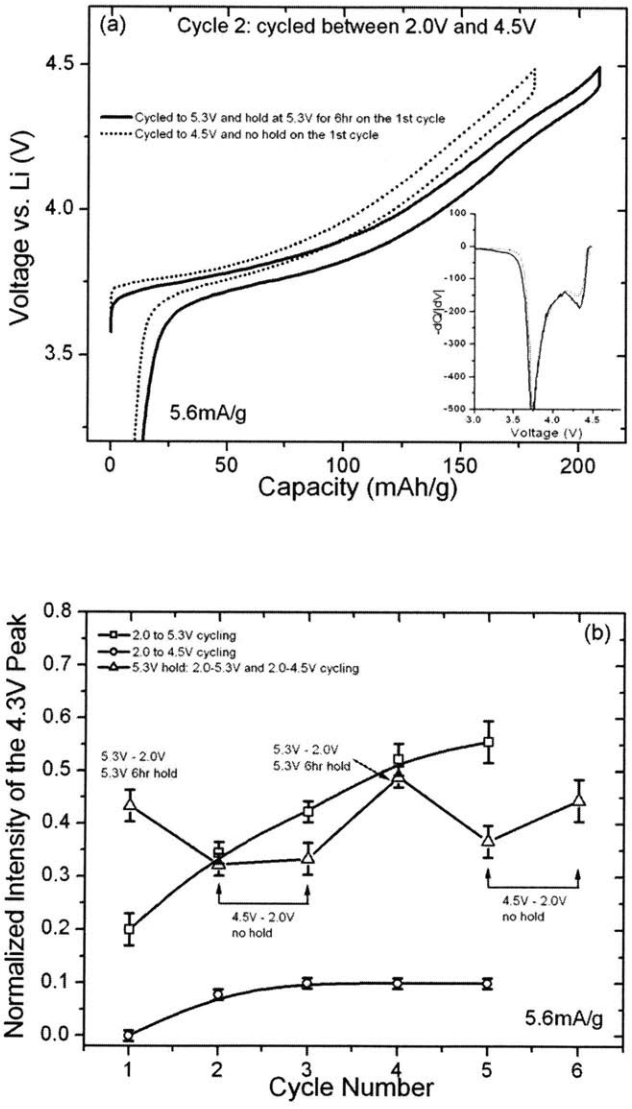

Figure 8[2]: (a) Galvanostatic voltage profiles of two $Li/Li_xNi_{0.5}Mn_{0.5}O_2$ cells in the second cycle between 4.5 V and 2.0 V at 5.6 mA/g. One of the cells was cycled between 5.3 V and 2.0 V, and held at 5.3 V for 6 hrs during charge on the first cycle. (b) The evolution of the 4.3 V peak upon discharge in the differential capacity plots. The 4.3 V peak was normalized based on the height of dQ/|dV| upon discharge.

		pristine	4.5 V charged state	4.5 V discharged state	5.3 V charged state	5.3 V discharged state
Space Group		$R\bar{3}m$	$R\bar{3}m$	$R\bar{3}m$	$C2/m$	$R\bar{3}m$
Lattice Constants (Å)		$a_{hex.}$ = 2.8777(2) $c_{hex.}$ = 14.256(1)	$a_{hex.}$ = 2.8326(3) $c_{hex.}$ = 14.373(1)	$a_{hex.}$ = 2.8700(3) $c_{hex.}$ = 14.308(1)	$a_{mon.}$ = 4.914(1) $b_{mon.}$ = 2.834(1) $c_{mon.}$ = 4.984(1) β = 108.92(1)°	$a_{hex.}$ = 2.8834(2) $c_{hex.}$ = 14.281(1)
3a site (2a site for $C2/m$)	Ni (g)	0.393(2)	0.439(4)	0.419(3)	0.45(1)	0.438(2)
	Mn (g)	0.5*	0.5*	0.500*	0.5*	0.5*
	Li (g)	0.107(2)	0*	0.03* and ##	0*	0*
	B**	0.30*	0.30*	0.30*	0.30*	0.30*
3b site (2d site for $C2/m$)	Li (g)	0.893(2)	0.220*	0.820*	0*	0.75*
	Ni (g)	0.107(2)	0.031(4)	0.063(3)	0.05(1)	0.062(2)
	B**	1.00*	1.20*	1.00*	1.20*	1.00*
6c site (4i site for $C2/m$)	Tetrahedral Ni (g)	0*	0.015(2)	0.009(1)	0*	0*
	B**	0.60*	0.60*	0.60*	0.60*	0.60*
	Octahedral O (g)	2.0*	2.0*	2.0*	2.0*	2.0*
	B**	0.70*	0.70*	0.70*	0.70*	0.70*
Positional Parameter z for 6c Site	Ni (Tetrahedral)	0.130***	0.133***	0.130***	x = 0.14, z = 0.40 (4i site)***	0.130***
	O (Octahedral)	0.2579(6)	0.2630(5)	0.2593(6)	x = 0.255(6), z = 0.789(5)	0.2582(5)
Unit Cell Volume (Å^3)		102.2	99.87	102.06	65.6 (98.5 as R-3m lattice)	102.85
Me-O distance (Å)		1.979	1.923	1.972	1.916# (1.879 × 2, 1.934 × 4)	1.977
Li-O distance (Å)		2.110	2.143	2.117	2.143# (2.117 × 2, 2.156 × 4)	2.120
MeO_2 Slab Space (Å)###		2.151	2.022	2.119	1.990	2.146
LiO_2 Slab Space (Å)###		2.601	2.769	2.651	2.725	2.614
R_{wp} (%)		13.7	15.2	14.5	28.7	10.7
R_B (%)		5.45	6.24	4.05	14.2	4.49

* not refined ** isotropic displacement parameter *** fixed based on z for octahedral site

average value ## fixed with the assumprtion based on the observation of NMR study[24] Small amount of lithium ions was observed after discharge.

Slab space was caluclated by using the relations.

MeO_2 Slab Space (Å) $2c_{hex.}(-z + 1/3)$ or $2c_{mon.} \sin\beta(-z + 1$ LiO_2 Slab Space (Å) $2c_{hex.}(z - 1/6)$ or $2c_{mon.} \sin\beta(z - 1/2)$

Table 1[2]: The crystallographic parameters for the $Li_xNi_{0.5}Mn_{0.5}O_2$ samples obtained by the Rietveld refinement of synchrotron X-ray powder diffraction data.

estimated based on a one-to-one combination of Mn^{4+} and Ni^{4+} (low-spin) using Shannon's ionic radii (1.87 Å)[20]. This result suggests that the valence state of the Ni ions in the electrode charged to 5.3 V is close to 4+, which indicates that Ni ions are oxidized and additional Li ions are removed upon charging $Li_xNi_{0.5}Mn_{0.5}O_2$ electrodes to voltages greater than 4.5 V in addition to the electrolyte decomposition process.

In Figures 9a-d, the synchrotron X-ray diffraction patterns of the pristine, charged samples to 4.5 V and 5.3 V, and discharged sample from 5.3 V are shown, respectively. The O3 phase is observed for all four samples. However, for the 5.3 V charged sample, an additional O1 phase is observed (Figure 9c). This suggests that the O1 phase can be formed at very low Li contents by cycling to high voltages. In addition, the appearance of the O1 phase implies that the Li layer has been depleted of both the Li and the Ni ions. As only the O3 phase is observed for the 5.3 V discharged sample, the O1 phase appears to be reversible upon discharge.

As evidenced by the formation of the O1 phase, the cation arrangements in the pristine material may change drastically upon Li de-intercalation. As the tetrahedral sites of the Li layer become available with the removal of the Li ions in the transition metal layer, new types of long range ordering may appear. There are two tetrahedral sites per octahedral site in the Li layer that share faces with the adjacent octahedral sites in the transition metal layer. As Li and Ni ions can reside in both the octahedral and the tetrahedral sites of the Li layer, ordering in these octahedral and tetrahedral sites might be possible due to the electrostatic forces amongst the cations. The distance between the cations in the nearest upper and lower tetrahedral sites is small, approximately 2.0 Å – 2.1 Å in the charged samples[19, 30], as shown in Figure 10, which might make the random

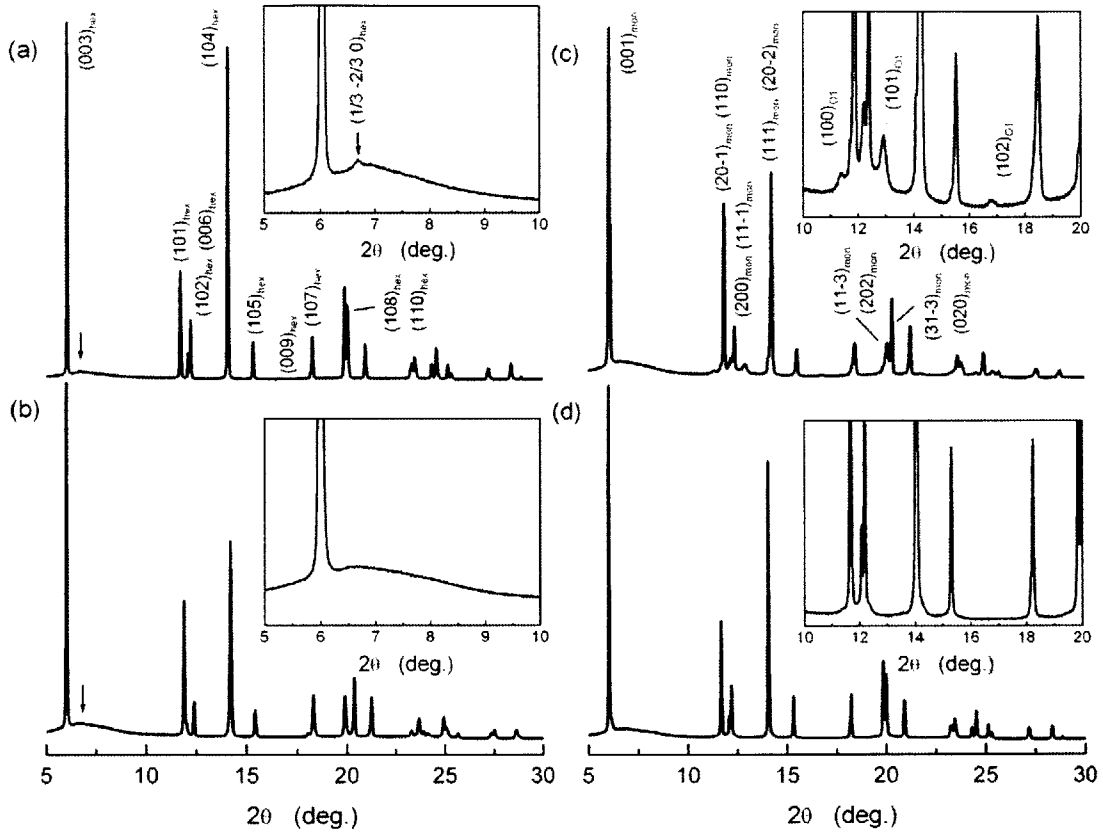

Figure 9[2]: Synchrotron X-ray diffraction patterns of $Li_xNi_{0.5}Mn_{0.5}O_2$: (a) pristine (x = 1; $R\bar{3}m$, $a_{Hex.}$ = 2.877 Å, $c_{Hex.}$ = 14.256 Å); (b) $Li_{0.2}Ni_{0.5}Mn_{0.5}O_2$ charged to 4.5 V after two cycles, which has a single O3 phase ($R\bar{3}m$, $a_{Hex.}$ = 2.833 Å, $c_{Hex.}$ = 14.373 Å); (c) $Li_0Ni_{0.5}Mn_{0.5}O_2$ charged to 5.3 V after 2 cycles, which has two phases: monoclinic O3 (C2/m, $a_{Mon.}$ = 4.914 Å, $b_{Mon.}$ = 2.834 Å, $c_{Mon.}$ = 4.984 Å, β = 108.92°), and O1 phase ($R\bar{3}m$, a_{O1} = 2.91 Å, c_{O1} = 4.68 Å); and (d) $Li_{0.75}Ni_{0.5}Mn_{0.5}O_2$ discharged to 2.0 V after cycling to 5.3 V for 5 cycles, which has a single O3 phase ($R\bar{3}m$, $a_{Hex.}$ = 2.883 Å, $c_{Hex.}$ = 14.281 Å). The wavelength used was 0.501 Å, as calibrated by CeO_2. X-ray diffraction pattern of the pristine sample (a) was obtained from a powder sample without additives while those of cycled samples (b-d) were obtained from composite electrodes consisting the active material, Super P carbon, and PVdF.

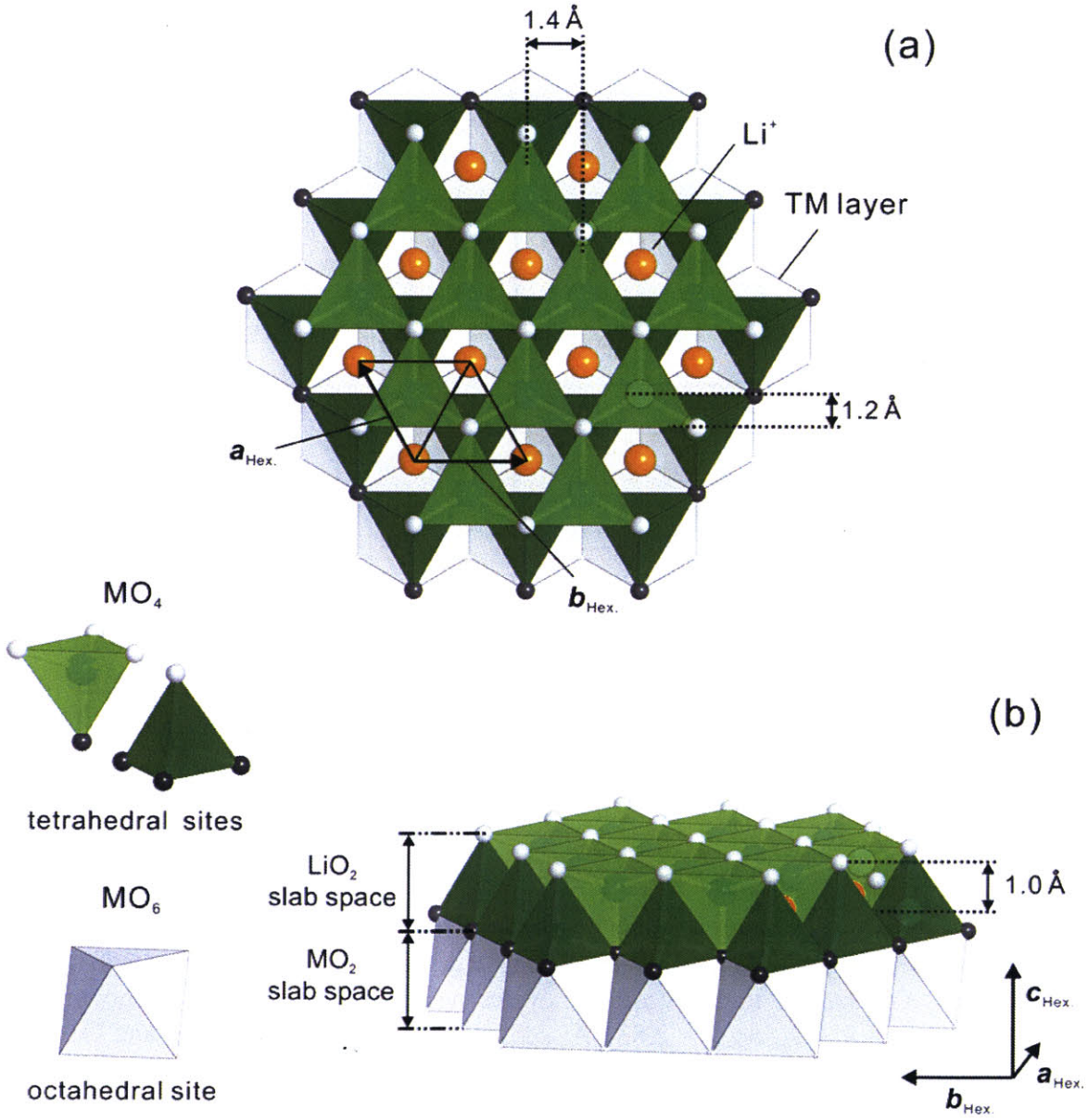

Figure 10: (a) Schematics of the crystal structure of $Li_xNi_{0.5}Mn_{0.5}O_2$ viewed perpendicular to the transition metal slabs, where the parent hexagonal cell is outlined. Upper and lower tetrahedra in the Li layer, octahedral Li ions, and octahedra in the transition metal layer are shown; (b) schematics of $Li_xNi_{0.5}Mn_{0.5}O_2$'s crystal structure viewed along the $\boldsymbol{a}_{Hex.}$ direction, where the upper and lower tetrahedral are revealed clearly.

occupancy of the nearest upper and lower tetrahedral sites unfavorable due to the strong repulsive interactions between the cations. Similarly for the octahedral sites of the discharged samples, ordering is possible due to the electrostatic interactions between the cations in the octahedral sites of the Li layer.

In the following chapters, the electron diffraction data of $Li_xNi_{0.5}Mn_{0.5}O_2$ samples cycled to 4.5 V and 5.3 V will be discussed for both the charged and discharge states, from which changes in the cation arrangement and the nature of cation ordering are proposed and analyzed in detail. Changes in the cation arrangement and ordering can play a significant role in the electrochemical properties and stability of cycled $Li_xNi_{0.5}Mn_{0.5}O_2$. Electron diffraction is more sensitive to cation ordering in comparison to X-ray and neutron powder diffraction. For example, single crystal electron diffraction analyses have clearly revealed superlattice reflections associated with the Li and vacancies ordering in the O3 layered $Li_{0.5}CoO_2$[27] and Li_xNiO_2[28, 33] and cation ordering in $LiNi_{0.5}Mn_{0.5}O_2$[23, 24], while these superlattice reflections are either not visible or extremely weak in the powder diffraction data. The focus of this study is to investigate how cation arrangements and ordering change in $Li_xNi_{0.5}Mn_{0.5}O_2$ samples in the charged and discharged states using selected area electron diffraction. Furthermore, the details of cation ordering are explored to explain the relationship between the structural changes in $Li_xNi_{0.5}Mn_{0.5}O_2$ upon Li removal with the material's electrochemical properties.

2.0 EXPERIMENTAL

2.1 Material Synthesis of Pristine $LiNi_{0.5}Mn_{0.5}O_2$

The pristine $LiNi_{0.5}Mn_{0.5}O_2$ sample was synthesized from the following steps: 1) Ni and Mn hydroxides were obtained from $Ni(NO_3)_2$ and $Mn(NO_3)_2$ with LiOH solution; 2) a stoichiometric amount of $LiOH{\cdot}H_2O$ was added to the Ni and Mn hydroxides, and the mixture was heated at 480 °C for 12 hrs in air; 3) a pellet was then made from the product; and 4) the pellet was heated at 1000 °C for 12 hrs in air, and was quenched to the room temperature between two thick copper plates.

2.2 Coin Cell Preparation

2016 Li coin cells were assembled with $LiNi_{0.5}Mn_{0.5}O_2$ composite electrodes, which consisted of 80 wt % of the pristine $LiNi_{0.5}Mn_{0.5}O_2$ powder with 10 wt % of Super P carbon (TIMCAL) and 10 wt % of poly-vinylidene fluoride (PVdF). The electrolyte used was a 1 M solution of $LiPF_6$ in a 1:1 EC:DMC solvent (Merck, TECHNO, SEMICHEM Co. Ltd., Korea). Coin cells were assembled inside an argon-filled glove box, and their schematics are shown in Figure 11. Two aluminum caps served as current collectors and were electrically insulated from each other by a gasket. Between the current collectors, there were a spacer to enhance the contact within the cell, a $LiNi_{0.5}Mn_{0.5}O_2$ cathode, 2 Celgard separators to allow ionic conduction, and a Li anode. Additionally, electrolyte was dropped with a pipette around the separator layers to fully saturate the entire cell. Finally, the assembly was securely packaged inside the coin cell with a crimper and allowed to age for 12 hrs before testing.

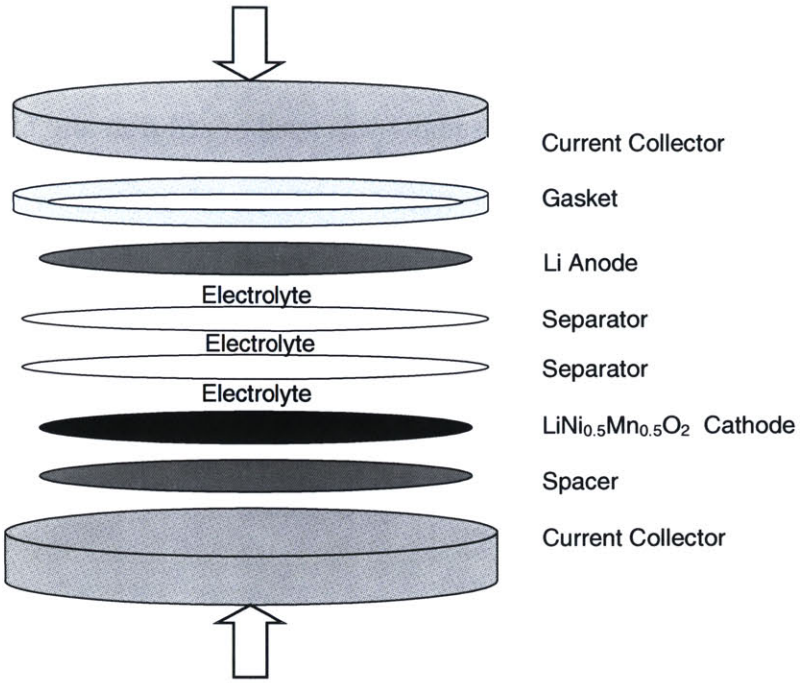

Figure 11: Schematic of a coin cell assembly.

The coin cells were cycled galvanostatically on a Solartron 1470 battery tester between 2.0 V and 4.5 V or 2.0 V and 5.3 V at a C/50 rate (current density = 5.6 mA/g and 0.027 mA/cm^2). Cycled positive electrodes were recovered from the coin cells inside the glove box, which were then rinsed thoroughly with diethyl carbonate to remove the electrolyte salt.

2.3 Preparation of Electrochemically Cycled Samples

In Table 2, the Li content and electrochemical cycling history of the samples used for electron diffraction are shown. The Li contents are calculated from the galvanostatic charge and discharge profiles assuming 100 % columbic efficiency. For the detailed charge and discharge profiles, please see Appendix B.

2.4 Transmission Electron Microscopy and Selected Area Electron Diffraction

Transmission electron microscopy (TEM) samples were prepared by suspending the powder from the positive electrodes onto a copper grid with lacy carbon. Single crystal selected area electron diffraction patterns were collected from the samples under an accelerating voltage of 200 keV on a JEOL 200CX or JEOL 2010 microscope. Selected area electron diffraction patterns were collected from 20 - 30 randomly selected single crystals within each sample (Figure 12). Simulation of single crystal electron and X-ray powder diffraction patterns was performed using the CaRIne Crystallography software (http://pros.orange.fr/carine.crystallography/). Some Rietveld refinement results[2] of synchrotron X-ray diffraction data (wavelength set to 0.5 Å) obtained at

Sample Name	Li Composition	Electrochemical History
Pristine	1.0	None
4.5 V Charged	0.2	Cycled between 4.5 V and 2.0 V for 2 complete cycles and 1 additional charged at C/50
5.3 V Charged	0.0	Cycled between 5.3 V and 2.0 V for 2 complete cycles and 1 additional charged at C/50
4.5 V Discharged	0.9	Cycled between 4.5 V and 2.0 V for 5 complete cycles at C/50
5.3 V Discharged	>0.76	Cycled between 5.3 V and 2.0 V for 5 complete cycles at C/50
4.5 V Discharged Extensively Cycled	0.8	Cycled between 4.5 V and 2.0 V for 5 cycles at C/50, 5 cycles at C/20, 5 cycles at C/5, 5 cycles at C/2, and 1 cycle at C/50

Table 2: Electron diffraction sample information. For their electrochemical cycling profiles, please see Appendix B.

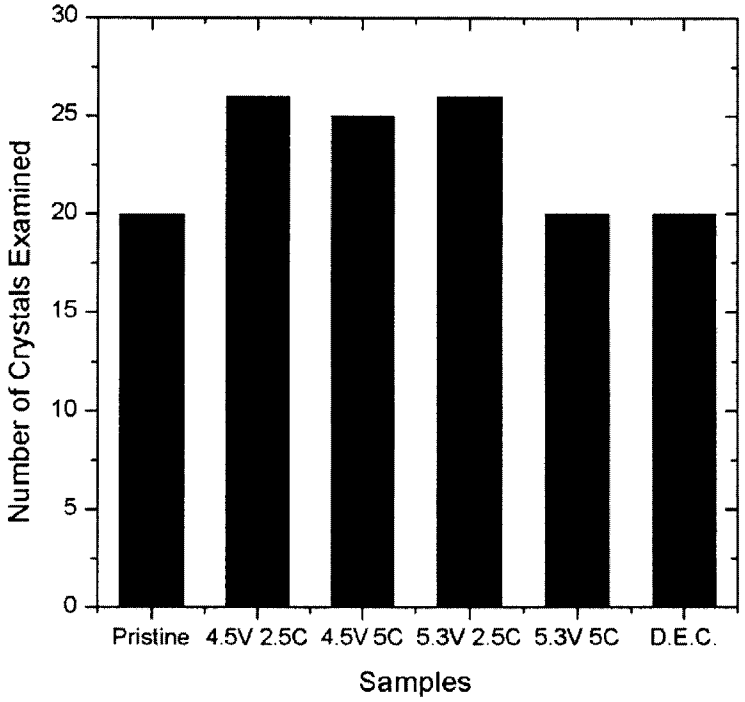

Figure 12: The number of crystals examined for the pristine, 4.5 V charged, 5.3 V charged, 4.5 V discharged, 5.3 V discharged, and extensively cycled 4.5 V discharged samples.

SPring-8 were compared and discussed with respect to the electron diffraction data.

It is important to note that the CaRIne software used to generate the electron diffraction simulations is not accurate in calculating the intensity of the electron diffraction spots. This is not an issue for this study as no conclusions were drawn based on the intensities of the simulated electron diffraction patterns. However, the intensity of the X-ray powder diffraction peaks can be accurately simulated. Furthermore, simulations of the electron diffraction patterns were double checked with the SingleCrystal software (http://www.crystalmaker.com/singlecrystal/index.html), which does calculate the intensities correctly, and no inconsistencies to the conclusions of this study were found.

Each electron diffraction pattern is identified by a particular zone axis, which contains a set of planes as represented by the diffraction reflections. To index the planes, the first step is to measure the distances of the parent reflections from the center beam, r, and the relative angles amongst the parent reflections. Knowing r, the plane spacing, d, can be calculated using the Bragg's Law,

$$rd = \lambda L \qquad (1)$$

where λ is the wavelength of the electron beam and L is the camera length. Then, the d values and the relative angles must be matched with the calculated d values and relative angles of the parent planes belonging to the specific zone axis of the electron diffraction pattern.

3.0 RESULTS

3.1 Pristine $LiNi_{0.5}Mn_{0.5}O_2$

TEM images of the $LiNi_{0.5}Mn_{0.5}O_2$ crystals are shown in Appendix C. In general, the particles are less than 1 micron in size, and have a plate or rectangular shape depending on orientation. Single crystal selected area electron diffraction patterns were collected from 20 randomly selected crystals of the pristine $LiNi_{0.5}Mn_{0.5}O_2$ sample, of which 95 % showed superlattice reflections that evidence long range ordering in the transition metal layer, consistent with previous studies[2, 23, 24]. Two representative patterns collected along the $[00\bar{1}]_{Hex.}$ and $[\bar{1}\bar{8}1]_{Hex.}$ zone axes are shown in Figures 13a-b, respectively. In addition to the fundamental reflections of the parent hexagonal cell with space group $R\bar{3}m$, superlattice reflections (marked by stars in Figures 13a-b) were observed. These superlattice reflections could be indexed consistently to the $\sqrt{3}\boldsymbol{a}_{Hex.} \times \sqrt{3}\boldsymbol{a}_{Hex.} \times \boldsymbol{c}_{Hex.}$ superstructure with the space group $P3_112$ as reported previously[23, 24], where the crystallographic relationship between the parent and the superstructure has been described in detail[24]. The $(11\boldsymbol{l})_{Hex.}$ planar spacings ($\boldsymbol{l} = 3n$, $n = 0, \pm1, \pm2\ldots$) in the parent hexagonal structure are tripled by the presence of superlattice reflections, which is in good agreement with the simulated patterns (Figures 14a-b). The appearance of these superlattice reflections is indicative of cation ordering in the transition metal layer into Li-rich and Li-deficient sites in the trigonal lattice[23, 24].

Electron diffraction patterns with superlattice reflections consistent with a $2\sqrt{3}\boldsymbol{a}_{Hex.} \times 2\sqrt{3}\boldsymbol{a}_{Hex.} \times \boldsymbol{c}_{Hex.}$ superstructure were also observed in the pristine sample (Figures 15a-b). In general, the experimental electron diffraction patterns do not match with the simulated patterns based on the flower type structure model, with the exception

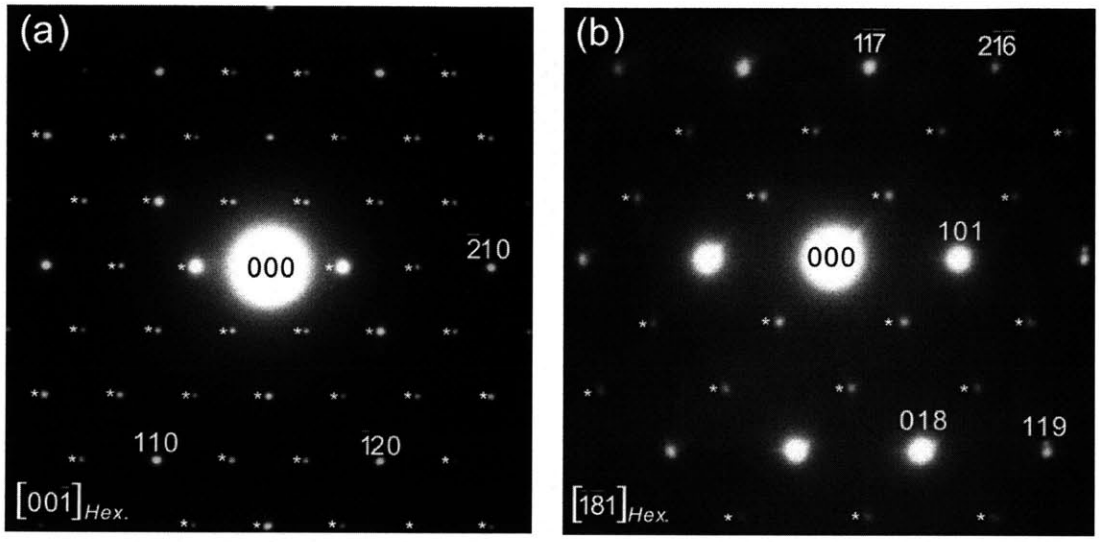

Figure 13: Experimental electron diffraction patterns collected from the pristine $LiNi_{0.5}Mn_{0.5}O_2$ sample along the (a) $[00\bar{1}]_{Hex.}$ zone axis, and (b) $[\bar{1}\bar{8}1]_{Hex.}$ zone axis. Superlattice reflections consistent with the $\sqrt{3}\boldsymbol{a}_{Hex.} \times \sqrt{3}\boldsymbol{a}_{Hex.} \times \boldsymbol{c}_{Hex.}$ supercell are marked by white stars.

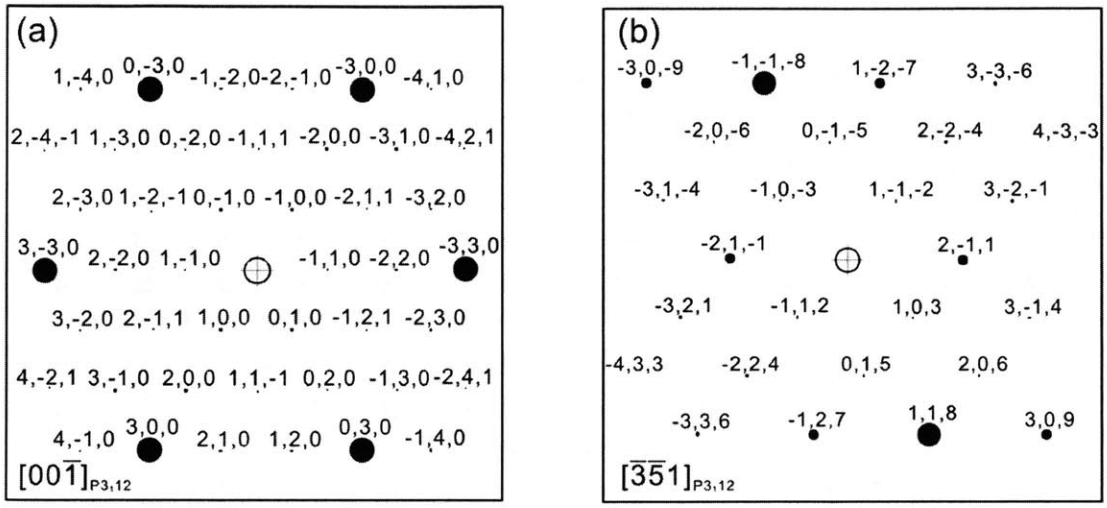

Figure 14: Simulated electron diffraction patterns of the experimental patterns in Figure 13 collected from the pristine $LiNi_{0.5}Mn_{0.5}O_2$ sample with (a) $[00\bar{1}]_{Hex.}$ zone axis, and (b) $[\bar{1}\bar{8}1]_{Hex.}$ zone axis.

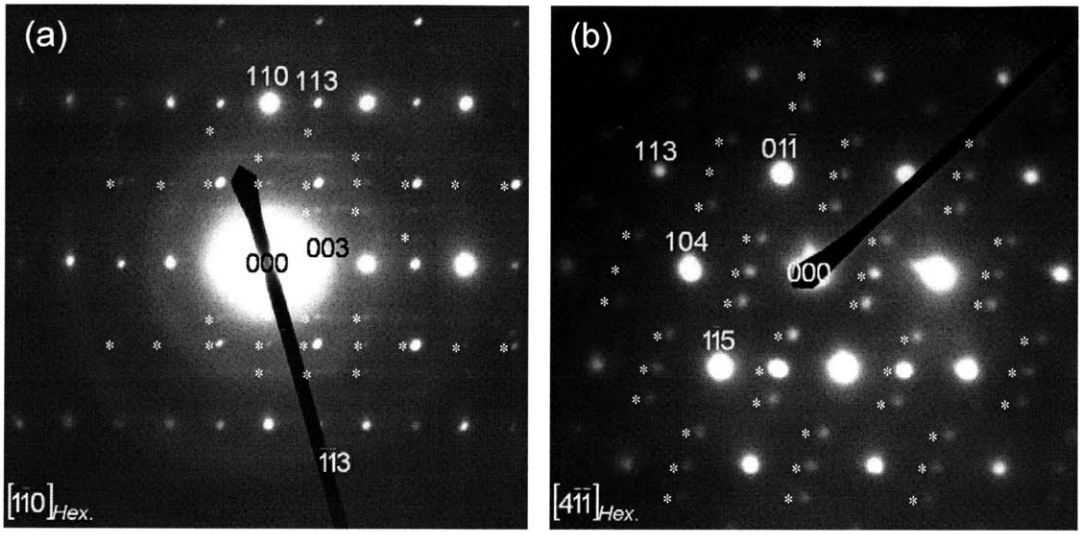

Figure 15: Experimental electron diffraction patterns collected from the pristine $LiNi_{0.5}Mn_{0.5}O_2$ sample along the (a) $[1\bar{1}0]_{Hex.}$ zone axis, and (b) $[4\bar{1}\bar{1}]_{Hex.}$ zone axis. Superlattice reflections consistent with the $2\sqrt{3}\boldsymbol{a}_{Hex.} \times 2\sqrt{3}\boldsymbol{a}_{Hex.} \times \boldsymbol{c}_{Hex.}$ supercell are marked by white stars.

of the $[1\bar{1}0]_{Hex.}$ zone axis (Figures 16a-b). The nature of cation ordering that results in the $2\sqrt{3}\boldsymbol{a}_{Hex.} \times 2\sqrt{3}\boldsymbol{a}_{Hex.} \times \boldsymbol{c}_{Hex.}$ type superlattice reflections is not clearly understood.

3.2 Electrochemically Charged $Li_xNi_{0.5}Mn_{0.5}O_2$ Samples

Electron diffraction patterns were collected from 26 randomly selected crystals in both of the charged samples to 4.5 V ($Li_{0.2}Ni_{0.5}Mn_{0.5}O_2$) and 5.3 V ($Li_0Ni_{0.5}Mn_{0.5}O_2$). The electron diffraction patterns of these charged samples differ from the pristine sample in the following three ways. First, a significant percentage of the crystals in the charged samples no longer exhibited superlattice reflections of the $\sqrt{3}\boldsymbol{a}_{Hex.} \times \sqrt{3}\boldsymbol{a}_{Hex.} \times \boldsymbol{c}_{Hex.}$ type. Second, a fraction of the crystals showed superlattice reflections that double some interplanar spacings in the parent structure that could not be indexed to the $\sqrt{3}\boldsymbol{a}_{Hex.} \times \sqrt{3}\boldsymbol{a}_{Hex.} \times \boldsymbol{c}_{Hex.}$ supercell. The appearance of these superlattice reflections was more predominant in the 4.5 V charged sample than the 5.3 V charged sample. Finally, superlattice reflections unique to the O1 phase, which were reported previously for highly de-intercalated Li_xCoO_2[34] and Li_xNiO_2[35, 36] (x = ~0) samples, were found in some patterns collected from the 5.3 V charged sample.

3.2.1 Disappearance of the $\sqrt{3}\boldsymbol{a}_{Hex.} \times \sqrt{3}\boldsymbol{a}_{Hex.} \times \boldsymbol{c}_{Hex.}$ Superlattice Reflections

Not only were the intensities of the $\sqrt{3}\boldsymbol{a}_{Hex.} \times \sqrt{3}\boldsymbol{a}_{Hex.} \times \boldsymbol{c}_{Hex.}$ superlattice reflections in the 4.5 V and 5.3 V charged samples weakened considerably in comparison to those observed for the pristine sample, a significant fraction of the crystals exhibited only the fundamental reflections of the parent structure. Representative electron diffraction patterns from the 4.5 V and 5.3 V charged samples along the $[\bar{4}\bar{8}1]_{Hex.}$ and

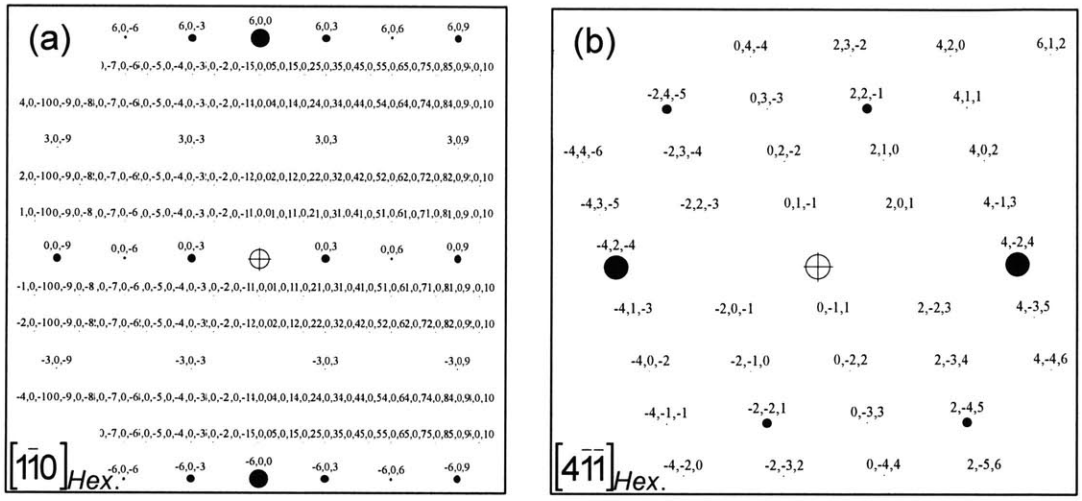

Figure 16: Simulated electron diffraction patterns of the experimental patterns in Figure 15 collected from the pristine $LiNi_{0.5}Mn_{0.5}O_2$ sample with (a) $[1\bar{1}0]_{Hex.}$ zone axis, and (b) $[4\bar{1}\bar{1}]_{Hex.}$ zone axis.

$[45\bar{1}]_{Hex.}$ zone axes are shown in Figures 17a-b, respectively. Superlattice reflections that were expected for the $\sqrt{3}\boldsymbol{a}_{Hex.} \times \sqrt{3}\boldsymbol{a}_{Hex.} \times \boldsymbol{c}_{Hex.}$ supercell in the marked reciprocal directions were not observed. In addition, the 5.3 V charged sample had much fewer crystals (~19 %) showing the $\sqrt{3}\boldsymbol{a}_{Hex.} \times \sqrt{3}\boldsymbol{a}_{Hex.} \times \boldsymbol{c}_{Hex.}$ superlattice reflections than the 4.5 V charged sample (~58 %). The weakening and disappearance of these superlattice reflections in the charged samples reflect a decreased contrast in the average electron scattering factor between the Li-rich and the Li-deficient sublattices of the $\sqrt{3}\boldsymbol{a}_{Hex.} \times \sqrt{3}\boldsymbol{a}_{Hex.} \times \boldsymbol{c}_{Hex.}$ superstructure[23]. This observation is indicative of changes in the cation distribution during Li de-intercalation.

3.2.2 Appearance of Doubling Superlattice Reflections

In addition to the disappearance of the $\sqrt{3}\boldsymbol{a}_{Hex.} \times \sqrt{3}\boldsymbol{a}_{Hex.} \times \boldsymbol{c}_{Hex.}$ superlattice reflections, extra reflections that led to the doubling of some interplanar spacings of the parent structure, such as the $(10\boldsymbol{l})_{Hex.}$ and $(11\boldsymbol{l})_{Hex.}$ planar spacings ($\boldsymbol{l}$ = 2n, n = 0, $\pm$1, $\pm$2...), were noted in the charged samples. The presence of these reflections can be attributed to the formation of a hexagonal $2\boldsymbol{a}_{Hex.} \times 2\boldsymbol{a}_{Hex.} \times \boldsymbol{c}_{Hex.}$ supercell or a monoclinic $\boldsymbol{a}_{Mon.} \times \boldsymbol{a}_{Mon.} \times \boldsymbol{c}_{Mon.}$ primitive cell similar to that reported previously for $Li_{0.5}CoO_2$[27]. The detailed crystallographic relationship between the parent and monoclinic cells in real and reciprocal space has been reported previously[27]. Two representative electron diffraction patterns from the 4.5 V charged sample collected along the $[45\bar{1}]_{Hex.}$ and $[81\bar{2}]_{Hex.}$ zone axes are shown in Figures 18a-b, respectively. Fundamental reflections of the parent structure are indexed while the superlattice reflections, which cannot be indexed consistently to the $\sqrt{3}\boldsymbol{a}_{Hex.} \times \sqrt{3}\boldsymbol{a}_{Hex.} \times \boldsymbol{c}_{Hex.}$ supercell, are marked by white stars

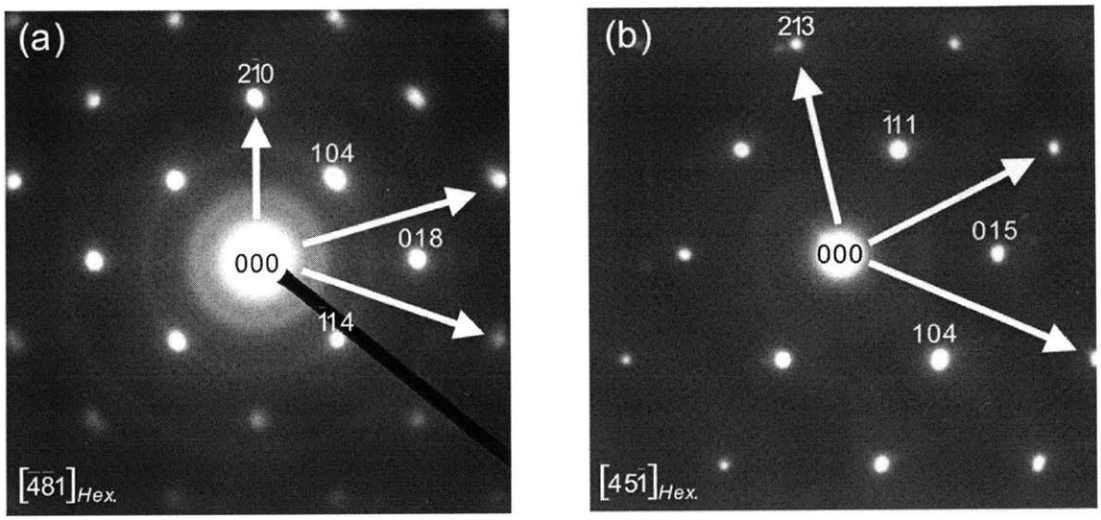

Figure 17: Experimental electron diffraction patterns exhibiting only fundamental reflections collected (a) from a $Li_{0.2}Ni_{0.5}Mn_{0.5}O_2$ sample charged to 4.5 V with $[\bar{4}\bar{8}1]_{Hex.}$ zone axis, (b) and from a $Li_0Ni_{0.5}Mn_{0.5}O_2$ sample charged to 5.3 V with $[45\bar{1}]_{Hex.}$ zone axis. Superlattice reflections consistent with a $\sqrt{3}\boldsymbol{a}_{Hex.} \times \sqrt{3}\boldsymbol{a}_{Hex.} \times \boldsymbol{c}_{Hex.}$ supercell in the marked planes have disappeared.

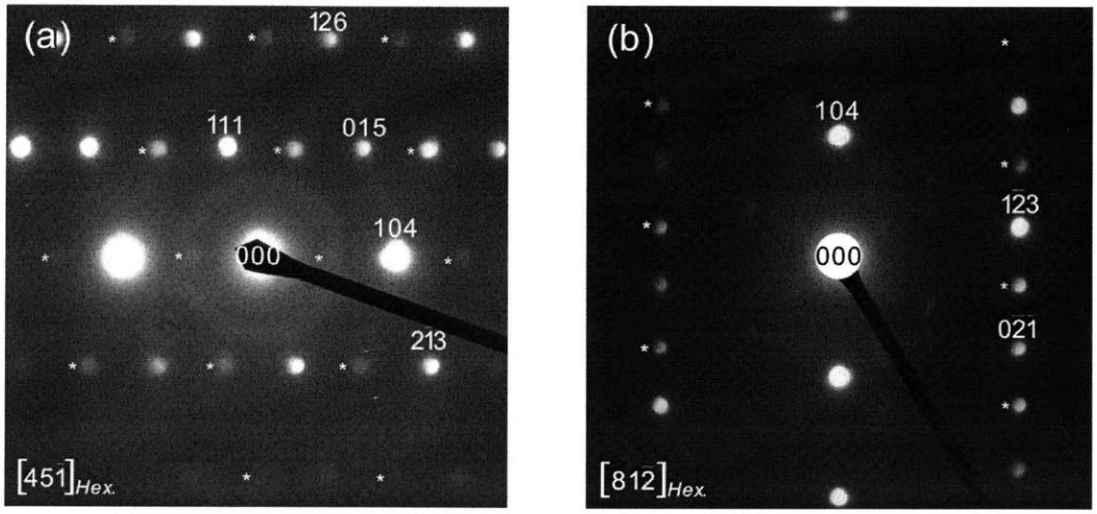

Figure 18: Experimental electron diffraction patterns exhibiting intense doubling superlattice reflections collected from the charged $Li_{0.2}Ni_{0.5}Mn_{0.5}O_2$ sample to 4.5 V along the (a) $[45\bar{1}]_{Hex.}$ zone axis, and the (b) $[81\bar{2}]_{Hex.}$ zone axis.

(Figures 19a-b). These types of superlattice reflections were found to coexist with those of the $\sqrt{3}\boldsymbol{a}_{\text{Hex.}} \times \sqrt{3}\boldsymbol{a}_{\text{Hex.}} \times \boldsymbol{c}_{\text{Hex.}}$ supercell in some crystals of the 4.5 V charged sample. In addition, the doubling superlattice reflections of the $(104)_{\text{Hex.}}$ plane were either weak in comparison to the other superlattice reflections (Figure 18a) or not visible (Figure 18b) in the 4.5 V charged sample. Similar superlattice reflections were found in fewer crystals of the 5.3 V charged sample, and two representative patterns of this sample are shown in Figures 20a-b, which are indexed to the $[\bar{2}\,\bar{1}\,\bar{1}]_{\text{Hex.}}$ and $[241]_{\text{Hex.}}$ zone axes, respectively. They cannot be indexed consistently to the $\sqrt{3}\boldsymbol{a}_{\text{Hex.}} \times \sqrt{3}\boldsymbol{a}_{\text{Hex.}} \times \boldsymbol{c}_{\text{Hex.}}$ supercell (Figures 21a-b). This type of doubling superlattice reflections was found predominant in the 4.5 V charged sample, where ~42 % of the crystals were found to exhibit these superlattice reflections as compared to only ~12 % for the 5.3 V charged sample.

3.2.3 Appearance of Extra Reflections for the O1 $\boldsymbol{a}_{\text{Hex.}} \times \boldsymbol{a}_{\text{Hex.}} \times \boldsymbol{c}_{\text{Hex.}}$ Cell

Additional reflections (marked by white stars), indicative of a primitive $\boldsymbol{a}_{\text{Hex.}} \times \boldsymbol{a}_{\text{Hex.}} \times \boldsymbol{c}_{\text{Hex.}}$ cell, were found in the $[001]_{\text{Hex.}}$ pattern collected from the 5.3 V charged sample, as shown in Figure 22a. The pattern cannot be indexed to the $\sqrt{3}\boldsymbol{a}_{\text{Hex.}} \times \sqrt{3}\boldsymbol{a}_{\text{Hex.}} \times \boldsymbol{c}_{\text{Hex.}}$ supercell. These extra reflections were found one-third-way between the diffraction center and the $(300)_{\text{Hex.}}$ fundamental reflections, and can be indexed consistently to the O1 structure with AB AB AB... oxygen packing having the space group $P\bar{3}m1$ (Figure 23). Electron diffraction evidence of the O1 formation in the 5.3 V charged $Li_0Ni_{0.5}Mn_{0.5}O_2$ sample is further supported by recent synchrotron X-ray diffraction data, which reveal three small diffraction peaks unique to the O1 phase and the coexistence of the primary O3 and the minor O1 phases in the 5.3 V charged sample[2]. It should be

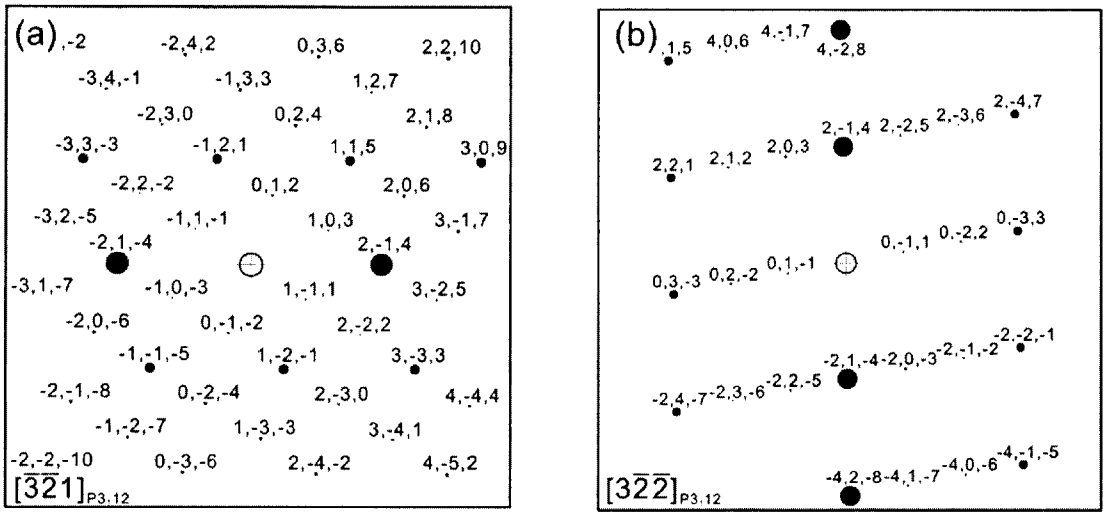

Figure 19: Simulated electron diffraction patterns of the experimental patterns in Figure 18 collected from the pristine $LiNi_{0.5}Mn_{0.5}O_2$ sample with (a) $[45\bar{1}]_{Hex.}$ zone axis, and (b) $[81\bar{2}]_{Hex.}$ zone axis.

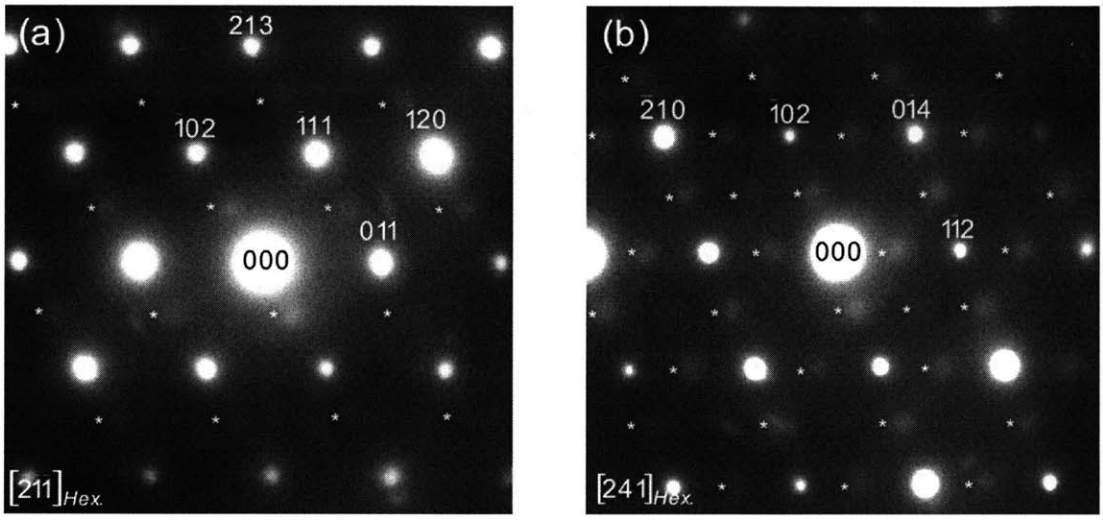

Figure 20: Experimental electron diffraction patterns exhibiting doubling superlattice reflections collected from the charged $Li_0Ni_{0.5}Mn_{0.5}O_2$ sample to 5.3 V along the (a) $[\bar{2}\bar{1}\bar{1}]_{Hex.}$ zone axis, and the (b) $[241]_{Hex.}$ zone axis.

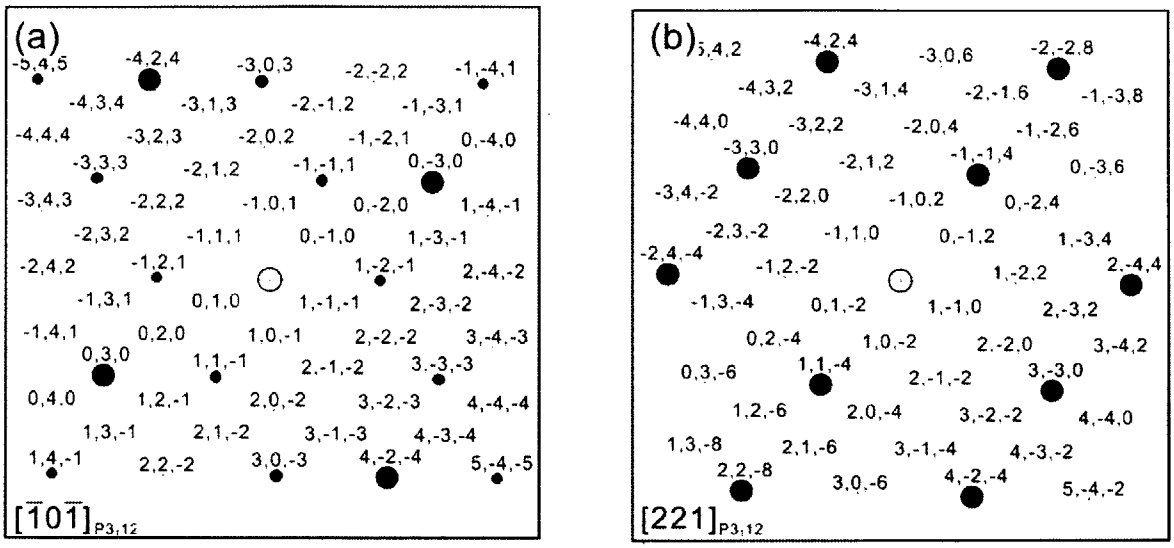

Figure 21: Simulated electron diffraction patterns of the experimental patterns in Figure 20 collected from the charged $Li_0Ni_{0.5}Mn_{0.5}O_2$ sample to 5.3 V along the (a) $[\bar{2}\bar{1}\bar{1}]_{Hex.}$ zone axis, and (b) $[241]_{Hex.}$ zone axis.

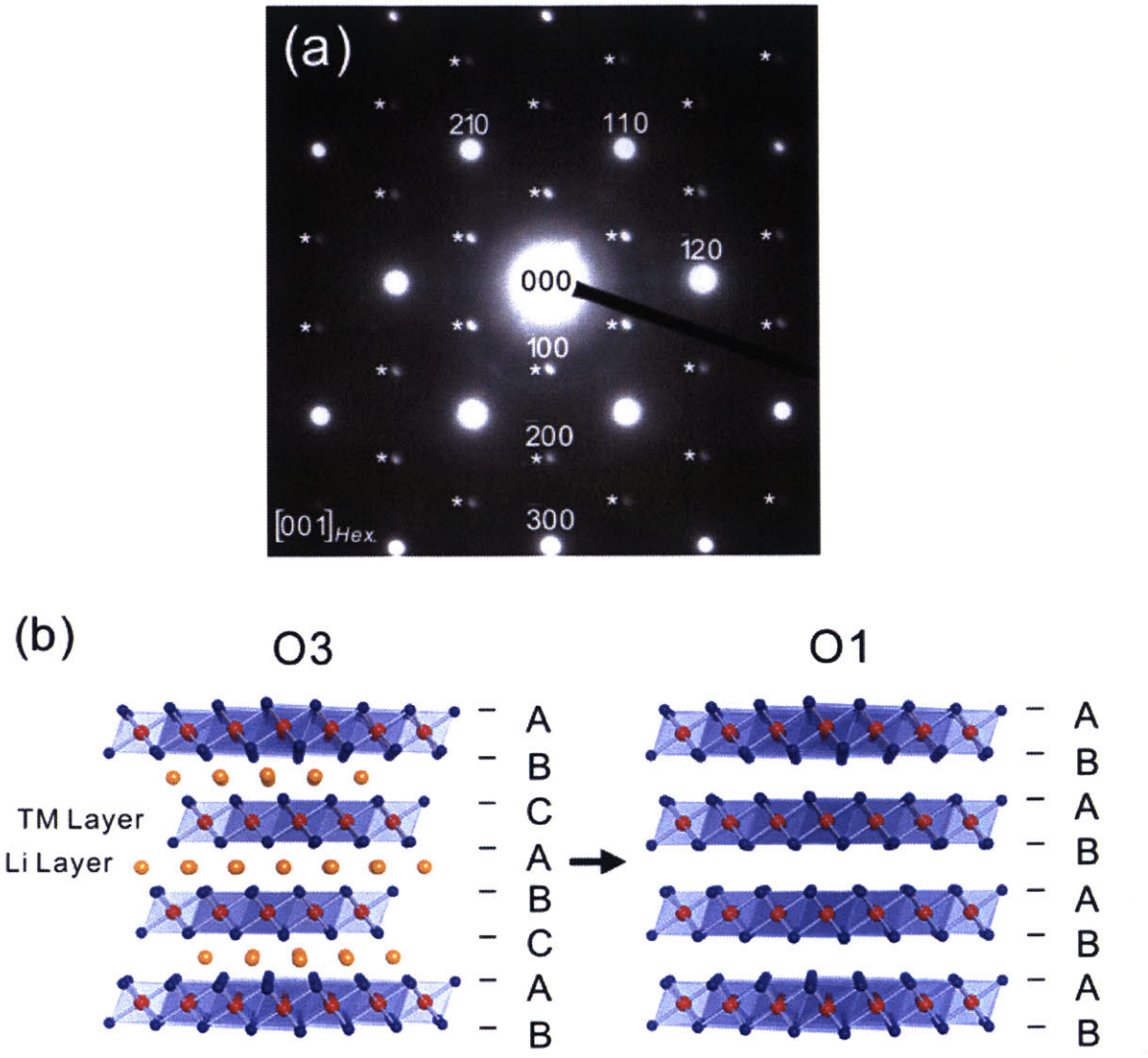

Figure 22: (a) Experimental electron diffraction patterns of the O1 phase collected from the charged $Li_0Ni_{0.5}Mn_{0.5}O_2$ sample to 5.3 V with the $[001]_{Hex.}$ zone axis. (b) Structural diagram of the O3 to O1 transition.

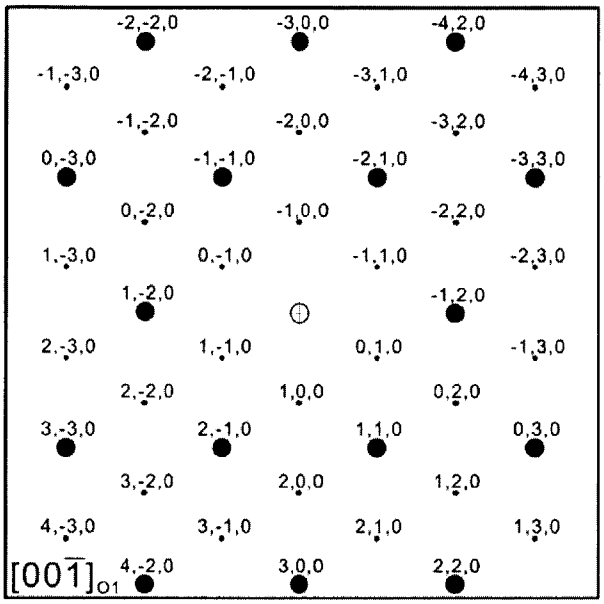

Figure 23: Simulated electron diffraction patterns of the O1 phase collected from the charged $Li_0Ni_{0.5}Mn_{0.5}O_2$ sample to 5.3 V with the $[001]_{Hex.}$ zone axis.

noted that both the electron diffraction and synchrotron X-ray diffraction data are not consistent with the H1-3 structure. The O1 phase was not so clearly observed in the neutron diffraction study of the 5.3 V charged sample because most of the reflections unique to O1 were hidden under the reflections of graphite[1]. Careful inspection of the diffraction pattern did, however, reveal the presence of a small concentration of the O1 phase. Removal of all Li ions in the Li layer leads to the sliding of transition metal slabs that forms the O1 structure with hexagonal-close-packed oxygen arrays, which is shown in Figure 22b. As expected, the O1 phase was not found in the 4.5 V charged sample ($Li_{0.2}Ni_{0.5}Mn_{0.5}O_2$) as a considerable amount of Li remains in the layered structure. The observation of the O1 phase is consistent with Ni migration from the Li layers, as any residual Ni would be expected to pin the transition metal slabs and prevent the O1 formation. Electron diffraction simulation analyses show that the parent O3 structure with space group $R\bar{3}m$ and the O1 phase with space group $P\bar{3}m1$ have similar patterns along many zone axes, which cannot be distinguished by the electron diffraction data of this study. Therefore, patterns that have zone axes other than $[001]_{Hex.}$ and do not exhibit any superlattice reflections can be indexed to either the O3 or the O1 structure.

3.3 Electrochemically Discharged $Li_xNi_{0.5}Mn_{0.5}O_2$ Samples

Electron diffraction patterns were collected from 25 randomly selected crystals of the discharged $Li_{0.9}Ni_{0.5}Mn_{0.5}O_2$ sample to 4.5 V and 20 crystals from the discharged $Li_{x>0.76}Ni_{0.5}Mn_{0.5}O_2$ sample to 5.3 V. Similar types of superlattice reflections were observed in the discharged samples as compared to the charged samples. It was found that ~80 % and ~55 % of the crystals exhibited the $\sqrt{3}\boldsymbol{a}_{Hex.} \times \sqrt{3}\boldsymbol{a}_{Hex.} \times \boldsymbol{c}_{Hex.}$ superlattice

reflections in the 4.5 V and 5.3 V discharged samples, respectively. In addition, ~28 % of the crystals from the 4.5 V discharged sample and ~35 % of the crystals from the 5.3 V discharged sample showed doubling superlattice reflections, which are indicative of cation ordering in a hexagonal $2\boldsymbol{a}_{Hex.} \times 2\boldsymbol{a}_{Hex.} \times \boldsymbol{c}_{Hex.}$ supercell or a monoclinic $\boldsymbol{a}_{Mon.} \times \boldsymbol{a}_{Mon.} \times \boldsymbol{c}_{Mon.}$ primitive cell. Moreover, none of the patterns collected from the discharged samples exhibited the additional reflections that are consistent with the O1 structure.

3.4 Extensively Cycled Discharged $Li_{0.8}Ni_{0.5}Mn_{0.5}O_2$ Samples

Similar types of superlattice reflections as the cycled samples were observed in the electron diffraction patterns of the extensively cycled $Li_{0.8}Ni_{0.5}Mn_{0.5}O_2$ sample in the discharged state after 21 cycles between 4.5 V and 2.0 V at the following rates: 5 cycles at C/50, 5 cycles at C/20, 5 cycles at C/10, 5 cycles at C/2, and 1 cycle at C/50. The only difference is in the fractions of crystals that exhibited each types of the superlattice reflections. One of the 20 crystals showed the O1 phase. ~25 % of the crystals exhibited the $\sqrt{3}\boldsymbol{a}_{Hex.} \times \sqrt{3}\boldsymbol{a}_{Hex.} \times \boldsymbol{c}_{Hex.}$ superlattice reflections and ~40 % of the crystals exhibited the doubling superlattice reflections, which are indicative of cation ordering in a hexagonal $2\boldsymbol{a}_{Hex.} \times 2\boldsymbol{a}_{Hex.} \times \boldsymbol{c}_{Hex.}$ supercell or a monoclinic $\boldsymbol{a}_{Mon.} \times \boldsymbol{a}_{Mon.} \times \boldsymbol{c}_{Mon.}$ primitive cell.

4.0 DISCUSSION

4.1 Evidence of Ni Migration Upon Cycling

4.1.1 Ni Migration from the Li to the Transition Metal Layer Upon Charging

In the pristine $LiNi_{0.5}Mn_{0.5}O_2$ sample, Li, Mn, and Ni ions in the transition metal layer are ordered into Li-rich and Li-deficient sites in the trigonal lattice, as shown in Figure 24a. The contrast in the average scattering intensities of these two sites gives rise to the $\sqrt{3}\boldsymbol{a}_{Hex.} \times \sqrt{3}\boldsymbol{a}_{Hex.} \times \boldsymbol{c}_{Hex.}$ superlattice reflections as shown in Figures 13a-b and in previous studies[23, 24]. Li MAS NMR studies[8] have revealed that Li ions can be removed from both the Li and the transition metal layers, and that all of the Li ions in the transition metal layer can be removed upon charging to $Li_{0.4}Ni_{0.5}Mn_{0.5}O_2$. De-intercalated Li ions create vacant sites in the transition metal layers, which would slightly increase the contrast in the average scattering factor between these two sites, and would lead to increased intensities of the $\sqrt{3}\boldsymbol{a}_{Hex.} \times \sqrt{3}\boldsymbol{a}_{Hex.} \times \boldsymbol{c}_{Hex.}$ superlattice reflections. However, the weakening and disappearance of these superlattice reflections were observed experimentally. This might be attributed to the following two scenarios upon charging: 1) in-plane movements of the Ni and the Mn ions in the transition metal layer, which result in a random distribution of Ni, Mn, and vacancies; 2) Ni migration from the Li layer to fill the vacant sites left behind by the de-intercalated Li ions in the transition metal layer (Figure 25). Both cases would decrease the contrast in the average scatting intensity between these two sites in comparison to that of the pristine sample, as illustrated in Figure 24b. Synchrotron X-ray powder diffraction analyses[2] of these charged samples reveal a significant increase in the Ni occupancy (octahedral 3a sites) of the transition metal layer. Cation occupancies in the octahedral and tetrahedral sites

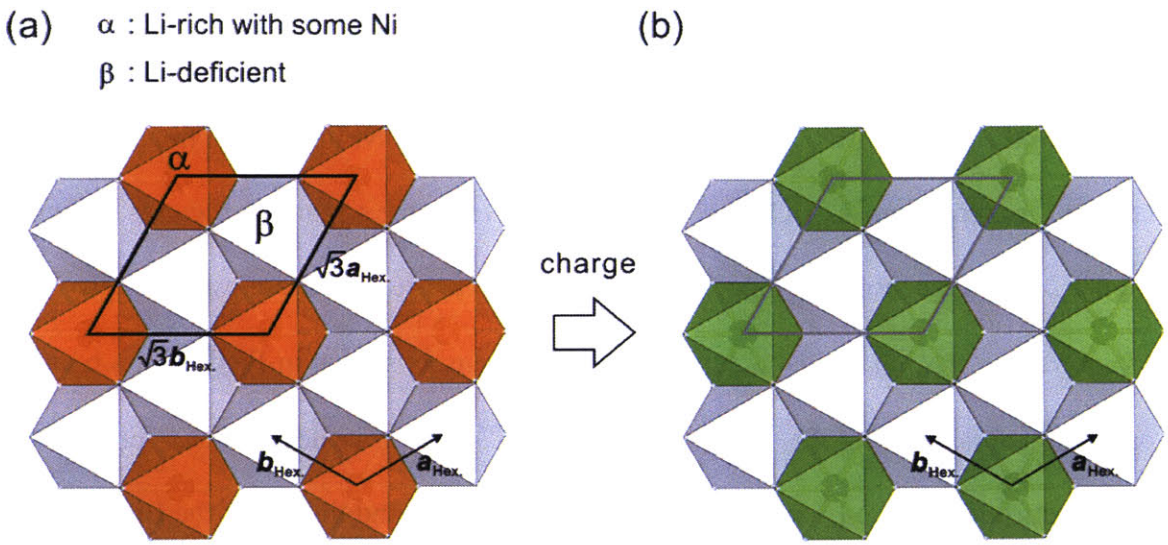

Figure 24: Changes in the cation ordering of the transition metal layer as Ni ions migrate into available vacancy sites upon charge. The intensity reduction of the superlattice reflections is a result of the decreasing contrast between the alpha and beta sites.

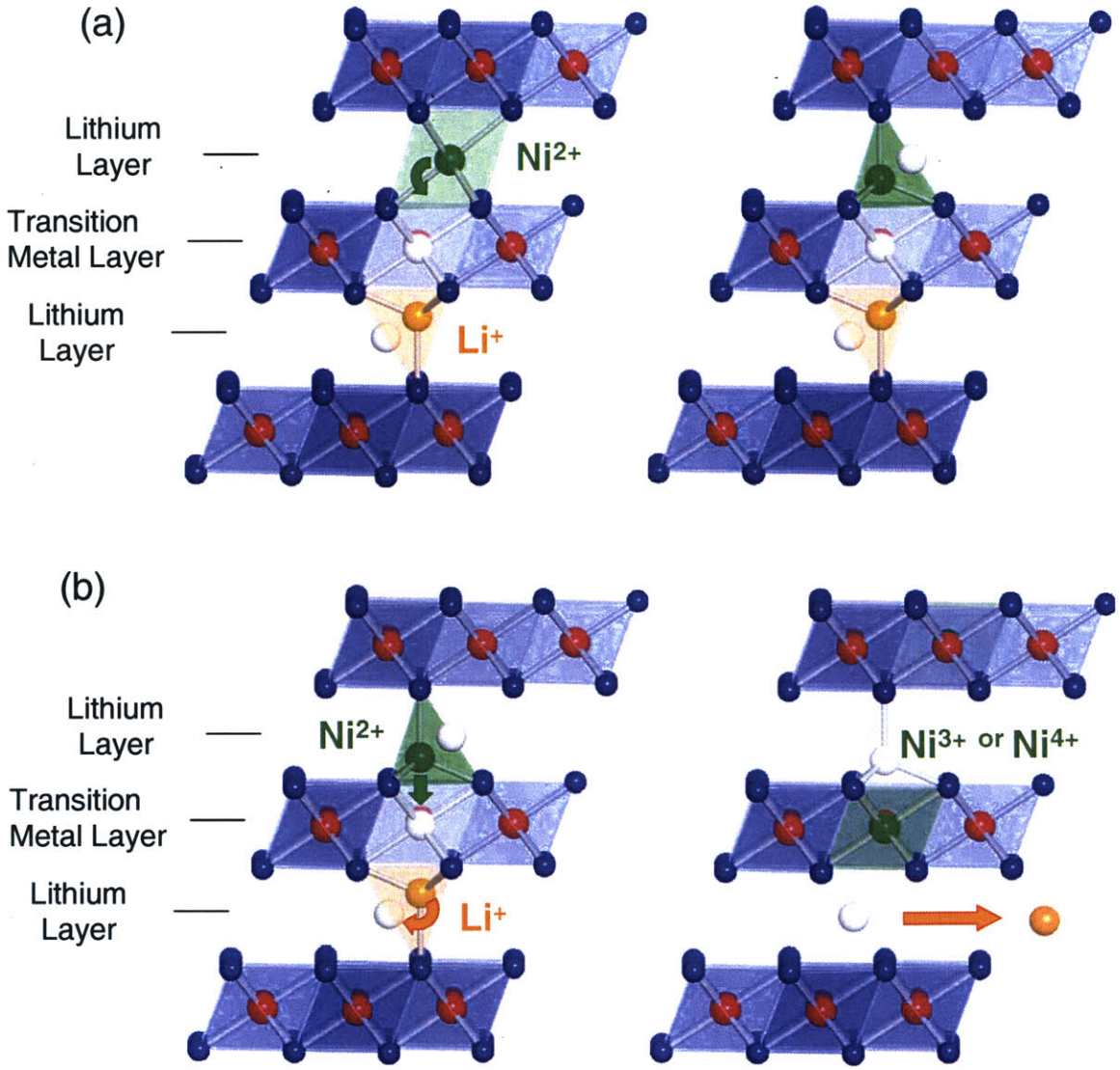

Figure 25: (a) Hopping Ni^{2+} ions from an octahedral site in the Li layer to a tetrahedral site that is adjacent to three vacant octahedral sites in the Li layer and one vacant octahedral site in the transition metal layer; and (b) Ni migration from the tetrahedral site into the vacant, face-sharing octahedral site in the transition metal layer upon Ni oxidation and Li removal.

found in the pristine and 4.5 V charged ($Li_{0.2}Ni_{0.5}Mn_{0.5}O_2$) samples are compared in Figure 26a. Therefore, both synchrotron X-ray powder diffraction and electron diffraction results agree that the onset of Ni migration from the Li layer to the vacant sites of the transition metal layer is by charging to 4.5 V. Oxidation of the Ni^{2+} ions in the Li layer, having similar ionic radii to Li^+ ions, to smaller Ni^{3+} (0.56 Å) or Ni^{4+} (0.48 Å) ions is not favored for the Ni ions in the Li layer. In particular, the Li (LiO_2) slab space is increased considerably upon charging (~6 % to 4.5 V), while the transition metal slab space is reduced (~6 % to 4.5 V), as shown in Figure 26b. Ni^{3+} and Ni^{4+} ions are more stable in the transition metal layer in the samples charged to these high voltages, and drive Ni migration from the Li to the transition metal layer.

The fraction of crystals exhibiting the $\sqrt{3}\boldsymbol{a}_{Hex.} \times \sqrt{3}\boldsymbol{a}_{Hex.} \times \boldsymbol{c}_{Hex.}$ superlattice reflections is indicative of the amount of Ni ions that have migrated into the transition metal layer. This fraction is significantly reduced in the 4.5 V charged sample, as shown in Figure 27, which is consistent with the increased Ni occupancy in the transition metal layer from Rietveld refinement in Figure 26a. However, recent neutron diffraction analyses showed no evidence for significant Ni migration to the transition metal layer in an electrode sample charged to 4.6 V. As the extent of Ni migration is strongly correlated to the Li content and the valence state of Ni in $Li_xNi_{0.5}Mn_{0.5}O_2$, this discrepancy can be attributed to the fact that the charged sample used for neutron diffraction had a considerably higher Li content ($Li_{0.33}Ni_{0.5}Mn_{0.5}O_2$) than the electrode ($Li_{0.2}Ni_{0.5}Mn_{0.5}O_2$) charged to 4.5 V in this study. Moreover, the fraction of crystals having the $\sqrt{3}\boldsymbol{a}_{Hex.} \times \sqrt{3}\boldsymbol{a}_{Hex.} \times \boldsymbol{c}_{Hex.}$ superlattice reflections in the 5.3 V charged

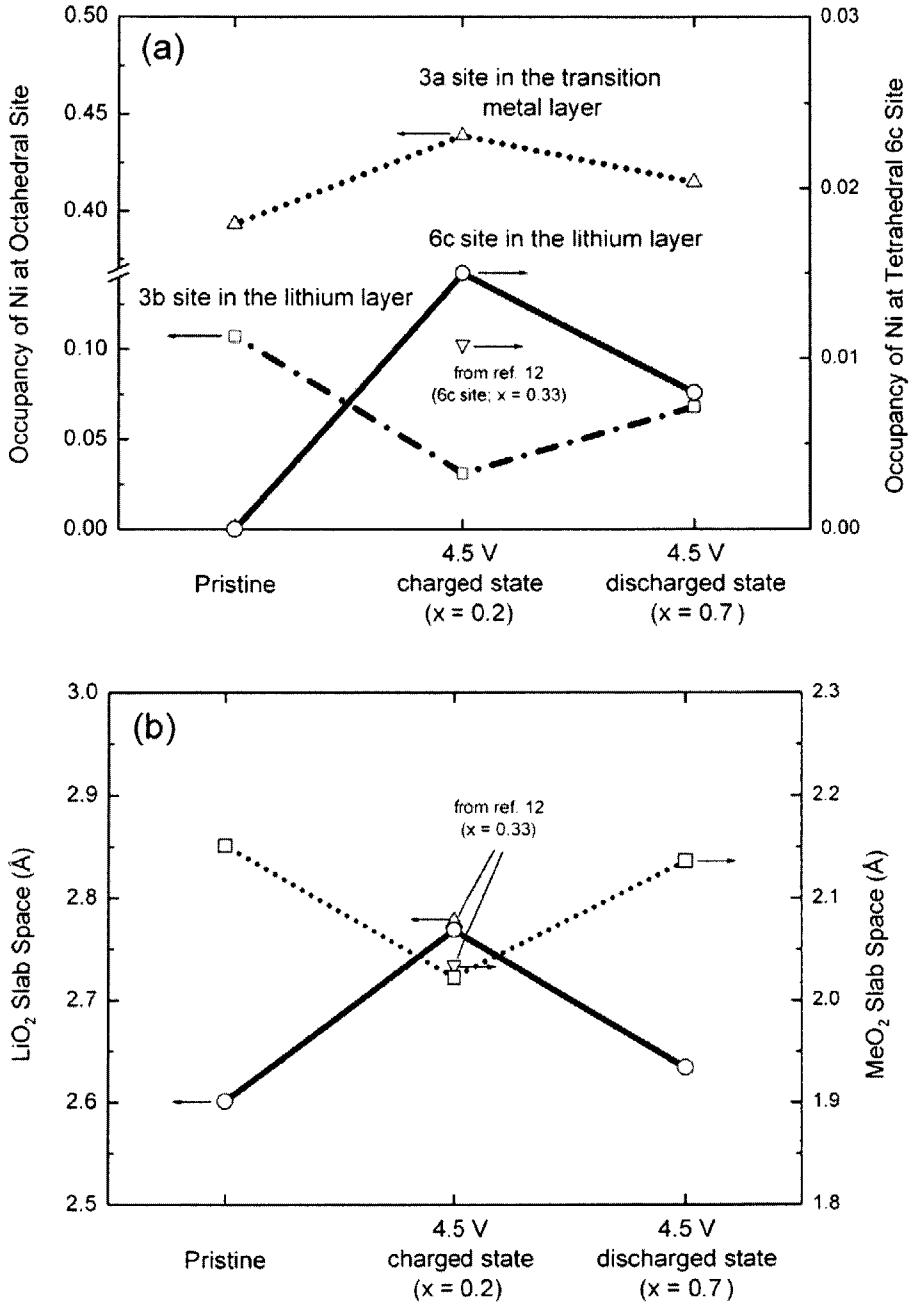

Figure 26: (a) Ni occupancy in the octahedral and tetrahedral sites and (b) the change in LiO_2 and MeO_2 slab space from Rietveld analysis of the pristine, charged 4.5 V, and discharged 4.5 V samples.

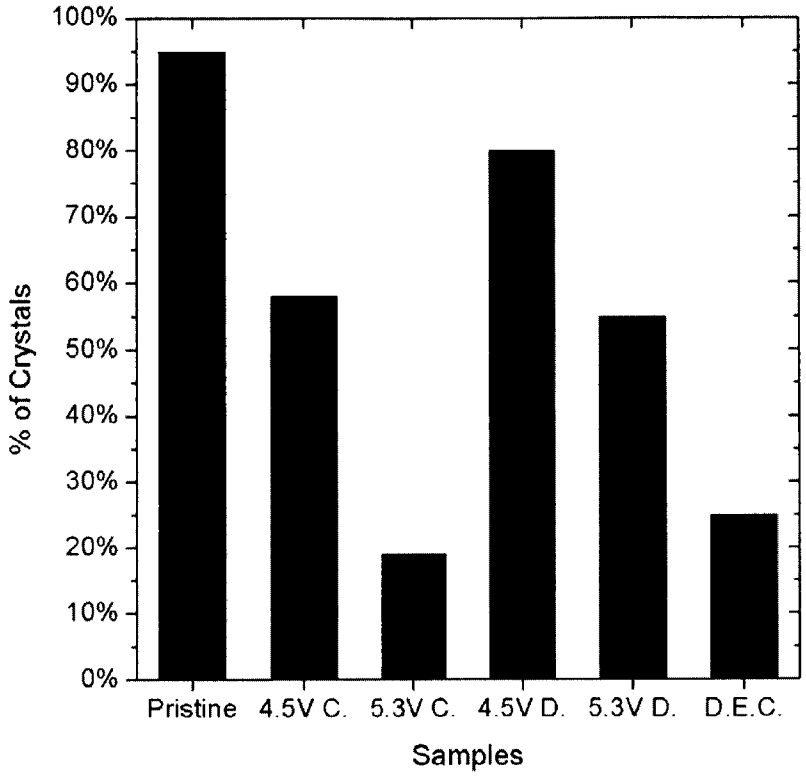

Figure 27: Comparison of the percentage of crystals exhibiting the $\sqrt{3}\boldsymbol{a}_{\text{Hex.}} \times \sqrt{3}\boldsymbol{a}_{\text{Hex.}} \times \boldsymbol{c}_{\text{Hex.}}$ type superlattice reflections in the pristine, 4.5 V charged, 5.3 V charged, 4.5 V discharged, 5.3 V discharged, and extensively cycled 4.5 V discharged samples.

$Li_0Ni_{0.5}Mn_{0.5}O_2$ sample is considerably lower than that of the 4.5 V charged $Li_{0.2}Ni_{0.5}Mn_{0.5}O_2$ sample, as shown in Figure 27. This observation suggests that additional Ni ions migrate to the transition metal layer, and the interlayer mixing is further reduced upon charging from 4.5 V to 5.3 V. This finding from electron diffraction is in good agreement with the results of the synchrotron X-ray data (the appearance of the O1 phase in the 5.3 V charged sample (~10 % by volume))[2] and the neutron diffraction data (a decrease in the Ni concentration in the Li layers from ~10 % to ~2.4 % in a 5.2 V charged $Li_{0.06}Ni_{0.5}Mn_{0.5}O_2$ sample)[1].

The extent of Ni migration may be dependent on the Li content, the valence state of the Ni ions, and the local cation arrangements adjacent to the Ni ions in the Li layer. Upon charging to extremely high voltages such as 5.3 V, nearly all of the Li ions are removed, and almost all of the Ni ions are oxidized to Ni^{4+} by the end of charge. In this case, all of the Ni ions in the Li layer may be removed and displaced into the vacant octahedral sites in the transition metal layer as evidenced by the appearance of the O1 phase in the 5.3 V charged sample (Figure 22). Furthermore, Ni migration can occur at voltages lower than 4.5 V, as shown in Figures 26-27. Ni ions migrate from the Li layer to the transition metal layer via the tetrahedral sites, and the magnitude of voltage that can induce such Ni migration and Li removal may depend on the local cation arrangements of the Ni ions in the Li layer. If a Ni^{2+} ion were located in an octahedral site in the Li layer edged shared with a vacant octahedral site in the transition metal layer, it could hop into the tetrahedral site in the Li layer that is face sharing with the vacant octahedral site[29], and migrate into the vacant octahedral site in the transition metal layer upon oxidation without any energy barrier[1].

Two hypothetical structural models are discussed here to understand the process of Ni migration in the $Li_xNi_{0.5}Mn_{0.5}O_2$ structure. In the first case, one third of the octahedral sites in the transition metal layer are vacant, and are ordered into a $\sqrt{3}\boldsymbol{a}_{Hex.} \times \sqrt{3}\boldsymbol{a}_{Hex.} \times \boldsymbol{c}_{Hex.}$ supercell. In this super structure, every octahedral site in the Li layer can edge share with one octahedral vacancy in the transition metal layer, and Ni migration should be facile. In the second case, the flower structure model from first-principles studies is examined[1, 6]. In the flower structure, one twelfth of the octahedral sites in the transition metal layer are vacant, and the Ni ions in the Li layer are ordered in the octahedral sites that share corners with the octahedral vacancies in the transition metal layer. Migration of such Ni ions is kinetically difficult as they need to go through adjacent tetrahedral sites in the Li layer, which face share with three adjacent and filled octahedral sites in the Li layer. First-principles studies have shown that the activation barrier for Ni ions hopping through such tetrahedral sites is as high as 1 eV[1, 14]. The actual local environments of Ni in the charged $Li_xNi_{0.5}Mn_{0.5}O_2$ samples may fall in between these two structural models. The maximum fraction of vacant octahedral sites in the transition metal layer is 0.11 per formula unit as only 0.11 Li^+ per formula unit is displaced into the transition metal layer in the pristine sample (Figure 26a). This leads to a maximum of 0.22 per formula unit of available tetrahedral sites for Li and Ni occupancy in the charged samples. The voltage needed for Ni migration into these tetrahedral sites depends on how far away the Ni ions are located in the Li layer. Some of the Ni ions in the Li layer may share an edge with the octahedral vacancies in the transition metal layer, and can migrate at voltages lower than 4.5 V. Others that are positioned further from these vacancies would migrate upon charging to voltages higher

than 4.5 V. This argument is in agreement with the experimental observation that the Ni migration process occurs over a wide range of voltages upon charging (Figure 27).

4.1.2 Ni Migration from the Transition Metal to the Li Layer Upon Discharge

Ni migration appears to be in part reversible upon discharge. The fractions of the crystals with the $\sqrt{3}\boldsymbol{a}_{\text{Hex.}} \times \sqrt{3}\boldsymbol{a}_{\text{Hex.}} \times \boldsymbol{c}_{\text{Hex.}}$ superlattice reflections in the discharged samples are considerably higher than those of charged samples, as shown in Figure 27. This observation suggests that a fraction of the Ni ions that migrate into the transition metal layer upon charging moves back to the Li layer upon discharge, which is consistent with the decreasing Ni occupancy in the transition metal layer upon discharge (Figure 26a). It also means that the cycled samples in the discharge state have a reduced interlayer mixing and an increased Ni occupancy in the transition metal layer in comparison to the pristine sample. This result is consistent with recent neutron diffraction analyses of the discharged electrodes cycled to 4.8 V and 5.2 V[1], where the fraction of the Ni ions in the Li layer is reduced by ~4 % per formula unit relative to the pristine sample. Recent first-principles and NMR results have suggested that the stability of the Ni ions in the transition metal layer may decrease with increasing Mn^{4+} neighbors[1]. Therefore, Ni^{4+} surrounded by 6 Mn^{4+} are most likely to migrate back to the Li layer upon discharge.

After cycling to 5.3 V, fewer crystals in the discharged electrode exhibit the $\sqrt{3}\boldsymbol{a}_{\text{Hex.}} \times \sqrt{3}\boldsymbol{a}_{\text{Hex.}} \times \boldsymbol{c}_{\text{Hex.}}$ superlattice reflections in comparison to the 4.5 V discharged electrode (Figure 27). This observation suggests that more Ni ions are permanently displaced into the transition metal layer in the 5.3 V discharged sample in comparison to

electrodes cycled to 4.5 V. This is consistent with the observation by NMR that Li ions do not return to the transition metal layer after cycling to 5.3 V[1]. The electron diffraction observations are also in agreement with the electrochemical cycling results, which show that the electrodes first exposed to 5.3 V have improved reversible capacities and rate capability during the subsequent cycling to 4.5 V[2]. An increasing layered characteristic (reducing cation disorder or interlayer mixing) can enhance the rate capability of similarly layered compounds as shown by studies of ion-exchanged $LiNi_{0.5}Mn_{0.5}O_2$[14] and $LiNi_{0.56}Mn_{0.44}O_2$ samples[37] that have smaller amounts of cation disorder (~0.04 to 0.06 per formula unit). The physical origin of the difference in the Ni stability between the 4.5 V and 5.3 V charged samples is not fully understood. It is postulated that the structural differences between these two samples may influence the Ni stability in the adjacent and face-sharing tetrahedral sites in the Li layer upon discharge. The occupancy of Li (as revealed by recent neutron diffraction data[1]) and Ni (Figure 26a) ions in the tetrahedral sites of the Li layer in the 4.5 V charged sample results in a relatively large Li slab space, as shown in Figure 26b. Such a large Li slab space may allow the Ni ions to move out of the octahedral sites in the transition metal layer into the face-sharing tetrahedral sites in the Li layer upon reduction to Ni^{2+} during discharge, and then further migrate into the Li layer. The O1 phase has a much smaller distance between the adjacent transition metal layers (4.68 Å) than that found in the O3 structure of the 4.5 V charged sample (4.79 Å). Therefore, Ni ions in the transition metal layer are more stable under the O1 type structure as compared to the O3 type structure. Unfortunately, the Li slab space of the O1 $Li_0Ni_{0.5}Mn_{0.5}O_2$ phase could not be refined from the synchrotron X-ray powder diffraction data[2]. Previous studies have shown that

the O1 CoO_2[34] and O1 NiO_2[35, 36] structures exhibit a significantly reduced lattice parameter $c_{Hex.}$ than observed in the slightly intercalated phases. Although the oxygen parameters are not reported in these studies, one may deduce that the sudden change in the lattice parameter $c_{Hex.}$ could be a result of the considerable reduction in the Li slab space, assuming that the thickness of the transition metal slabs is primarily determined by the valence of Ni and Co, and thus would not differ significantly amongst the samples. Similarly, it is believed that the Li slab space in O1 is much smaller than that of the O3 structure in the 4.5 V charged sample. Therefore, it is hypothesized that the Li slab space of the O1 phase might be too small to allow Ni migration from the transition metal layer to the tetrahedral sites in the Li layer upon Li intercalation, and would stabilize the Ni ions in the transition metal layer upon discharge.

For the extensively cycled sample in the discharged state, a significantly smaller fraction of its crystals exhibits the $\sqrt{3}a_{Hex.} \times \sqrt{3}a_{Hex.} \times c_{Hex.}$ superlattice reflections in comparison to the 4.5 V and 5.3 V discharged electrodes (Figure 27). This observation suggests that even more Ni ions are permanently displaced into the transition metal layer of the extensively cycled sample in the discharged state (after 21 cycles). The amount of Ni occupancy in the transition metal layer is comparable to that of the 5.3 V charged sample (Figure 27). This observation suggests that in addition to exposure to high voltages, prolonged cycling would also induce less cation mixing or promote Ni migration in the material. As discussed previously, Ni ions migrate from the octahedral site in the Li layer to the tetrahedral site, and then to another octahedral site in the transition metal layer. However, it is also likely for the Ni ions to migrate back into the octahedral site in the Li layer from the tetrahedral site. Therefore, the extent of Ni

migration and its reversibility is also a function of probability. It is observed that upon cycling to many cycles, more and more Ni ions are accumulated in the transition metal layer. However, it is not well understood why the transition metal layer is preferred to the Li layer for Ni occupancy.

4.2 Effect of Ni Migration on $LiNi_{0.5}Mn_{0.5}O_2$'s Electrochemical Properties

In general, the presence of Ni ions in the Li layer of a layered structure reduces the number of vacant sites available for Li intercalation, and impedes the motion of Li ions as a result of the strong repulsive forces between the mobile Li ions and the fixed Ni ions[38-40]. Therefore, the excellent electrochemical activity and reversibility of $LiNi_{0.5}Mn_{0.5}O_2$ having ~0.11 Ni per formula unit in the Li layer may be attributed to the mobility of Ni ions upon electrochemical cycling. As suggested by the refinement results of the monoclinic O3 phase, a considerable amount of Ni ions migrated from the octahedral 3b sites to the octahedral 3a and tetrahedral 6c sites upon charging to 4.5 V (Table 1). Furthermore, the 5.3 V charged sample showed even better discharged capacities (Figure 6a). This may be explained by the 5.3 V charged sample having more vacant sites in the Li layer that are available for Li intercalation. In addition, the O1 phase is observed in the 5.3 V charged sample, which suggests that the number of Ni ions in the Li layer decreases upon further charging from 4.5 V to 5.3 V, and results in higher discharge capacities. On the other hand, in the discharged states, the extent of Li and Ni interlayer mixing in the electrodes cycled to 5.3 V is lower than that found in the electrodes cycled to 4.5 V (Table 1). As exposure to 5.3 V permanently reduces the extent of Li and Ni interlayer mixing, higher discharge capacities are observed when

comparing with electrodes that have only been cycled to 4.5 V under the same voltage range of 4.5 V and 2.0 V.

Li de-intercalation voltages of $Li/LiNi_{0.5}Mn_{0.5}O_2$ cells are lowered considerably from ~3.83 V in the first charge to ~3.75 V in the subsequent charges, as shown in Figures 7a-b and also in previous publications[16]. First-principles studies have shown that Li removal from the Li layer occurs at lower voltages than that from the transition metal layer[29]. Therefore, it is believed that the reduction in the Li de-intercalation voltage is due to the decrease in the number of electrochemically active Li ions in the transition metal layer upon cycling. Figures 7a-b show that the Li de-intercalation voltage decreases drastically from the first to the second cycle for the 5.3 V charged sample, but the decrease is gradual for the 4.5 V charged sample over many cycles. This difference may be attributed to the availability of vacancies on the 3a sites of the transition metal layer for Li ions to migrate back upon discharge. In the 5.3 V cycled sample, some Ni ions have permanently occupied these sites after the first cycle due to high voltage exposure. In contrast, this process is more gradual and needs multiple cycles to complete in the 4.5 V cycled sample[1].

A reversible process centered at ~4.3 V becomes pronounced after exposure to 5.3 V (Figures 7a and 8a) as Ni occupancy in the Li layer is reduced. The ~4.3 V plateau is clearly observed in the charge and discharge voltage profiles of an ion-exchanged $LiNi_{0.5}Mn_{0.5}O_2$ sample[14], which has a Li and Ni intermixing of ~4 % upon cycling to 4.6 V. Croguennec *et al.*[35, 36] have reported a similar reversible process at ~4.2 V upon Li de-intercalation from nearly stoichiometric $LiNiO_2$ samples, and have attributed this feature to the formation of the O1 type packing in the O3 structure. As the O1 phase is

detected in the electrode charged to 5.3 V (Figure 9c), it is believed that the ~4.3 V process may be associated with the O3 to O1 transformation in $Li_xNi_{0.5}Mn_{0.5}O_2$ at very low Li contents. On the other hand, when the material is cycled in the voltage range between 4.5 V and 2.0 V, the Li content (~0.2) of $Li_xNi_{0.5}Mn_{0.5}O_2$ at the end of charge and the number of Ni ions in the interslab space (on the octahedral 3b and tetrahedral 6c sites) are too high to allow the sliding of transition metal layers to form the O1 phase. Although Rietveld refinement cannot be performed for the O1 phase present, it is believed that the Ni occupancy is ~0.5 in the transition metal layer. The O3 to O1 transition occurs when all of the Ni ions on the octahedral 3b sites, which may serve as pillars to hold oxygen packing in the cubic-close-packed array, have migrated into the octahedral 3a sites in the transition metal layer upon complete Li de-intercalation. A proposed structure for the monoclinic O3 structure in the 5.3 V charged electrode is shown in Figure 28b to illustrate the transition to the O1 oxygen packing with all of the Li and Ni ions removed from the interslab space.

4.3 Evidence of Li, Ni, and Vacancies Ordering in the Cycled $Li_xNi_{0.5}Mn_{0.5}O_2$ Samples

Figure 29 summarizes the fractions of crystals found in the cycled samples in both the charged and discharged states which exhibit the doubling superlattice reflections. These superlattice reflections can be indexed to either a hexagonal $2\boldsymbol{a}_{Hex.} \times 2\boldsymbol{a}_{Hex.} \times \boldsymbol{c}_{Hex.}$ supercell with space group $R\bar{3}m$ or a monoclinic $\boldsymbol{a}_{Mon.} \times \boldsymbol{a}_{Mon.} \times \boldsymbol{c}_{Mon.}$ primitive cell with space group P2/m. The ordering of Li, Ni, and vacancies in the tetrahedral and octahedral sites of the Li layer may give rise to the appearance of these superstructures, as shown in Figures 30a-d. To understand the origin of these superstructures, four

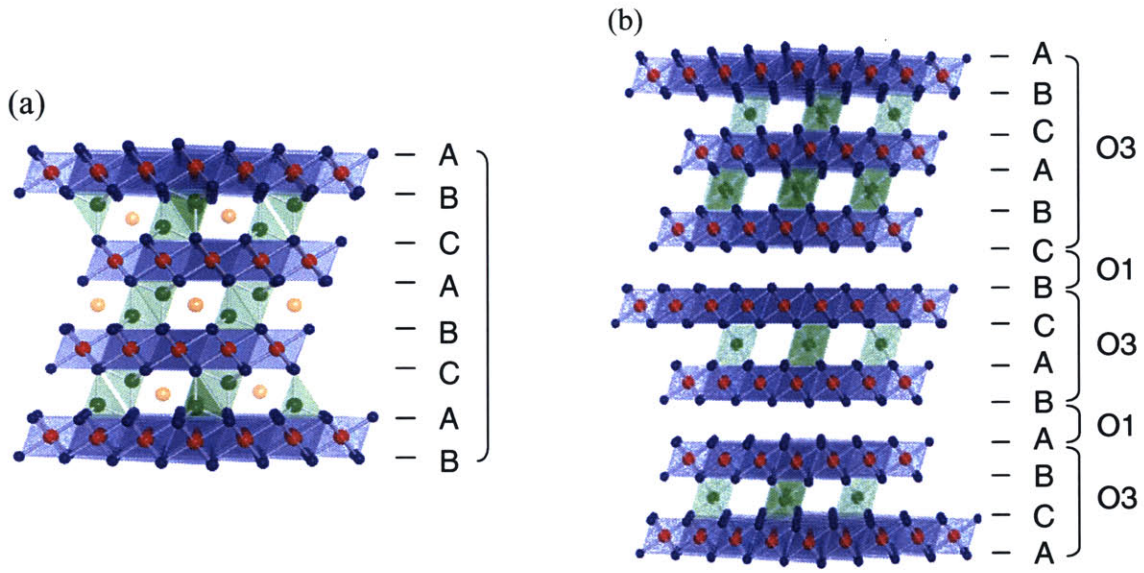

Figure 28[2]: Proposed structural models of (a) a rhombohedral O3 $Li_xNi_{0.5}Mn_{0.5}O_2$ in the 4.5 V charged electrode, where the Li and Ni ions are randomly distributed on the 3b and 6c sites in the interslab space. Note that vacancies in the transition metal layer (not shown) are required to accommodate the tetrahedral occupancy of Li and/or Ni; and (b) a monoclinic O3 found in the 5.3 V charged electrode, where some Ni ions are located on the octahedral 3b sites (interslab space), which stabilizes the O3-type oxygen packing.

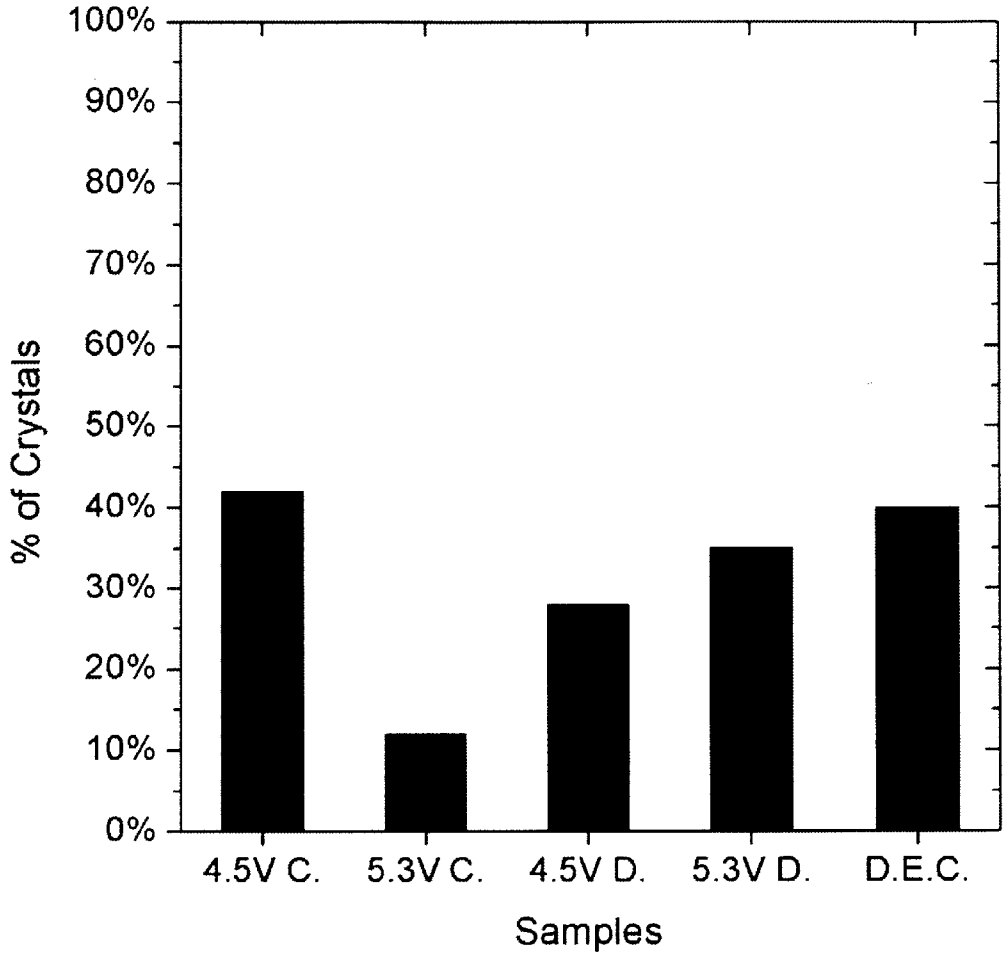

Figure 29: Comparison of the percentage of crystals that exhibit doubling superlattice reflections in the pristine, 4.5 V charged, 5.3 V charged, 4.5 V discharged, 5.3 V discharged samples, and extensively cycled 4.5 V discharged samples.

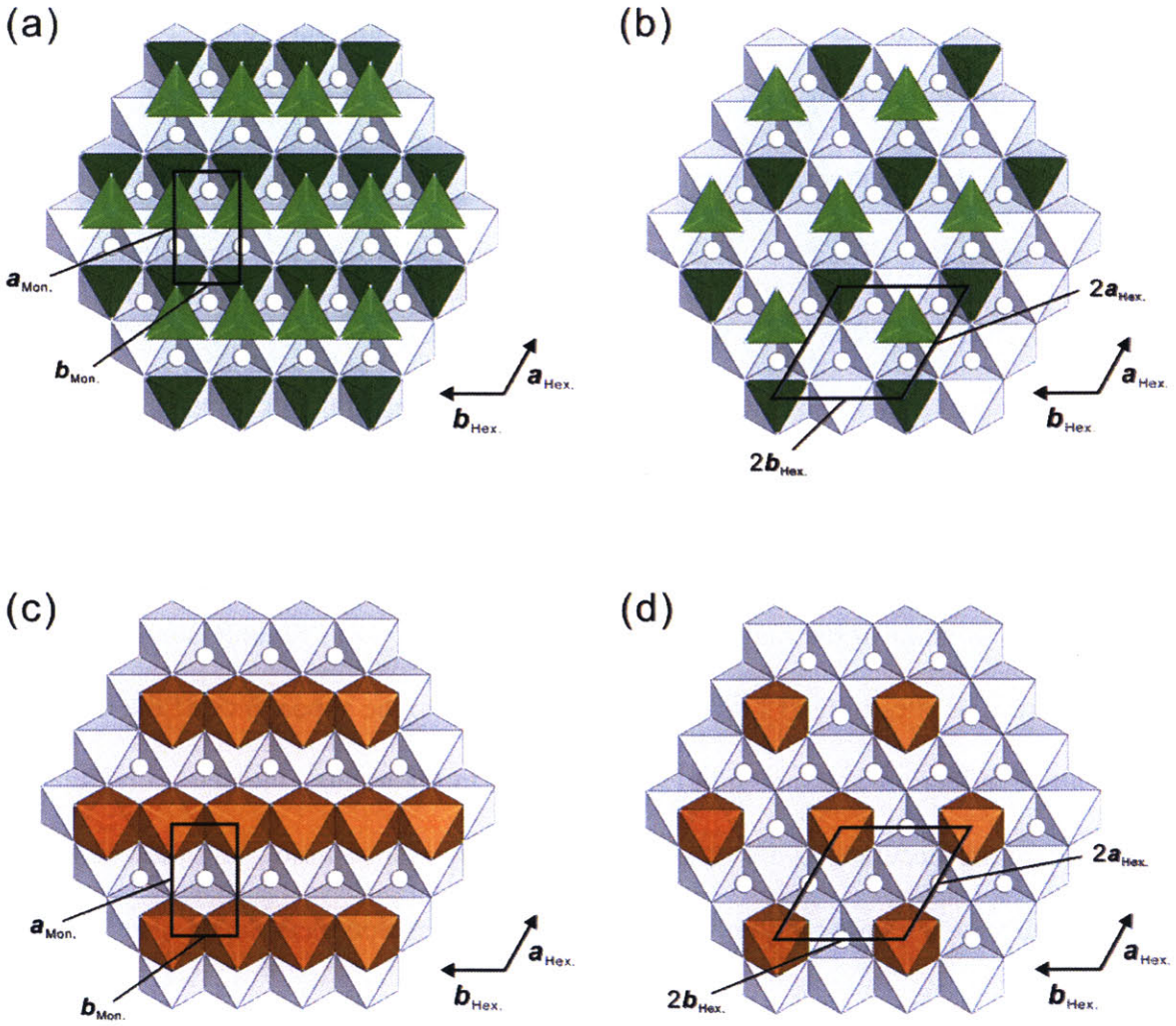

Figure 30: (a) Schematic of tetrahedral site ordering under the P2/m symmetry. (b) Schematic of tetrahedral site ordering under the R $\bar{3}m$ symmetry. (c) Schematic of octahedral site ordering under the P2/m symmetry. (d) Schematic of octahedral site ordering under the R $\bar{3}m$ symmetry.

different structural models including cation-rich and cation-deficient sites with full or partial occupancy are proposed. In the first model, upper (pointing down) and lower (pointing up) tetrahedral sites are occupied by Li or Ni in every other row, and the octahedral sites in the Li layer are marked by white spheres, as shown in Figure 30a. In this scheme, the octahedral cations and vacancies are randomly distributed in the transition metal and Li layers. Such ordering can be described by a monoclinic $\boldsymbol{a}_{\text{Mon.}} \times \boldsymbol{a}_{\text{Mon.}} \times \boldsymbol{c}_{\text{Mon.}}$ cell with space group P2/m. In Figure 30b, there are fully emptied and half occupied rows of upper and lower tetrahedral sites, respectively, and octahedral ions and vacancies randomly distributed in the transition metal and Li layers. This type of ordering can be described by a hexagonal $2\boldsymbol{a}_{\text{Hex.}} \times 2\boldsymbol{a}_{\text{Hex.}} \times \boldsymbol{c}_{\text{Hex.}}$ supercell with space group $R\bar{3}m$. Similar to the tetrahedral site ordering as shown in Figures 30a-b, ordering in the octahedral sites of the Li layer may also give rise to the appearance of the doubling superlattice reflections, as shown in Figures 30c-d. In Figure 30c, the octahedral sites of the Li layer are occupied every other row (1 Li to 1 vacancy ratio), and the octahedral cations and vacancies are randomly distributed in the transition metal layer. The ordering in Figure 30c can be described by a monoclinic $\boldsymbol{a}_{\text{Mon.}} \times \boldsymbol{a}_{\text{Mon.}} \times \boldsymbol{c}_{\text{Mon.}}$ cell with space group P2/m. Similar ordering configurations have been reported for also $Li_{0.5}CoO_2$[27] and $Li_{0.5}NiO_2$[28, 33]. In Figure 30d, the octahedral sites are occupied every other row, and within each occupied row every other octahedral sites are filled, and the octahedral ions and vacancies are randomly distributed in the transition metal layer. The ordering can be described by a hexagonal $2\boldsymbol{a}_{\text{Hex.}} \times 2\boldsymbol{a}_{\text{Hex.}} \times \boldsymbol{c}_{\text{Hex.}}$ supercell with space group $R\bar{3}m$ (Figure 30d). This superstructure has been reported for $Li_{0.25}NiO_2$[28], which consists of a 1 Li to

3 vacancies type ordering. The same supercell has also been proposed for $Li_{0.75}NiO_2$, which consists of a 3 Li to 1 vacancy type ordering[28].

Simulated electron diffraction patterns along the equivalent zone axes of these four ordered structures are compared with the experimental patterns exhibiting the doubling superlattice reflections. One differentiating feature in the simulated electron diffraction patterns of these superstructures is the doubling superlattice reflection of the $(104)_{Hex.}$ fundamental reflection. The doubling superlattice reflection's intensity relative to the other superlattice reflections is different amongst the models, for a given fraction of the transition metal ions on the octahedral and tetrahedral sites. In the case of tetrahedral site ordering, the intensity of the $(104)_{Hex.}$ doubling superlattice reflection is zero under the following two assumptions. First, the cations and oxygen ions are located in the ideal positions of the tetrahedral sites (oxygen: 6c site z = 1/4 and cations: 6c site z = 1/8). Second, the average occupancies of the cations in the upper and lower tetrahedral sites are identical. If the previous two conditions are not met, then weak $(104)_{Hex.}$ doubling superlattice reflections would be observed. In contrast, octahedral site ordering results in strong $(104)_{Hex.}$ doubling superlattice reflections. In comparison to the other superlattice reflections, the $(104)_{Hex.}$ doubling superlattice reflection is the second strongest, with the $(102)_{Hex.}$ doubling superlattice reflection being the strongest. The origin of this difference in intensity can be visualized in the structural projections along the $[010]_{Hex.}$ direction as shown in Figures 31a-c. In Figure 31a, the ordering of the tetrahedral sites do not change the periodicity of the $(104)_{Hex.}$ planes if the cation and oxygen positions are ideal. Therefore, the doubling superlattice reflections of the $(104)_{Hex.}$ plane are not expected. If the cation and oxygen positions are not ideal, then

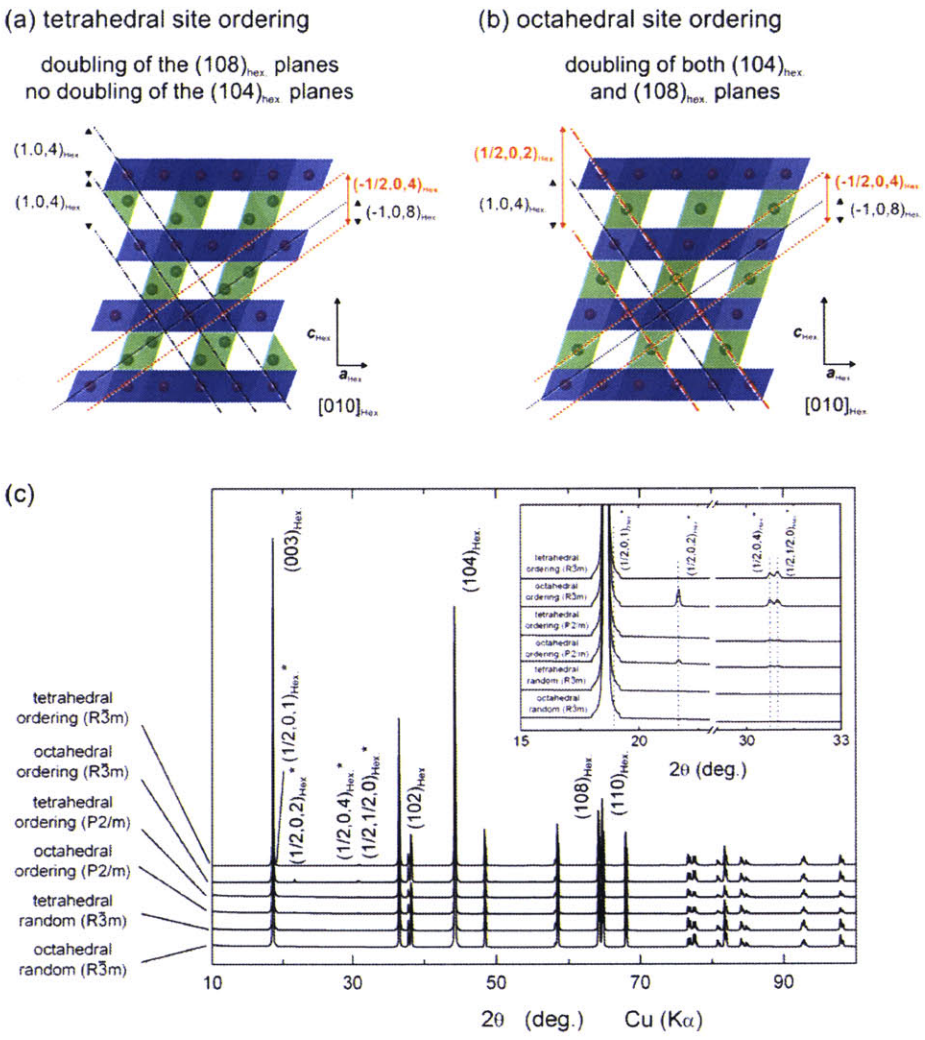

Figure 31: Schematic illustrations of the crystal structure of $Li_xNi_{0.5}Mn_{0.5}O_2$ projected along the $[010]_{Hex.}$ zone axis. Cation ordering that results in (a) doubling of $(104)_{Hex.}$ plane, and (b) no doubling of $(104)_{Hex.}$ plane. The key to the disappearance of $(104)_{Hex.}$ doubling superlattice reflection is cation ordering in the tetrahedral sites. (c) Simulated XRD patterns with the models shown in Figure 30.

weak $(104)_{Hex.}$ doubling superlattice reflections relative to the other superlattice reflections may be observed. On the other hand, ordering in the octahedral sites do change the periodicity of the $(104)_{Hex.}$ planes, as shown in Figure 31b. In this case, the doubling superlattice reflections of the $(104)_{Hex.}$ plane are expected. The same trend in the intensity of the $(104)_{Hex.}$ doubling superlattice reflection is observed in the simulated X-ray powder diffraction data (Figure 31c). In the simulation, 0.06 Ni per formula unit are located in both the octahedral 3a sites and the tetrahedral 6c sites of the Li layer. As expected, a random distribution of Ni and Li ions on the tetrahedral and octahedral sites results in zero intensity of the superlattice peaks. For the octahedral ordering in both the $2\boldsymbol{a}_{Hex.} \times 2\boldsymbol{a}_{Hex.} \times \boldsymbol{c}_{Hex.}$ supercell ($R\bar{3}m$) and the $\boldsymbol{a}_{Mon.} \times \boldsymbol{a}_{Mon.} \times \boldsymbol{c}_{Mon.}$ supercell (P2/m), strong $(104)_{Hex.}$ superlattice intensities relative to the other superlattice peaks are observed. In contrast, although the ordering of the tetrahedral sites results in the appearance of many other superlattice peaks similar to that of the octahedral site ordering, the $(104)_{Hex.}$ superlattice reflection is forbidden. Therefore, the presence and the intensity of the $(104)_{Hex.}$ doubling superlattice reflection in the experimental electron diffraction patterns may be used to distinguish the various cation ordering models.

Similar doubling superlattice reflections as the charged samples were found for the discharged samples. However, it is believed that the nature of the cation ordering is different. In the discharged samples, the occupancy of Li ions in the octahedral sites is significantly greater than what was observed in the charged samples (Figure 26a). Also, the occupancy of the Ni ions in the octahedral sites is considerably larger. In the following sections, the experimental electron diffraction results are combined with the simulated electron and X-ray diffraction data of the various superstructure models, and

also considering the electrochemical measurements reported previously[1, 2, 30], to discuss the likely ordering schemes in the charged and discharged samples.

4.3.1 Ordering in the Tetrahedral Sites of the Li Layer in the Charged Samples

The 4.5 V charged $Li_{0.2}Ni_{0.5}Mn_{0.5}O_2$ sample has a higher fraction of its crystals exhibiting the doubling superlattice reflections characteristic to the $\boldsymbol{a}_{Mon.} \times \boldsymbol{a}_{Mon.} \times \boldsymbol{c}_{Mon.}$ and the $2\boldsymbol{a}_{Hex.} \times 2\boldsymbol{a}_{Hex.} \times \boldsymbol{c}_{Hex.}$ supercells. In this sample, 0.03 Ni per formula unit is found in the tetrahedral sites (Figure 26a), which is in good agreement with literature results that show 0.02 Ni per formula unit in a $Li_{0.33}Ni_{0.5}Mn_{0.5}O_2$ electrode charged to 4.3 V[30]. In addition to the tetrahedral Ni occupancy, recent neutron diffraction studies reveal a considerable amount of Li ions (0.12 per formula unit) in the tetrahedral sites in the 4.6 V charged $Li_{0.33}Ni_{0.5}Mn_{0.5}O_2$ sample[1]. In the 4.5 V charged sample of this study, it is believed that a considerable amount of Li ions may similarly exist in the tetrahedral sites of the Li layer. The remaining Li ions and 0.03 Ni per formula unit are located on the octahedral sites of the Li layer (Figure 26a). In addition, no superlattice peaks were found in the synchrotron X-ray diffraction data[2].

Since the doubling superlattice reflections of the $(104)_{Hex.}$ fundamental reflections were either absent (Figure 18b) or very weak (Figure 18a) relative to the other superlattice reflections in the experimental patterns, it is proposed that these superlattice reflections could be attributed primarily to the ordering of Li, Ni, and vacancies in the tetrahedral sites of the Li layer. Corresponding to the experimental patterns in Figure 18a, simulated patterns based on the tetrahedral site ordering in both the $\boldsymbol{a}_{Mon.} \times \boldsymbol{a}_{Mon.} \times \boldsymbol{c}_{Mon.}$ and $2\boldsymbol{a}_{Hex.} \times 2\boldsymbol{a}_{Hex.} \times \boldsymbol{c}_{Hex.}$ supercells along the equivalent zone axes of the $[45\bar{1}]_{Hex.}$

is shown in Figures 32a-b. In the simulated patterns, the doubling superlattice reflections of the $(104)_{Hex.}$ parent planes are absent for ideal oxygen and cation positions. In contrast, simulated electron diffraction patterns based on the octahedral ordering in both the $\boldsymbol{a}_{Mon.} \times \boldsymbol{a}_{Mon.} \times \boldsymbol{c}_{Mon.}$ and $2\boldsymbol{a}_{Hex.} \times 2\boldsymbol{a}_{Hex.} \times \boldsymbol{c}_{Hex.}$ supercells are shown in Figures 32c-d. The appearance of the doubling superlattice reflections of the $(104)_{Hex.}$ type are observed. Furthermore, the relative intensity of the $(104)_{Hex.}$ doubling superlattice reflections is strong, inconsistent with the experimental electron diffraction observations. Therefore, it is believed that the Li and Ni ions are ordered in the tetrahedral sites of the Li layer in the 4.5 V charged sample. As additional Li ions are de-intercalated from the structure by charging the electrode further from 4.5 V to 5.3 V, more Ni ions can migrate into the transition metal layer. When the Li and Ni tetrahedral occupancies are reduced, tetrahedral site ordering may also diminish. In the 5.3 V charged sample, very few crystals showed the doubling superlattice reflections (Figure 29). Moreover, one of the $[241]_{Hex.}$ zone axis patterns collected from the 5.3 V charged sample in Figure 20b clearly shows the doubling reflections (marked by white stars) of the $(10\bar{2})_{Hex.}$ and $(110)_{Hex.}$ parent reflections, but those of the $(104)_{Hex.}$ parent plane are not observable. The appearance of the $(110)_{Hex.}$ superlattice reflections in this zone axis can be indexed consistently to the $2\boldsymbol{a}_{Hex.} \times 2\boldsymbol{a}_{Hex.} \times \boldsymbol{c}_{Hex.}$ supercell ($R\bar{3}m$), but not to the $\boldsymbol{a}_{Mon.} \times \boldsymbol{a}_{Mon.} \times \boldsymbol{c}_{Mon.}$ supercell (P2/m). Therefore, it is proposed that the doubling superlattice reflections observed in the charged samples are attributed to the ordering of Li, Ni, and vacancies on the tetrahedral sites in the $2\boldsymbol{a}_{Hex.} \times 2\boldsymbol{a}_{Hex.} \times \boldsymbol{c}_{Hex.}$ supercell ($R\bar{3}m$) (Figure 30b). In this proposed superstructure, no adjacent upper and lower tetrahedral sites are occupied,

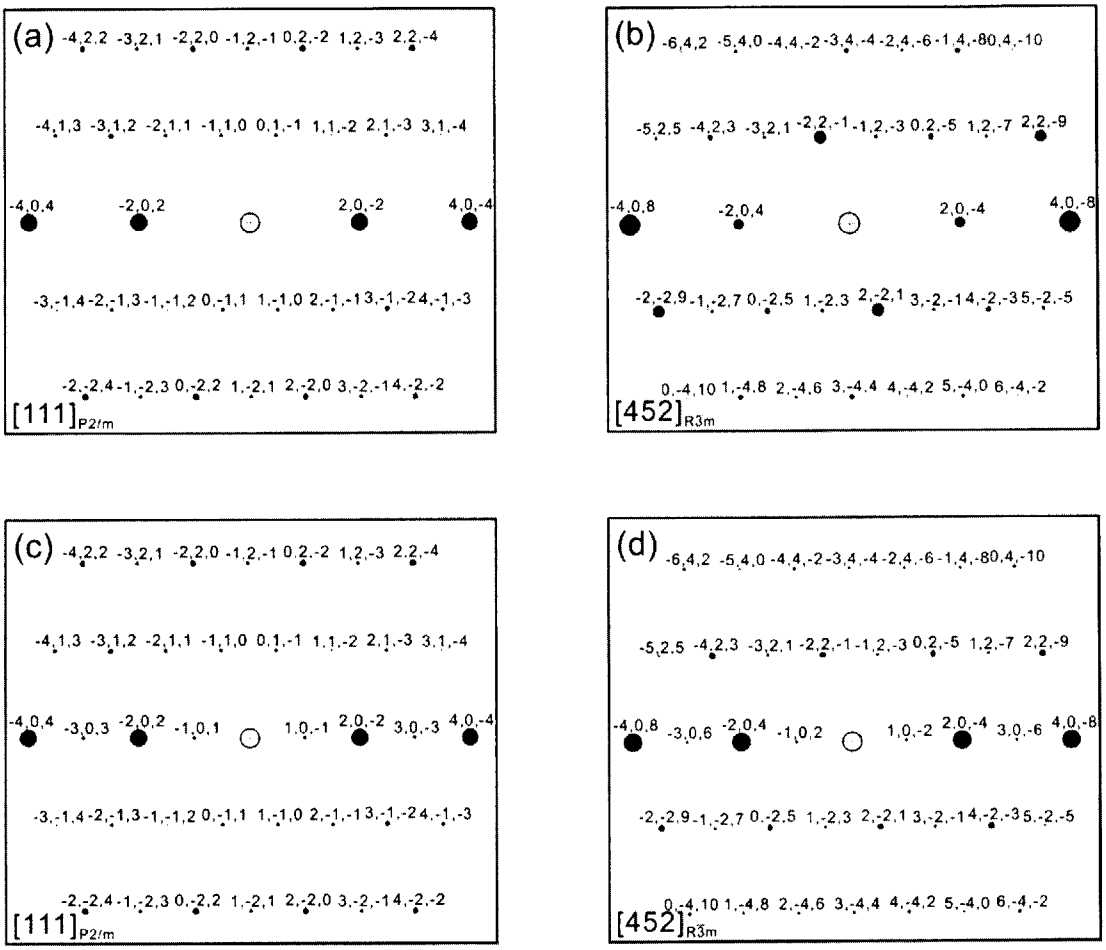

Figure 32: Simulated electron diffraction patterns of the experimental pattern in Figure 18a based on tetrahedral site ordering under the (a) P2/m and (b) R $\bar{3}m$ symmetry, and octahedral site ordering under the (c) P2/m and (d) R $\bar{3}m$ symmetry.

which minimizes the electrostatic repulsion amongst the cations in tetrahedral sites. In addition, the Li and Ni ions on the octahedral sites are randomly distributed in the Li layer. This superstructure can exist over a range of Li compositions based on a partial occupancy of Ni and Li ions in the upper and lower tetrahedral sites.

4.3.2 Ordering in the Octahedral Sites of the Li Layer in the Discharged Samples

The discharged samples have a large number of Li ions (~0.8 - 0.9 per formula unit) on the octahedral sites of the Li layer, and some Ni ions (~0.06 per formula unit) in the octahedral sites of the Li layer (Figure 26a). In addition, small amounts of Ni and Li ions may exist in the tetrahedral sites of the Li layer (0.02 Ni formula unit in the 4.5 V charged sample)[1, 2]. The tetrahedral and octahedral ordering of Li, Ni, and vacancies may coexist in the layered structure, and be responsible for the appearance of the doubling superlattice reflections in the discharged samples. Since the Li and Ni occupancies in the octahedral sites are much greater than those in the tetrahedral sites, it is hypothesized that octahedral ordering is predominant the discharged samples. The $2\boldsymbol{a}_{\text{Hex.}} \times 2\boldsymbol{a}_{\text{Hex.}} \times \boldsymbol{c}_{\text{Hex.}}$ structural model of octahedral ordering can be excluded as the doubling superlattice reflections of the $(104)_{\text{Hex.}}$ planes are absent in the experimental electron diffraction patterns collected from the discharged samples. Quite a few patterns show unique evidence for the cation ordering in the $\boldsymbol{a}_{\text{Mon.}} \times \boldsymbol{a}_{\text{Mon.}} \times \boldsymbol{c}_{\text{Mon.}}$ cell with space group P2/m. For example, one of the $[\bar{2}4\bar{1}]_{\text{Hex.}}$ zone axis patterns collected from the 4.5 V discharged samples is shown in Figure 33a. In this pattern, the doubling superlattice reflections of the $(10\bar{2})_{\text{Hex.}}$ parent planes are strong, whereas those of the $(110)_{\text{Hex.}}$ and $(104)_{\text{Hex.}}$ parent planes are absent. The absence of the doubling superlattice reflections of

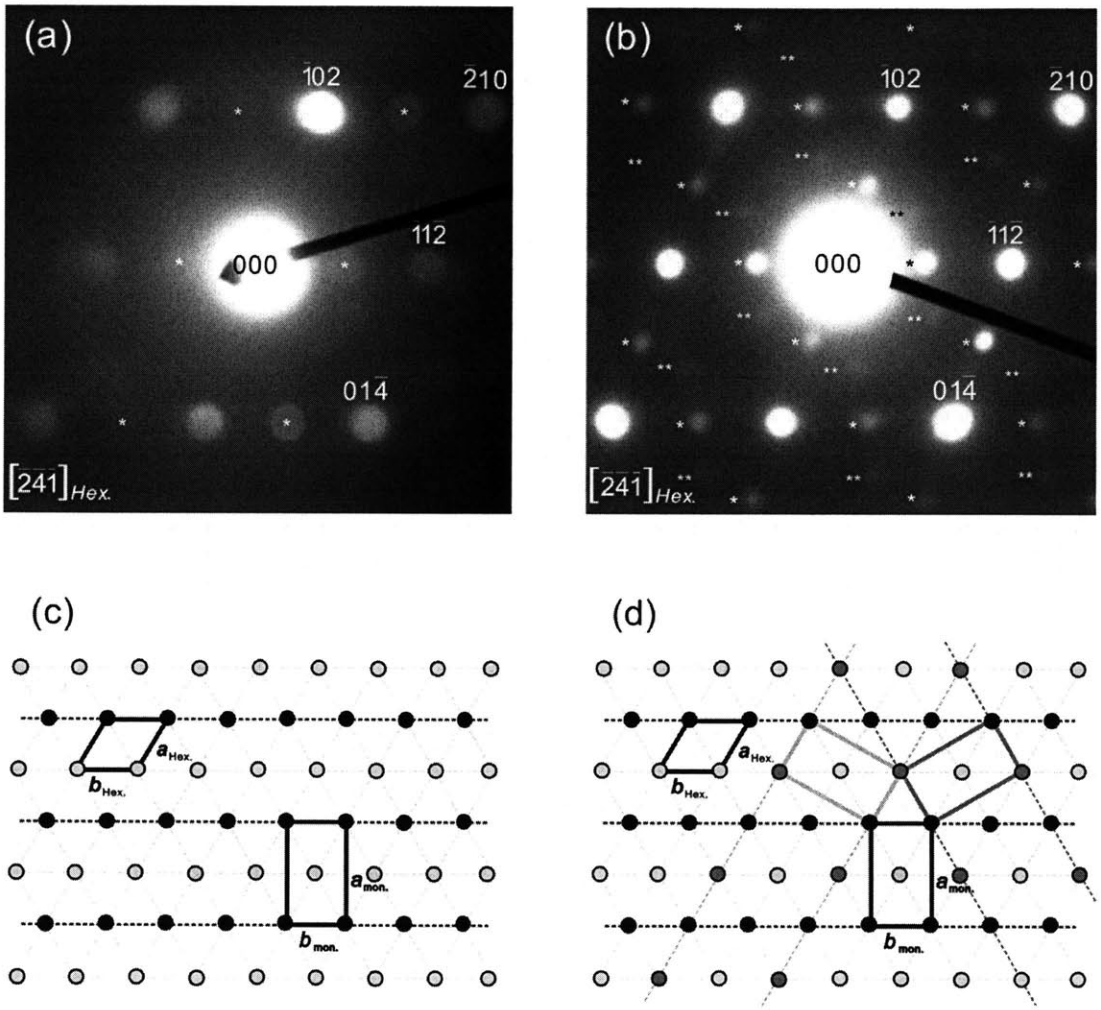

Figure 33: Two electron diffraction patterns (a) and (b) from the 4.5 V discharged sample collected along the $[\,\overline{2}4\overline{1}\,]_{Hex.}$ zone axis, where doubling and tripling superlattice reflections are marked by one and two stars, respectively. Schematic illustrations of P2/m ordering with (c) one variant and (d) possible three variants model.

the $(110)_{Hex.}$ reflections in this zone axis further excludes the $2\boldsymbol{a}_{Hex.} \times 2\boldsymbol{a}_{Hex.} \times \boldsymbol{c}_{Hex.}$ tetrahedral ordering (Figure 34a). The pattern in Figure 33a can be indexed consistently based on the octahedral site ordering in the $\boldsymbol{a}_{Mon.} \times \boldsymbol{a}_{Mon.} \times \boldsymbol{c}_{Mon.}$ cell with space group P2/m (Figures 33c and 34b), in which one row is fully occupied and the other row is partially occupied by Li/Ni. It is important to note that although the $\boldsymbol{a}_{Mon.} \times \boldsymbol{a}_{Mon.} \times \boldsymbol{c}_{Mon.}$ supercell with octahedral site ordering can give rise to strong doubling superlattice reflections of the $(104)_{Hex.}$ parent plane, they are absent in this particular zone axis. Furthermore, multiple orientation states of the ordered domains may coexist in one crystal. For example, another $[\bar{2}4\bar{1}]_{Hex.}$ zone axis pattern collected from the 4.5 V discharged samples is shown in Figure 33b, which can only be explained by considering two orientation states of ordered $\boldsymbol{a}_{Mon.} \times \boldsymbol{a}_{Mon.} \times \boldsymbol{c}_{Mon.}$ domains in this crystal (Figure 33d). As discussed in literature[27, 33, 41, 42], there are three independent orientation states (variants) of ordering in the $\boldsymbol{a}_{Mon.} \times \boldsymbol{a}_{Mon.} \times \boldsymbol{c}_{Mon.}$ cell having space group P2/m with respect to the parent cell with rhombohedral symmetry ($R\bar{3}m$). Ordering in the different orientation states may occur within one $Li_xNi_{0.5}Mn_{0.5}O_2$ crystal during electrochemical cycling, and these variants may exist within one Li layer and/or in different Li layers. Therefore, it is speculated that the doubling superlattice reflections observed in the discharged samples is due to the ordering of Li, Ni, and vacancies on the octahedral sites in alternating rows of the Li layer (Figure 30c).

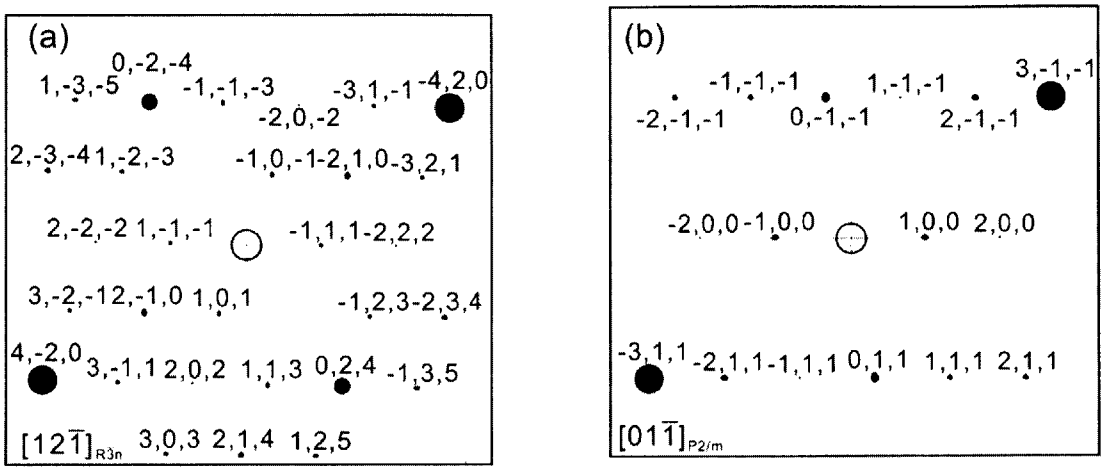

Figure 34: Simulated electron diffraction pattern of the experimental pattern in Figure 33a based on tetrahedral site ordering under the (a) $R\bar{3}m$ and (b) P2/m symmetries.

5.0 GENERAL DISCUSSION AND CONCLUSIONS

Despite the high Ni content in the Li layer, $LiNi_{0.5}Mn_{0.5}O_2$ demonstrates excellent capacity and cycleability properties as an attractive cathode material. It has been shown that both its discharge capacity and rate capability have improved upon cycling to high voltages. The improvements in discharge capacity and rate capability have been attributed to the favorable structural changes imposed by high voltages. Single crystal electron diffraction analyses of pristine and cycled $Li_xNi_{0.5}Mn_{0.5}O_2$ samples have shown that the fraction of crystals exhibiting the $\sqrt{3}\boldsymbol{a}_{Hex.} \times \sqrt{3}\boldsymbol{a}_{Hex.} \times \boldsymbol{c}_{Hex.}$ superlattice reflections has significantly decreased upon charging to 4.5 V and 5.3 V. The disappearance and weakening of the $\sqrt{3}\boldsymbol{a}_{Hex.} \times \sqrt{3}\boldsymbol{a}_{Hex.} \times \boldsymbol{c}_{Hex.}$ superlattice reflections can be explained by Ni migration from the Li to the transition metal layer and an increasing Ni occupancy in the transition metal layer upon charging to high voltages, in good agreement with previous powder diffraction studies[1, 2]. A considerable change in the Ni occupancy of the transition metal layer has been found in the 4.5 V charged $Li_{0.2}Ni_{0.5}Mn_{0.5}O_2$ sample. In addition, some crystals of the $Li_0Ni_{0.5}Mn_{0.5}O_2$ electrodes charged to 5.3 V and of the $Li_{0.8}Ni_{0.5}Mn_{0.5}O_2$ electrode cycled between 4.5 V and 2.0 V for 21 cycles have transformed to the O1 structure. The formation of the O1 structure indicates that nearly all of the Ni ions have migrated from the Li to the transition metal layer, allowing the transition metal layers to shift into the O1 stacking order. In addition, Ni migration has found to be in part reversible upon discharge, as demonstrated by the decreased number of crystals in the discharged samples exhibiting the $\sqrt{3}\boldsymbol{a}_{Hex.} \times \sqrt{3}\boldsymbol{a}_{Hex.} \times \boldsymbol{c}_{Hex.}$ superlattice reflections. However, extended cycling at 4.5 V has similar effects as exposure to 5.3 V. The fraction of Ni ions that permanently remains in the transition metal layer in these

samples with respect to cycling to 4.5 V for 5 cycles only has been dramatically increased. It is believed that the excellent reversibility of $LiNi_{0.5}Mn_{0.5}O_2$, even with a considerable amount of cation disorder, is due to the mobility and the migration of Ni ions in the layered structure upon Li removal and electrochemical cycling, which might facilitate Li diffusion in the Li slab space. These observations are in good agreement with the improved rate capability of the electrodes exposed to 5.3 V[2].

Electron diffraction data have shown additional superlattice reflections in a subset of crystallites from the cycled samples. They are indicative of cation ordering in a $2\boldsymbol{a}_{Hex.} \times 2\boldsymbol{a}_{Hex.} \times \boldsymbol{c}_{Hex.}$ supercell with the space group $R\bar{3}m$ and/or in an $\boldsymbol{a}_{Mon.} \times \boldsymbol{a}_{Mon.} \times \boldsymbol{c}_{Mon.}$ supercell with the space group P2/m. It is proposed that the Li, Ni, and vacancies order in the tetrahedral sites of the Li layer with partial occupancy, and give rise to the appearance of the $2\boldsymbol{a}_{Hex.} \times 2\boldsymbol{a}_{Hex.} \times \boldsymbol{c}_{Hex.}$ supercell and the observed superlattice reflections in the charged samples. This type of ordering is found especially pronounced in the 4.5 V charged sample, which is in good agreement with the synchrotron X-ray diffraction data showing a large amount of Ni (~0.03 per formula unit) in the tetrahedral sites. Such an ordering configuration in the tetrahedral sites may minimize the electrostatic interactions amongst the cations and stabilize the O3 structure. For the discharged samples, it is proposed that the Li, Ni, and vacancies order on the octahedral sites, as described by the $\boldsymbol{a}_{Mon.} \times \boldsymbol{a}_{Mon.} \times \boldsymbol{c}_{Mon.}$ cell with the space group P2/m. It is believed that this type of ordering might facilitate the Li diffusion in the interlayer space (relative to a randomly distributed Li and Ni ions in the Li layer), and contribute to the excellent reversibility of $Li/LiNi_{0.5}Mn_{0.5}O_2$ cells despite the fact that the cycled samples in the discharged state have ~0.06 Ni per formula unit in the Li layer. Partial occupancy of the

Li and Ni ions on the tetrahedral and octahedral sites can allow the proposed superstructures to accommodate and exist over a range of Li compositions.

The proposed superstructures for the charged and discharged $Li_xNi_{0.5}Mn_{0.5}O_2$ samples based on the electron diffraction data are not detected in the synchrotron X-ray powder diffraction data nor in the differential capacity plots of the $Li/Li_xNi_{0.5}Mn_{0.5}O_2$ cells. This is because electron diffraction is more sensitive to the ordering of light atoms and the partial occupancy of heavy atoms than X-rays. Also, single-crystal electron diffraction analysis can better detect ordered minor phases than X-ray powder diffraction and electrochemical data, and provide an averaged information over the entire sample. Lastly, it should be mentioned that based on the electron diffraction evidence presented in this study, other Li and vacancies ordering configurations are not excluded.

REFERENCES

1. Breger, J., et al., *Effect of High Voltage on the Structure and Electrochemistry of $LiNi_{0.5}Mn_{0.5}O_2$: A Joint Experimental and Theoretical Study.* Chemistry of Materials, 2006. 18(20): p. 4768 - 4781.

2. Naoaki Yabuuchi, Sundeep Kumar, Hayley H. Li, Yong-Tae Kim, and Yang Shao-Horn, *Changes in the Crystal Structure and Electrochemical Properties of $Li_xNi_{0.5}Mn_{0.5}O_2$ during Electrochemical Cycling to High Voltages.* Submitted to the Journal of the Electrochemical Society, 2006.

3. Ohzuku, T. and Y. Makimura, *Layered Li Insertion Material of $LiNi_{1/2}Mn_{1/2}O_2$: A Possible Alternative to $LiCoO_2$ for Advanced Li-ion Batteries.* Chemistry Letters, 2001. 30(8): p. 744 - 745.

4. Makimura, Y. and T. Ohzuku, *Li Insertion Material of $LiNi_{1/2}Mn_{1/2}O_2$ for Advanced Li-ion Batteries.* Journal of Power Sources, 2003. 119: p. 156 - 160.

5. Lu, Z.H., D.D. MacNeil, and J.R. Dahn, *Layered Cathode Materials $LiNi_xLi_{1/3-2x/3}Mn_{2/3-x/3)}O_2$ for Li-ion Batteries.* Electrochemical and Solid State Letters, 2001. 4(11): p. A191 - A194.

6. Van der Ven, A. and G. Ceder, *Ordering in $Li_xNi_{0.5}Mn_{0.5}O_2$ and its Relation to Charge Capacity and Electrochemical Behavior in Rechargeable Li Batteries.* Electrochemistry Communications, 2004. 6(10): p. 1045 - 1050.

7. Reed, J. and G. Ceder, *Charge, Potential, and Phase Stability of Layered $LiNi_{0.5}Mn_{0.5}O_2$.* Electrochemical and Solid State Letters, 2002. 5(7): p. A145 - A148.

8. Yoon, W.S., et al., *Investigation of the Local Structure of the $LiNi_{0.5}Mn_{0.5}O_2$ Cathode Material During Electrochemical Cycling by X-ray Absorption and NMR Spectroscopy.* Electrochemical and Solid State Letters, 2002. 5(11): p. A263 - A266.

9. Rossen, E., C.D.W. Jones, and J.R. Dahn, *Structure and Electrochemistry of $Li_xMn_yNi_{1-y}O_2$.* Solid State Ionics, 1992. 57(3-4): p. 311 - 318.

10. Spahr, M.E., et al., *Characterization of Layered Li Ni Mn Oxides Synthesized by a Novel Oxidative Coprecipitation Method and their Electrochemical Performance as Li Insertion Electrode Materials.* Journal of the Electrochemical Society, 1998. 145(4): p. 1113 - 1121.

11. Kim, J.S., C.S. Johnson, and M.M. Thackeray, *Layered $xLiMO_2*(1-x)Li_2M'O_3$ Electrodes for Li Batteries: a Study of $0.95LiMn_{0.5}Ni_{0.5}O_2*0.05Li_2TiO_3$.* Electrochemistry Communications, 2002. 4(3): p. 205 - 209.

12. Johnson, C.S., et al., *The Role of Li_2MO_2 Structures (M = Metal Ion) in the Electrochemistry of $(x)LiMn_{0.5}Ni_{0.5}O_2*(1-x)Li_2TiO_3$ Electrodes for Li-ion Batteries.* Electrochemistry Communications, 2002. 4(6): p. 492 - 498.

13. Johnson, C.S., et al., *Structural Characterization of Layered $Li_xNi_{0.5}Mn_{0.5}O_2$ ($0 < x <= 2$) Oxide Electrodes for Li Batteries.* Chemistry of Materials, 2003. 15(12): p. 2313 - 2322.

14. Kang, K.S., et al., *Electrodes with High Power and High Capacity for Rechargeable Li Batteries.* Science, 2006. 311(5763): p. 977 - 980.

15. Makimura, Y. 2003, Ph.D. Thesis, Osaka City University.

16. Lu, Z.H., Z.H. Chen, and J.R. Dahn, *Lack of Cation Clustering in $LiNi_xLi_{1/3-2x/3}Mn_{2/3-x/3}O_2$ ($0 < x <= 1/2$) and $LiCr_xLi_{(1-x)/3}Mn_{(2-2x)/3}O_2$ ($0 < x < 1$).* Chemistry of Materials, 2003. 15(16): p. 3214 - 3220.

17. Lu, Z.H., et al., *Synthesis, Structure, and Electrochemical Behavior of $LiNi_xLi_{1/3-2x/3}Mn_{2/3-x/3}O_2$.* Journal of the Electrochemical Society, 2002. 149(6): p. A778 - A791.

18. Arachi, Y., et al., *Structural Change of $Li_{1-x}Ni_{0.5}Mn_{0.5}O_2$ Cathode Materials for Li-ion Batteries by Synchrotron Radiation.* Chemistry Letters, 2003. 32(1): p. 60 - 61.

19. Kobayashi, H., et al., *Structural Determination of $Li_{1-y}Ni_{0.5}Mn_{0.5}O_2$ ($y = 0.5$) Using a Combination of Rietveld Analysis and the Maximum Entropy Method.* Journal of Materials Chemistry, 2004. 14(1): p. 40 - 42.

20. Shannon, R.D., *Revised Effective Ionic-Radii and Systematic Studies of Interatomic Distances in Halides and Chalcogenides.* Acta Crystallographica Section A, 1976. 32(SEP1): p. 751 - 767.

21. Wu, E.J., P.D. Tepesch, and G. Ceder, *Size and Charge Effects on the Structural Stability of $LiMO_2$ (M = Transition Metal) Compounds.* Philosophical Magazine B-Physics of Condensed Matter Statistical Mechanics Electronic Optical and Magnetic Properties, 1998. 77(4): p. 1039 - 1047.

22. Peres, J.P., et al., *The Relationship Between the Composition of Li Ni Oxide and the Loss of Reversibility During the First Cycle.* Journal of Physics and Chemistry of Solids, 1996. 57(6-8): p. 1057 - 1060.

23. Meng, Y.S., et al., *Cation Ordering in Layered O3 $LiNi_xLi_{1/3-2x/3}Mn_{2/3-x/3}O_2$ ($0 <= x <= 1/2$) Compounds.* Chemistry of Materials, 2005. 17(9): p. 2386 - 2394.

24. Meng, Y.S., et al., *Understanding the Crystal Structure of Layered $LiNi_{0.5}Mn_{0.5}O_2$ by Electron Diffraction and Powder Diffraction Simulation.* Electrochemical and Solid State Letters, 2004. 7(6): p. A155 - A158.

25. Strobel, P. and B. Lambertandron, *Crystallographic and Magnetic-Structure of Li_2MnO_3.* Journal of Solid State Chemistry, 1988. 75(1): p. 90 - 98.

26. Van der Ven, A., et al., *First-Principles Investigation of Phase Stability in Li_xCoO_2.* Physical Review B, 1998. 58(6): p. 2975 - 2987.

27. Shao-Horn, Y., et al., *Probing Li and Vacancy Ordering in O3 Layered Li_xCoO_2 ($x \sim 0.5$) - An Electron Diffraction Study.* Journal of the Electrochemical Society, 2003. 150(3): p. A366 - A373.

28. Delmas, C., et al., *Li Batteries: A New Tool in Solid State Chemistry.* International Journal of Inorganic Materials, 1999. 1(1): p. 11 - 19.

29. Grey, C.P., et al., *Electrochemical Activity of Li in the Transition-Metal Sites of O3 $Li[Li_{(1-2x)/3}Mn_{(2-x)/3}Ni_x]O_2$.* Electrochemical and Solid State Letters, 2004. 7(9): p. A290 - A293.

30. Arachi, Y., et al., *Li De-intercalation Mechanism in $LiNi_{0.5}Mn_{0.5}O_2$ Cathode Material for Li-ion Batteries.* Solid State Ionics, 2005. 176(9-10): p. 895 - 903.

31. Seel, J.A. and J.R. Dahn, *Electrochemical Intercalation of PF_6 into Graphite.* Journal of the Electrochemical Society, 2000. 147(3): p. 892 - 898.

32. Yoon, W.S., et al., *In Situ X-ray Absorption Spectroscopic Study on $LiNi_{0.5}Mn_{0.5}O_2$ Cathode Material During Electrochemical Cycling.* Chemistry of Materials, 2003. 15(16): p. 3161 - 3169.

33. Peres, J.P., F. Weill, and C. Delmas, *Li/Vacancy Ordering in the Monoclinic Li_xNiO_2 ($0.50 <= x <= 0.75$) Solid Solution.* Solid State Ionics, 1999. 116(1-2): p. 19 - 27.

34. Amatucci, G.G., J.M. Tarascon, and L.C. Klein, *CoO_2, the End Member of the Li_xCoO_2 Solid Solution.* Journal of the Electrochemical Society, 1996. 143(3): p. 1114 - 1123.

35. Croguennec, L., C. Pouillerie, and C. Delmas, *Structural Characterisation of New Metastable NiO_2 Phases.* Solid State Ionics, 2000. 135(1-4): p. 259 - 266.

36. Croguennec, L., et al., *Structural Characterization of the Highly De-intercalated $Li_xNi_{1.02}O_2$ Phases (with x <= 0.30).* Journal of Materials Chemistry, 2001. 11(1): p. 131 - 141.

37. Schougaard, S.B., et al., *$LiNi_{0.5+\delta}Mn_{0.5-\delta}O_2$ - A High-rate, High-capacity Cathode for Li Rechargeable Batteries.* Advanced Materials, 2006. 18(7): p. 905 - 909.

38. Ohzuku, T., A. Ueda, and M. Nagayama, *Electrochemistry and Structural Chemistry of $LiNiO_2$ ($R\bar{3}\mathbf{m}$) for 4 Volt Secondary Li Cells.* Journal of the Electrochemical Society, 1993. 140(7): p. 1862 - 1870.

39. Arai, H., et al., *Characterization and Cathode Performance of $Li_{1-X}Ni_{1+X}O_2$ Prepared with the Excess Li Method.* Solid State Ionics, 1995. 80(3 - 4): p. 261 - 269.

40. Rougier, A., P. Gravereau, and C. Delmas, *Optimization of the Composition of the $Li_{1-z}Ni_{1+z}O_2$ Electrode Materials: Structural, Magnetic, and Electrochemical Studies.* Journal of the Electrochemical Society, 1996. 143(4): p. 1168 - 1175.

41. Aizu, K., *Possible Species of Ferromagnetic, Ferroelectric, and Ferroelastic Crystals.* Physical Review B, 1970. 2(3): p. 754.

42. Chiang, Y.M., H.F. Wang, and Y.I. Jang, *Electrochemically Induced Cation Disorder and Phase Transformations in Li Intercalation Oxides.* Chemistry of Materials, 2001. 13(1): p. 53 - 63.

43. Shao-Horn, Y., et al., *Li and Vacancy Ordering in T#2-Li_xCoO_2 Derived from O2-type $LiCoO_2$.* Chemistry of Materials, 2003. 15(15): p. 2977 - 2983.

APPENDIX A: SUMMARY OF ELECTRON DIFFRACTION FINDINGS

Pristine Sample

Film Number	Crystal Number	Zone Axis	Super Cell Size			Doubling Planes		Tripling Planes		Forbidden Planes
						Doubled	Not Doubled	Tripled	Not Tripled	
5564	1	-7 4 1	sqrt(3)	sqrt(3)	1	none	0 -1 4	-1 -1 -3, 1 -2 15	none	none
5568	1	-1 -8 1	sqrt(3)	sqrt(3)	1	none	2 -1 -6, 0 1 8	2 -1 -6, 1 1 9, -1 2 15	none	none
40396	2	0 0 -1	sqrt(3)	sqrt(3)	1	none	-2 1 0, -1 2 0, 1 1 0	-2 1 0, -1 2 0, 1 1 0	none	none
40411	3	1 2 -1	sqrt(3)	sqrt(3)	1	none	2 -1 0, 0 -1 -2	2 -1 0	none	none
56510	7	2 4 1	sqrt(3)	sqrt(3)	1	none	1 -1 2, 2 -1 0, 1 0 -2, 0 1 -4	2 -1 0	none	none
5562	4	1 2 -1	sqrt(3)	sqrt(3)	1	none	2 -1 0	1 1 3, 2 -1 0, 1 -2 -3	none	none
56279	8	4 8 -1	sqrt(3)	sqrt(3)	1	none	1 -1 -4, 0 -1 -8, -1 0 -4, -2 1 0	-2 1 0	none	none
56490	9	-2 2 -1	sqrt(3)	sqrt(3)	1	none	-1 0 2, -1 1 4, 0 1 2, 1 1 0	1 1 0, -2 1 6, -1 2 6	none	none
56500	10	2 7 1	sqrt(3)	sqrt(3)	1	none	-1 0 2	-2 1 -3	none	none
56503	11	5 10 1	sqrt(3)	sqrt(3)	1	none	0 -1 10, 2 -1 0	2 -1 0	none	none
56512	12	1 -7 2	sqrt(3)	sqrt(3)	1	none	-1 1 4	1 1 3	none	none
54733	13	-2 -1 0	sqrt(3)	sqrt(3)	1	none	1 -2 0, 1 -2 6	1 -2 0, 1 -2 3, 1 -2 6	0 0 3	0 0 1, 0 0 2
56494	14	-1 -2 0	sqrt(3)	sqrt(3)	1	none	2 -1 0	2 -1 0, 2 -1 3, -2 1 3	0 0 3	0 0 1, 0 0 2
5572	1	2 4 1	sqrt(3)	sqrt(3)	1	none	-2 1 0, -1 -1 6, 1 -2 6	1 -2 6	-2 1 0, -1 -1 6	-2 2 0, -1 1 0, -2 0 4, -1 0 2
54721	15	1 -1 0	2 sqrt(3)	2 sqrt(3)	1	1 1 0	none	1 1 0, 1 1 3, -1 -1 3	none	1 0 0, 5 0 0, 0 0 1, 0 0 2
5558	5	4 -1 -1	2 sqrt(3)	2 sqrt(3)	1	1 0 4, 1 -2 6	none	1 1 3, 2 -1 9, 1 -2 6	none	0 -1 1, 0 -5 5
5574	6	2 -2 -1	2 sqrt(3)	2 sqrt(3)	1	-2 1 -6, -1 2 -6, 1 1 0	none	-2 1 -6, -1 2 -6, 1 1 0	none	-3 1 -1, -4 2 -2, -2 1 -1, -3 2 -2, -5 5 -5, -1 1 -1, 0 1 -1, 0 5 -5, 1 0 0, 5 0 0
56499	16	2 1 1	2 sqrt(3)	2 sqrt(3)	1	-2 2 2, -1 0 2	-3 2 4, 1 -2 0	1 -2 0	none	0 -1 0, 0 -3 0, 0 -5 0, -4 5 2
56506	18	-7 1 -2	2 sqrt(3)	2 sqrt(3)	1	-2 0 7, 0 2 1	-1 1 4	-1 -1 3	none	-1 2 2
56518	19	5 7 -2	2 sqrt(3)	2 sqrt(3)	1	1 1 6	3 1 -4	-3 1 -4	1 1 6	1 0 1, 2 0 2, 4 0 4, 5 0 5, -5 4 -2
56290	17	-2 -7 -1	2 sqrt(3)	2 sqrt(3)	1	-1 0 2	none	-2 1 -3	none	none
56295	20	1 -1 1	Sqrt(3)*sqrt(3)*1 superlattice reflections disappeared.							

Charged Sample to 4.5V for 2.5 Cycles

Film Number	Crystal Number	Zone Axis	Super Cell Size			Doubling Planes		Tripling Planes		Forbidden Planes
						Doubled	Not Doubled	Tripled	Not Tripled	
53084	1	8 -8 1	sqrt(3)	sqrt(3)	1	none	n/a	-1 -1 0	none	none
53086	2	-1 -2 1	sqrt(3)	sqrt(3)	1	none	n/a	-2 1 0	none	none
53089	3	4 5 -1	sqrt(3)	sqrt(3)	1	none	n/a	-2 1 -3, -1 2 6, 1 1 9	none	none
53076	14	-1 -2 1	sqrt(3)	sqrt(3)	1	none	n/a	-2 1 0, -1 -1 -3	none	none
8672	19	7 11 -1	sqrt(3)	sqrt(3)	1	none	n/a	2 -1 3	none	none
8675	20	-2 -1 -1	sqrt(3)	sqrt(3)	1	none	n/a	-1 2 0	none	none
8684	23	-5 -4 -1	sqrt(3)	sqrt(3)	1	none	n/a	-1 2 -3	none	none
8686	24	-2 -1 -1	sqrt(3)	sqrt(3)	1	none	n/a	-2 1 3	none	none
8688	25	-2 -1 -1	sqrt(3)	sqrt(3)	1	none	n/a	-1 2 0	none	none
8690	26	0 0 -1	sqrt(3)	sqrt(3)	1	none	n/a	2 -1 0, 1 -2 0, -1 -1	none	none
53078	5	4 8 -1	2 sqrt(3)	2 sqrt(3)	1	0 1 8, 2 -1 0	1 0 4, 1 -1 -4	2 -1 0	none	2 -1 2, 1 -1 0, 5 -5 0, -1 2 2
53087	6	4 5 -1	2 sqrt(3)	2 sqrt(3)	1	-1 2 6	1 0 4	2 -1 3, -1 2 6, 1 1 9	none	0 5 5, 0 1 1, 2 -1 2
8680	21	-5 -4 -1	2 sqrt(3)	2 sqrt(3)	1	-2 3 -2	0 1 -4	-1 2 -3	none	
8682	22	2 10 1	2 sqrt(3)	2 sqrt(3)	1	-2 1 -6, -1 0 2, 0 -1	-1 1 -8	-2 1 -6	none	
8692	27	-2 -1 -1	2 sqrt(3)	2 sqrt(3)	1	-1 2 0, 1 0 -2	none	-1 2 0	none	
53082	7	4 5 -1	2	2	1	1 0 4, -1 2 6, -3 2 -2	none	none	n/a	none
53073	8	-1 1 1	2	2	1	1 -1 2, 1 1 0	none	none	n/a	none
53080	9	8 1 -2	2	2	1	1 -4 2	1 0 4	none	n/a	1 0 2
53088	10	-2 -4 -1	2	2	1	-1 0 2, 1 -1 2	0 -1 4, -2 1 0	none	n/a	0 -1 2, -2 1 0
53075	11	-2 -4 -1	2	2	1	-1 0 2, -1 1 -2, 1 1 -6	0 1 -4	none	n/a	0 1 -2
53071	12	4 5 -1	2	2	1	-1 0 -4	none	none	n/a	none
53074	13	-4 -8 1	sqrt(3)*sqrt(3)*1 superlattice reflections disappeared.							
53077	15	4 11 -1	sqrt(3)*sqrt(3)*1 superlattice reflections disappeared.							
53081	16	-1 -2 1	sqrt(3)*sqrt(3)*1 superlattice reflections disappeared.							
53083	17	-1 -5 1	sqrt(3)*sqrt(3)*1 superlattice reflections disappeared.							
53085	18	1 2 -1	sqrt(3)*sqrt(3)*1 superlattice reflections disappeared.							

Charged Sample to 5.3V for 2.5 Cycles

Film Number	Crystal Number	Zone Axis	Super Cell Size			Doubling Planes		Tripling Planes		Forbidden Planes
						Doubled	Not Doubled	Tripled	Not Tripled	
8521	14	1 2 -1	sqrt(3)	sqrt(3)	1	none	n/a	-1 2 3, 1 1 3	-2 1 0	-2 2 0, -1 1 0
8555	25	2 1 1	sqrt(3)	sqrt(3)	1	none	n/a	-1 -1 3	none	none
8526	15	-8 -4 -1	sqrt(3)	sqrt(3)	1	none	n/a	-1 2 0	none	none
8533	16	-2 -1 -1	sqrt(3)	sqrt(3)	1	none	n/a	1 1 -3	none	none
6162	2	-1 -2 1	2 sqrt(3)	2 sqrt(3)	1	0 1 2, -2 1 0	none	-2 1 0	none	-1 1 0, 5 5 0
53185	3	-2 -1 -1	2	2	1	-1 0 2, -1 2 0	none	none	n/a	none
53189	3	2 4 1	2	2	1	-2 1 0, -1 0 2, 0 -1 4, 1 -1 2	0 -1 4	none	n/a	none
53196	4	2 4 1	2	2	1	-1 0 2, 0 -1 4, 1 -1 2, 2 -1 0	none	none	n/a	none
53181	1	0 0 1	1P	1P	1P	none	n/a	3 0 0	2 -1 0, 1 1 0, -1 2 0	none
6163	2	0 0 -1	1P	1P	1P	none	n/a	3 0 0	2 -1 0, 1 1 0, 1 -2 0	none
8512	13	0 0 1	1P	1P	1P	none	n/a	0 3 0, 3 0 0, -3 3 0	2 -1 0, 1 1 0, -1 2 0	none
8542	18	0 0 1	1P	1P	1P	none	n/a	0 3 0	2 -1 0, 1 1 0, -1 2 0	none
8549	21	0 0 1	1P	1P	1P	none	n/a	0 3 0	2 -1 0, 1 1 0, -1 2 0	none
8557	27	0 0 1	1P	1P	1P	none	n/a	0 3 0	2 -1 0, 1 1 0, -1 2 0	none
6169	5	-11 -7 -1	sqrt(3)*sqrt(3)*1 superlattice reflections disappeared.							
6158	6	-2 -1 -1	sqrt(3)*sqrt(3)*1 superlattice reflections disappeared.							
6160	7	1 -1 -1	sqrt(3)*sqrt(3)*1 superlattice reflections disappeared.							
6161	8	-11 -7 -1	sqrt(3)*sqrt(3)*1 superlattice reflections disappeared.							
6165	9	4 5 -1	sqrt(3)*sqrt(3)*1 superlattice reflections disappeared.							
6167	10	1 2 -1	sqrt(3)*sqrt(3)*1 superlattice reflections disappeared.							
6168	11	1 2 -1	sqrt(3)*sqrt(3)*1 superlattice reflections disappeared.							
53194	4	1 1 0	sqrt(3)*sqrt(3)*1 superlattice reflections disappeared.							
53192	12	1 2 -1	sqrt(3)*sqrt(3)*1 superlattice reflections disappeared.							
8539	17	-10 -5 -2	sqrt(3)*sqrt(3)*1 superlattice reflections disappeared.							
8545	19	-1 -2 1	sqrt(3)*sqrt(3)*1 superlattice reflections disappeared.							
8551	22	-2 -10 -1	sqrt(3)*sqrt(3)*1 superlattice reflections disappeared.							
8553	23	3 2 0	sqrt(3)*sqrt(3)*1 superlattice reflections disappeared.							
8554	24	-2 -1 -1	sqrt(3)*sqrt(3)*1 superlattice reflections disappeared.							
8556	26	-2 2 -1	sqrt(3)*sqrt(3)*1 superlattice reflections disappeared.							

Discharged Sample to 4.5V for 5 Cycles

Film Number	Crystal Number	Zone Axis	Super Cell Size			Doubling Planes		Tripling Planes		Forbidden Planes
						Doubled	Not Doubled	Tripled	Not Tripled	
53632	1	-5 -4 -1	sqrt(3)	sqrt(3)	1	none	n/a	-1 2 -3	none	none
53634	2	7 14 -1	sqrt(3)	sqrt(3)	1	none	n/a	2 -1 0	none	none
53615	3	11 7 1	sqrt(3)	sqrt(3)	1	none	n/a	-1 2 -3	none	none
53618	4	-4 -8 1	sqrt(3)	sqrt(3)	1	none	n/a	2 -1 0	none	none
53619	5	-1 -2 1	sqrt(3)	sqrt(3)	1	none	n/a	-2 1 0	none	none
53627	6	5 7 -2	sqrt(3)	sqrt(3)	1	none	n/a	-1 -1 -6	none	none
53628	6	-2 2 -1	sqrt(3)	sqrt(3)	1	none	n/a	-1 -1 0	none	none
53629	7	-4 -8 1	sqrt(3)	sqrt(3)	1	none	n/a	-2 1 0	none	none
53622	8	-1 1 0	sqrt(3)	sqrt(3)	1	none	n/a	-1 -1 3, -1 -1 0, -1 -1 -3	0 0 3	0 0 2, 0 0 1
53636	9	-1 -2 0	sqrt(3)	sqrt(3)	1	none	n/a	2 -1 -3, 2 -1 0, 2 -1 3	0 0 3	0 0 2, 0 0 1
53626	6	-4 -5 1	sqrt(3)	sqrt(3)	1	none	n/a	-1 2 6, -2 1 -3	none	none
53623	17	1 -1 2	sqrt(3)	sqrt(3)	1	none	n/a		none	none
56941	18	8 4 1	sqrt(3)	sqrt(3)	1	none	n/a	-1 2 0	none	none
56945	20	8 1 -2	sqrt(3)	sqrt(3)	1	none	n/a	-1 2 -3	none	none
56946	21	-2 -1 -1	sqrt(3)	sqrt(3)	1	none	n/a	-2 1 3, -1 -1 3	none	none
56951	23	2 7 1	sqrt(3)	sqrt(3)	1	none	n/a	2 -1 3	none	none
56953	24	-5 -4 -1	sqrt(3)	sqrt(3)	1	none	n/a	-1 -1 9, -2 1 6, -1 2 -3	none	none
53631	10	-2 -4 -1	2 sqrt(3)	2 sqrt(3)	1	-1 0 2, -1 1 -2	-2 1 0, 0 -1 4	-2 1 0	none	-5 5 0, -3 3 0, -1 1 0, -1 -1 2
53625	12	5 7 1	2 sqrt(3)	2 sqrt(3)	1	1 -1 2	none	2 -1 -3	none	none
56931	15	-5 -4 -1	2 sqrt(3)	2 sqrt(3)	1	-2 1 6, 0 -1 4	none	-1 2 -3, -2 1 6	none	
56934	16	-2 -4 -1	2 sqrt(3)	2 sqrt(3)	1	-1 0 2, -1 1 -2	-2 1 0, 0 1 -4	-2 1 0	none	
56955	25	2 1 1	2 sqrt(3)	2 sqrt(3)	1	-1 0 2	1 -2 0	1 -2 0	none	
56937	26	-2 -1 -1	2	2	1	1 0 -2	none	n/a	n/a	
56942	19	-2 -4 -1	2	2	1	-1 1 -2	-1 0 2, -2 1 0, 0 1 -4	n/a	n/a	
53617	13	0 1 0	sqrt(3)*sqrt(3)*1 superlattice reflections disappeared.							
53613	14	4 8 -1	sqrt(3)*sqrt(3)*1 superlattice reflections disappeared.							
56949	22	8 4 1	sqrt(3)*sqrt(3)*1 superlattice reflections disappeared.							

Discharged Sample to 5.3V for 5 Cycles

Film Number	Crystal Number	Zone Axis	Super Cell Size			Doubling Planes		Tripling Planes		Forbidden Planes
						Doubled	Not Doubled	Tripled	Not Tripled	
53348	1	-8 17 -1	sqrt(3)	sqrt(3)	1	none	n/a	1 1 9	none	none
53355	2	-1 -11 1	sqrt(3)	sqrt(3)	1	none	n/a	-2 1 9	none	none
53357	3	4 8 -1	sqrt(3)	sqrt(3)	1	none	n/a	-2 1 0	none	none
53358	4	-1 -11 1	sqrt(3)	sqrt(3)	1	none	n/a	-2 1 9	none	none
53368	5	-5 -1 -1	sqrt(3)	sqrt(3)	1	none	n/a	2 -1 -9	none	none
6653	6	4 5 2	sqrt(3)	sqrt(3)	1	none	n/a	-1 2 -3	none	none
6654	7	5 4 1	sqrt(3)	sqrt(3)	1	none	n/a	-1 2 -3, -2 1 6	none	none
53347	10	5 4 -2	sqrt(3)	sqrt(3)	1	none	n/a	-2 1 -3	none	none
53349	11	-11 -16 -1	sqrt(3)	sqrt(3)	1	none	n/a	-2 1 6	none	none
6651	6	-1 4 1	sqrt(3)	sqrt(3)	1	none	n/a	-1 -1 3	none	none
53353	8	-1 -8 1	2 sqrt(3)	2 sqrt(3)	1	0 1 8, -2 1 6	none	1 1 9, -2 1 6	none	-1 1 1, -5 5 5
6666	9	-5 -4 -1	2 sqrt(3)	2 sqrt(3)	1	0 1 -4	none	-1 2 -3	none	none
53362	12	2 7 1	2	2	1	-1 0 2	none	none	n/a	none
53359	13	2 -8 1	2	2	1	1 1 6, -1 1 10, -1 0 2	0 1 8	none	n/a	0 1 4
6661	14	-4 -2 1	2	2	1	0 1 2, -1 1 -2	-1 2 0, -1 0 -4	none	n/a	-1 1 0, -1 0 -2
6664	14	-4 -2 1	2	2	1	0 1 2, -1 1 -2	-1 2 0, -1 0 -4	none	n/a	-1 1 0, -1 0 -2
53370	15	-16 -11 -2	2	2	1	-1 0 8	none	none	n/a	none
53360	13	7 8 -1	2	2	1	2 -1 6	0 1 8	none	n/a	0 1 4
53365	16	2 -2 1	2	2	1	-1 0 2, 0 -1 -2	-1 1 4, -1 -1 0	none	n/a	-1 1 2, -1 -1 0
53350	17	-5 -10 -1	sqrt(3)*sqrt(3)*1 superlattice reflections disappeared.							
53354	18	-2 -1 -1	sqrt(3)*sqrt(3)*1 superlattice reflections disappeared.							
53361	13	0 0 1	sqrt(3)*sqrt(3)*1 superlattice reflections disappeared.							
53369	19	-16 -11 -2	sqrt(3)*sqrt(3)*1 superlattice reflections disappeared.							
53371	15	4 0 1	sqrt(3)*sqrt(3)*1 superlattice reflections disappeared.							
6657	7	-4 0 -1	sqrt(3)*sqrt(3)*1 superlattice reflections disappeared.							
6663	14	1 1 0	sqrt(3)*sqrt(3)*1 superlattice reflections may or may not have disappeared.							
6669	20	-1 -1 0	sqrt(3)*sqrt(3)*1 superlattice reflections disappeared.							

Discharged Sample to 4.5V for 21 Cycles

Film Number	Crystal Number	Zone Axis	Super Cell Size			Doubling Planes		Tripling Planes		Forbidden Planes
						Doubled	Not Doubled	Tripled	Not Tripled	
5776	1	-1 1 1	sqrt(3)	sqrt(3)	1	none	n/a	1 1 0, -1 2 -3, -2 1 -3	none	none
56783	14	2 2 1	sqrt(3)	sqrt(3)	1	none	n/a	-3 3 0, 0 3 -6, -3 6 -6	none	none
5781	3	1 2 0	2 sqrt(3)	2 sqrt(3)	1	-2 1 6, 0 0 6, 2 -1 6, 2 -1 0	none	-2 1 6, 2 -1 6	0 0 6, 2 -1 0	-1 1 1, -5 5 5, 0 0 1, 0 0 2, 0 0 4, 0 0 5, 1 -1 1, 5 -5 5, 1 -1 0, 2 -2 0, 4 -4 0, 5 -5 0
5794	4	2 -2 1	2 sqrt(3)	2 sqrt(3)	1	0 1 2, -1 0 2	1 1 0, -1 1 4	1 1 0	none	1 0 0, 2 0 0, 3 0 0, 4 0 0, 5 0 0, -1 2 2, -1 0 0, -3 0 0, -5 0 0
5779	5	10 2 -1	2 sqrt(3)	2 sqrt(3)	1	-1 3 -4, 0 1 2, 1 1 12, 1 -1 8	none	1 1 12, 0 6 -6	none	1 0 2, 5 0 10
5788	2	1 -1 0	2	2	1	1 1 0, 1 1 6, 1 1 -6	none	none	n/a	0 0 1, 0 0 2
56427	8	-2 2 -1	2	2	1	-1 2 6, -1 0 2	-1 0 2, -1 1 4, 0 1 2, 1 1 0	none	n/a	-1 0 1, -1 1 2, 0 1 1, 1 1 0
56777	11	-2 -4 -1	2	2	1	1 0 -2, 1 -1 2, 1 -2 6	0 -1 4	none	n/a	0 -1 2
56778	12	2 4 1	2	2	1	1 -1 2	-2 1 0, -1 0 2, 0 -1 4	none	n/a	-2 1 0, -1 0 1, 0 -1 2
56784	15	2 1 1	2	2	1	-1 0 2	none	none	n/a	-1 1 0, -3 2 2
56772	10	0 0 -1	1P	1P	1P	none	n/a	0 -3 0	2 -1 0, 1 -2 0, -1 -1 0	none
5784	6	-5 -1 1	sqrt(3)*sqrt(3)*1 superlattice reflections disappeared.							
5792	7	-1 -2 -2	sqrt(3)*sqrt(3)*1 superlattice reflections disappeared.							
56768	9	8 4 1	sqrt(3)*sqrt(3)*1 superlattice reflections disappeared.							
56781	13	-5 -4 -1	sqrt(3)*sqrt(3)*1 superlattice reflections disappeared.							
56786	16	-5 -4 -1	sqrt(3)*sqrt(3)*1 superlattice reflections disappeared.							
56787	17	-8 -4 -1	sqrt(3)*sqrt(3)*1 superlattice reflections disappeared.							
56790	18	8 4 1	sqrt(3)*sqrt(3)*1 superlattice reflections disappeared.							
56800	19	2 1 1	sqrt(3)*sqrt(3)*1 superlattice reflections disappeared.							
56804	20	-2 -1 -1	sqrt(3)*sqrt(3)*1 superlattice reflections disappeared.							

APPENDIX B: ELECTROCHEMICAL HISTORY OF THE CYCLED SAMPLES FOR ELECTRON AND X-RAY DIFFRACTION

(Electron and X-Ray Diffraction) 4.5 V Charged $Li_{0.2}Ni_{0.5}Mn_{0.5}O_2$ Sample Cycled Between 4.5 V and 2.0 V for 2 Complete Cycles and 1 Additional Charge at C/50:

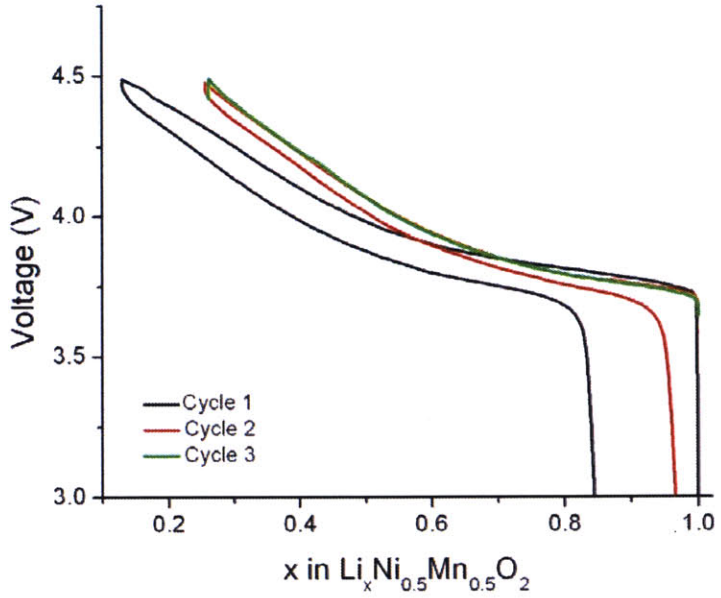

(Electron and X-Ray Diffraction) 5.3 V Charged $Li_0Ni_{0.5}Mn_{0.5}O_2$ Sample Cycled Between 5.3 V and 2.0 V for 2 Complete Cycles and 1 Additional Charge at C/50:

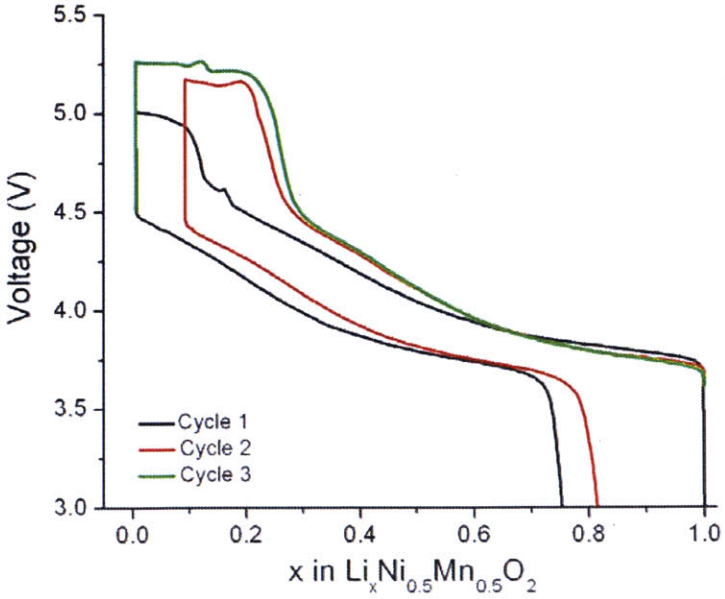

(Electron Diffraction) 4.5 V Discharged $Li_{0.9}Ni_{0.5}Mn_{0.5}O_2$ Sample Cycled Between 4.5 V and 2.0 V for 5 Complete Cycles at C/50:

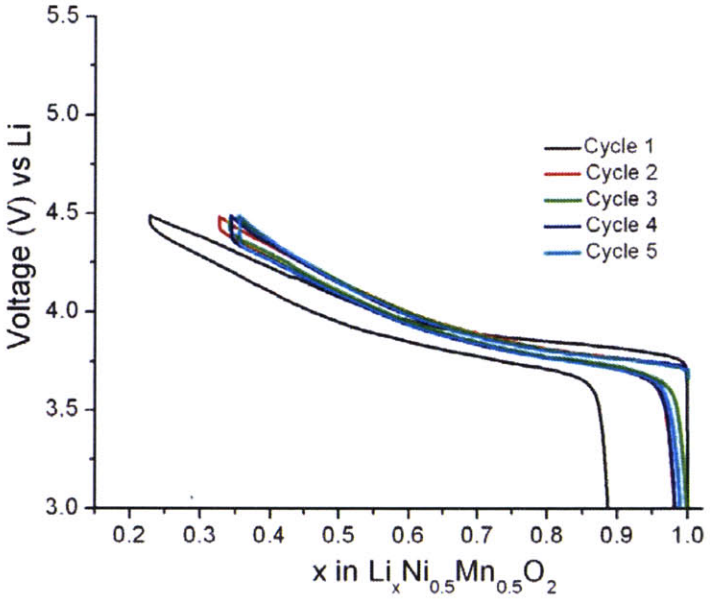

(Electron Diffraction) 5.3 V Discharged $Li_{x>0.76}Ni_{0.5}Mn_{0.5}O_2$ Sample Cycled Between 5.3 V and 2.0 V for 5 Complete Cycles at C/50:

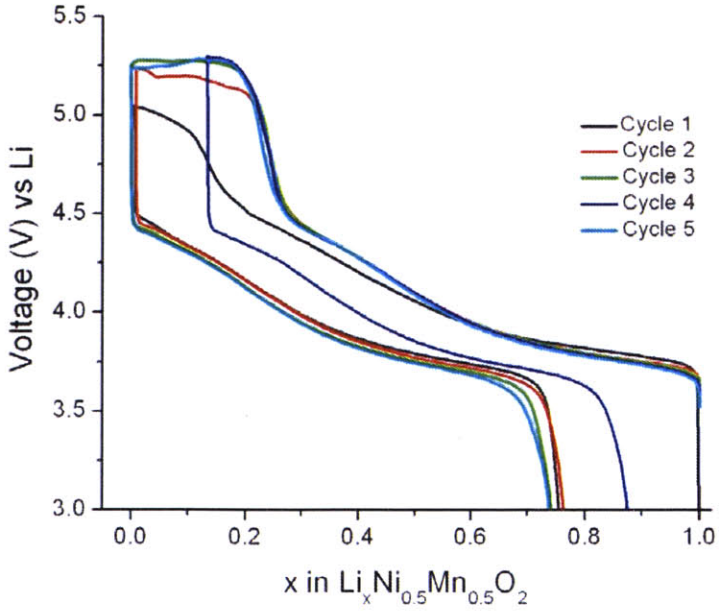

(Electron Diffraction) 4.5 V Extensively Cycled $Li_{0.8}Ni_{0.5}Mn_{0.5}O_2$ Sample in the Discharged State Cycled Between 4.5 V and 2.0 V for 5 Cycles at C/50, 5 Cycles at C/20, 5 Cycles at C/5, 5 Cycles at C/2, and 1 Cycle at C/50:

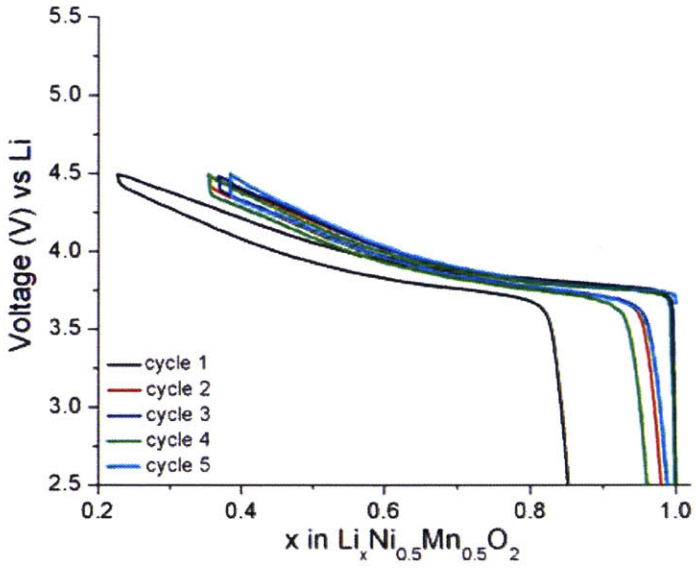

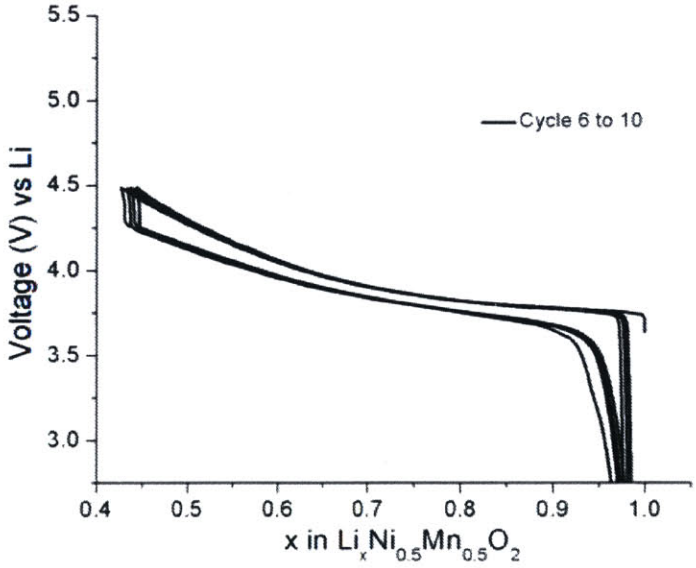

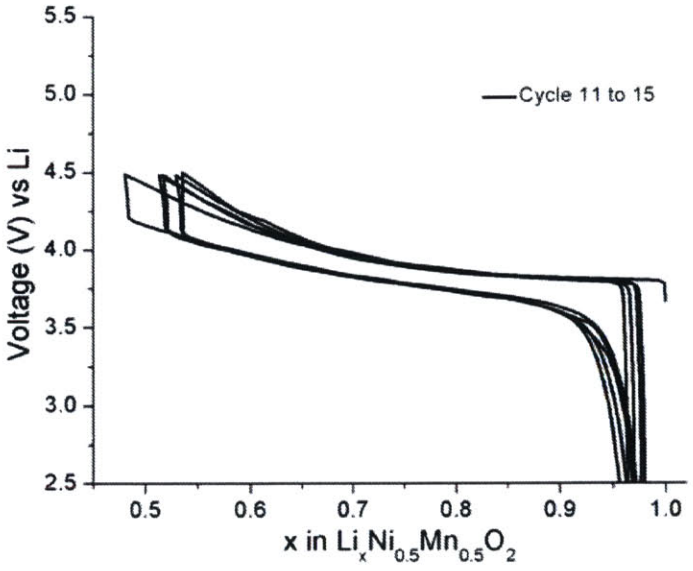
Cycle 11 to 15
Voltage (V) vs Li
x in $Li_xNi_{0.5}Mn_{0.5}O_2$
5.5
5.0
4.5
4.0
3.5
3.0
2.5
0.5
0.6
0.7
0.8
0.9
1.0

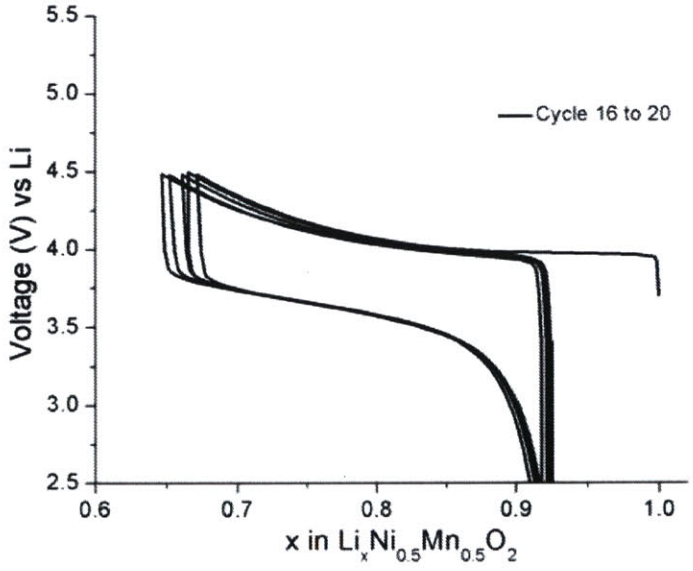
Cycle 16 to 20
Voltage (V) vs Li
x in $Li_xNi_{0.5}Mn_{0.5}O_2$
5.5
5.0
4.5
4.0
3.5
3.0
2.5
0.6
0.7
0.8
0.9
1.0

(X-Ray Diffraction) 4.5 V Discharged $Li_{0.82}Ni_{0.5}Mn_{0.5}O_2$ Sample Cycled Between 4.5 V and 2.0 V for 5 Complete Cycles at C/20 with EIS Steps:

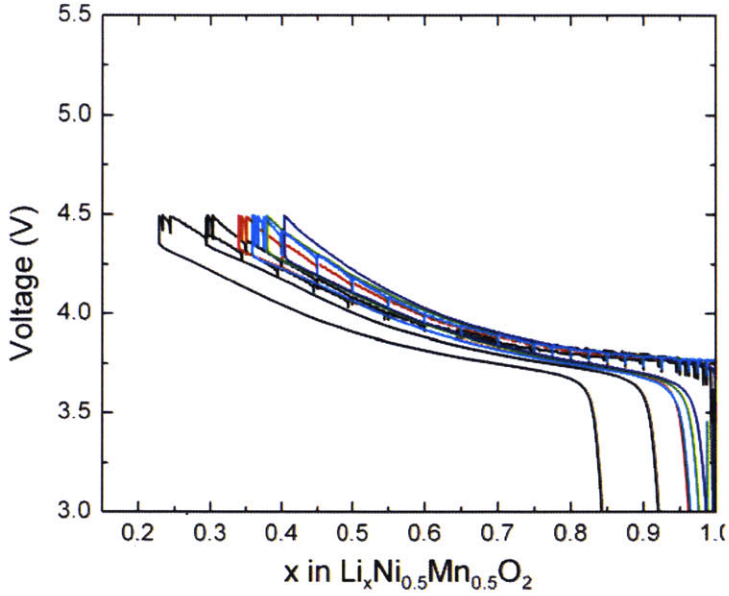

(X-Ray Diffraction) 5.3 V Discharged $Li_{0.75}Ni_{0.5}Mn_{0.5}O_2$ Sample Cycled Between 5.3 V and 2.0 V for 2 Complete Cycles at C/50 with GITT Steps:

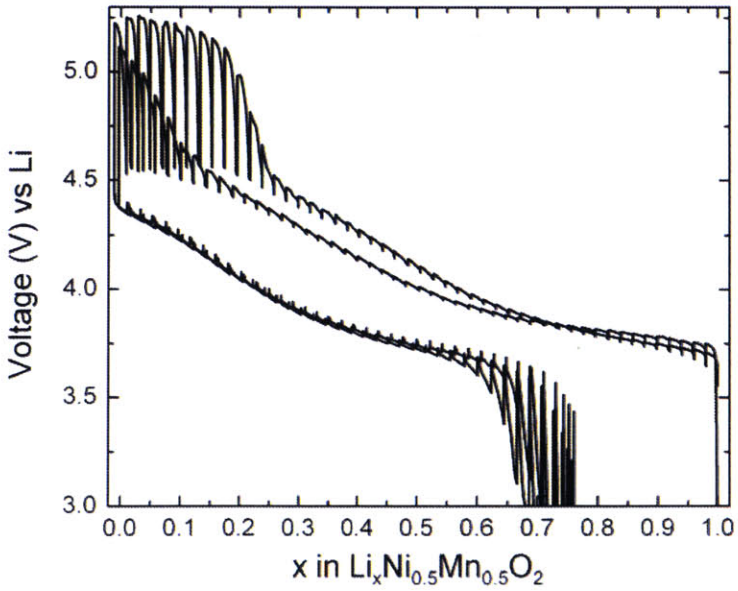

APPENDIX C: BRIGHTFIELD TRANSMISSION ELECTRON MICROSCOPY IMAGES OF THE SAMPLES IN APPENDIX B

Pristine $LiNi_{0.5}Mn_{0.5}O_2$ Sample:

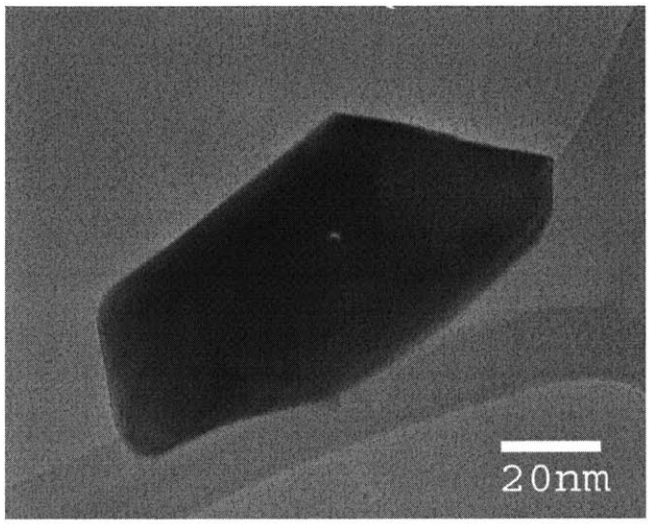

5.3 V Charged $Li_0Ni_{0.5}Mn_{0.5}O_2$ Sample Cycled Between 5.3 V and 2.0 V for 2 Complete Cycles and 1 Additional Charge at C/50:

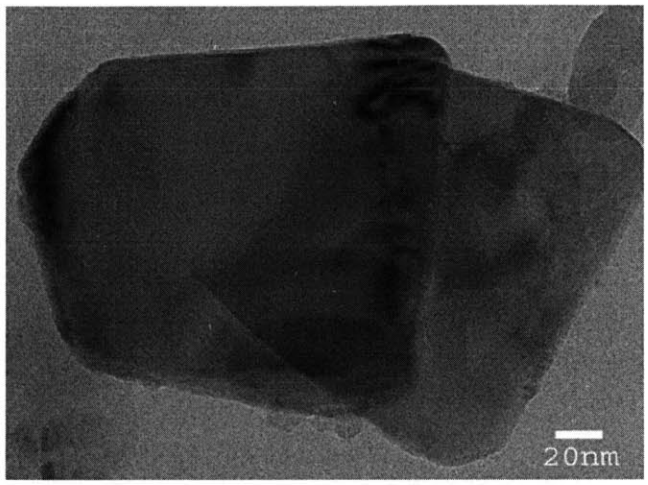

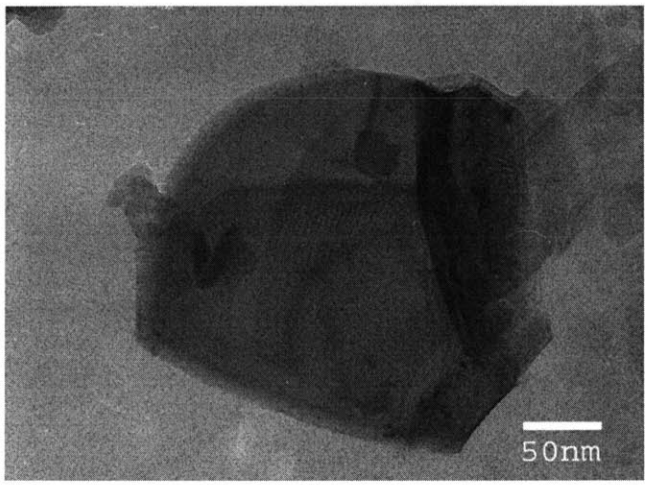

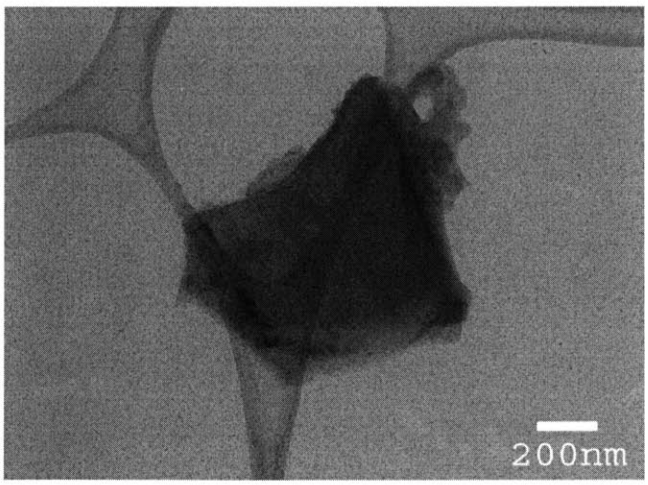

APPENDIX D: ADDITIONAL ELECTRON DIFFRACTION PATTERNS OF THE SAMPLES IN APPENDIX B

Pristine $LiNi_{0.5}Mn_{0.5}O_2$ Sample:

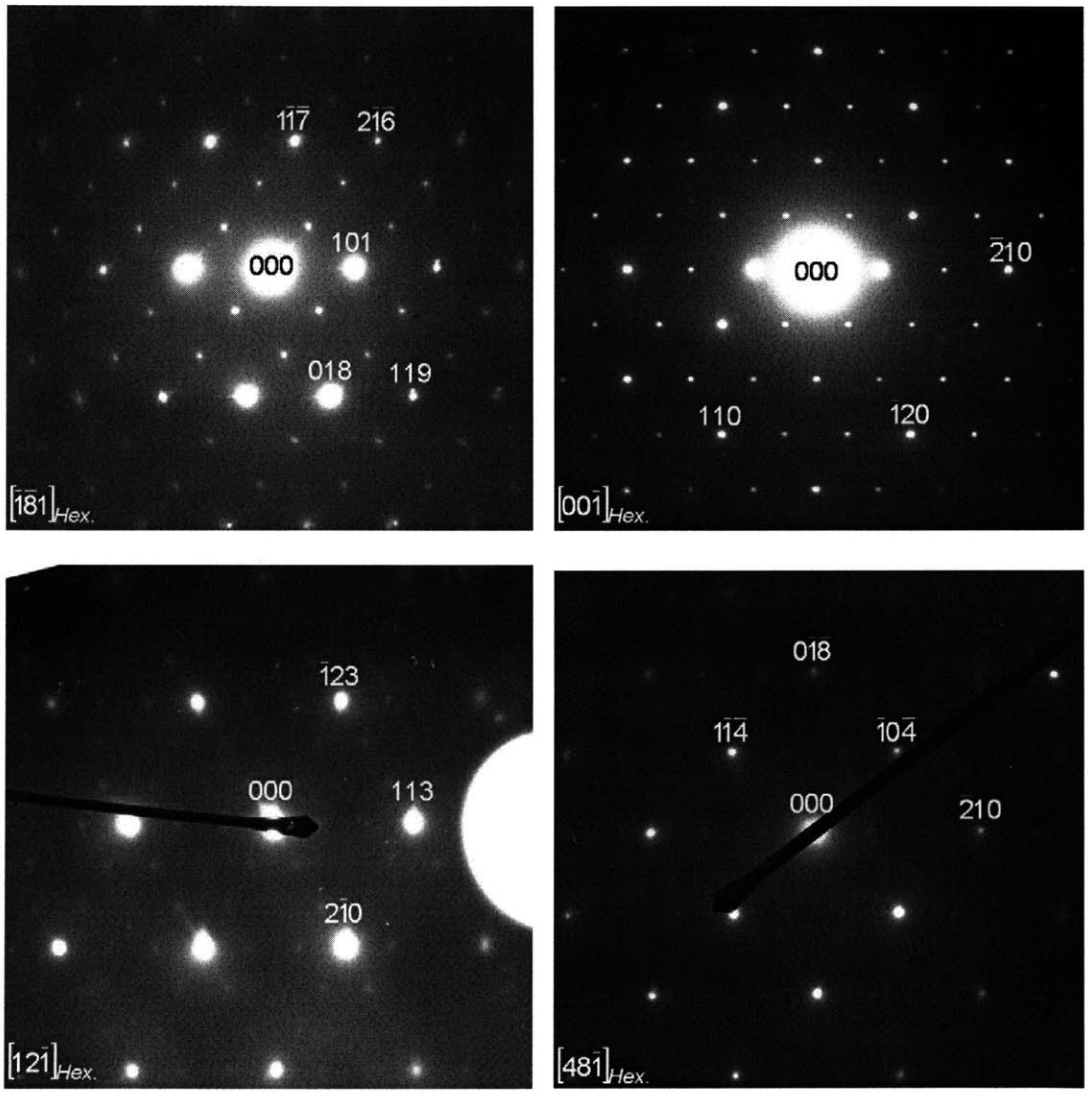

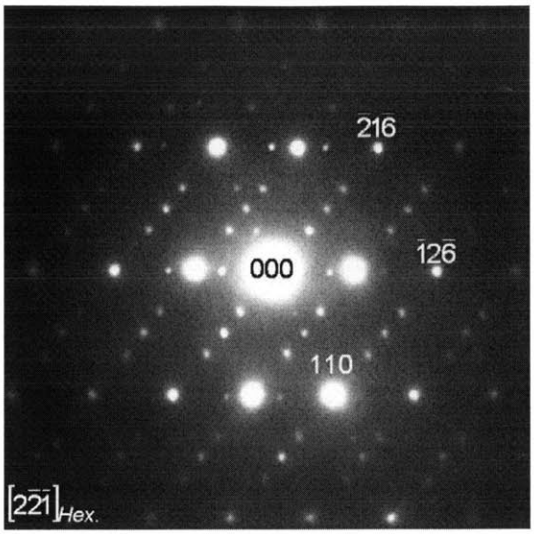
$\bar{2}16$
000
$\bar{1}2\bar{6}$
110
$[2\bar{2}\bar{1}]_{Hex.}$

4.5 V Charged $Li_{0.2}Ni_{0.5}Mn_{0.5}O_2$ Sample Cycled Between 4.5 V and 2.0 V for 2 Complete Cycles and 1 Additional Charge at C/50:

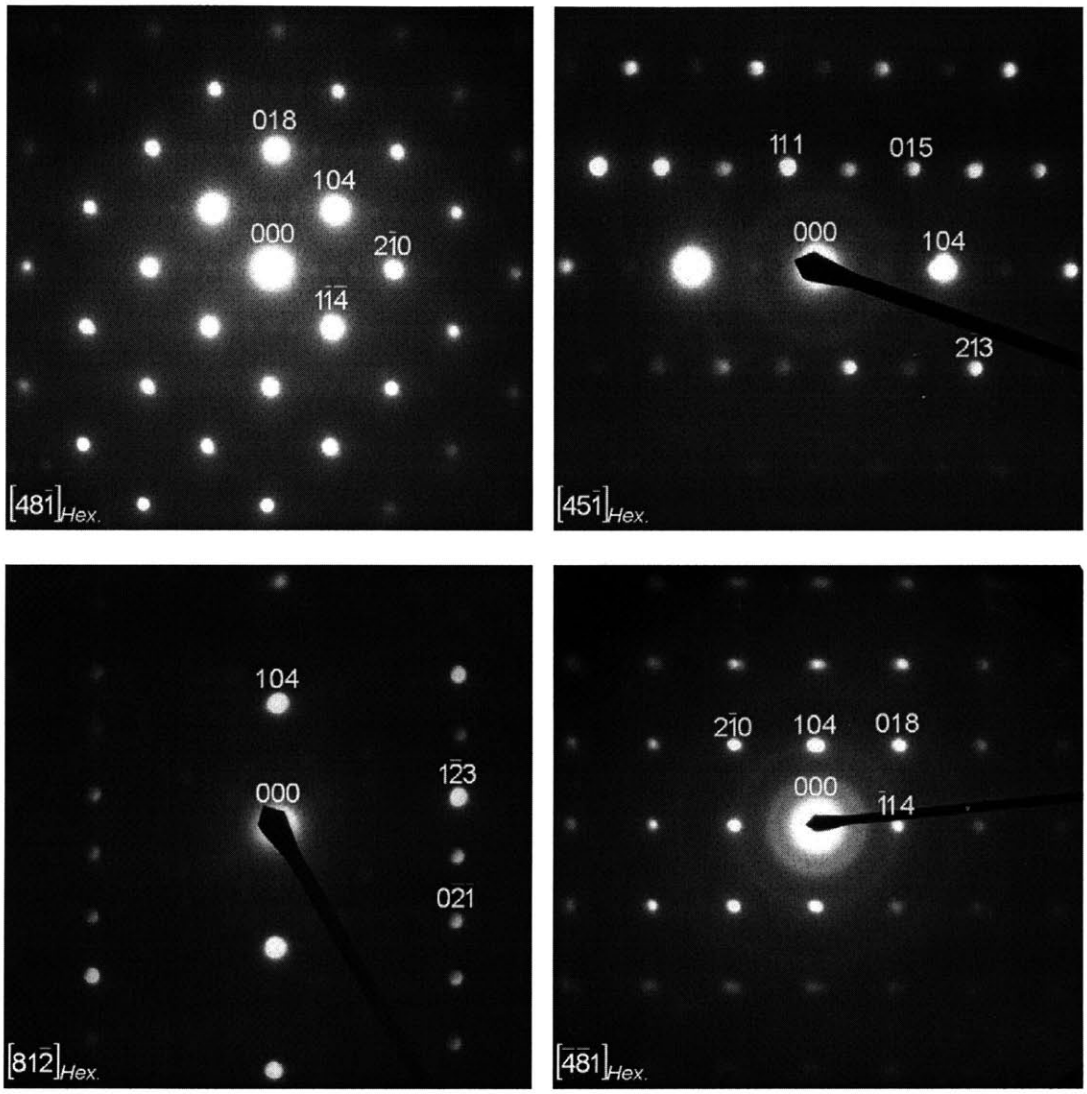

5.3 V Charged $Li_0Ni_{0.5}Mn_{0.5}O_2$ Sample Cycled Between 5.3 V and 2.0 V for 2 Complete Cycles and 1 Additional Charge at C/50:

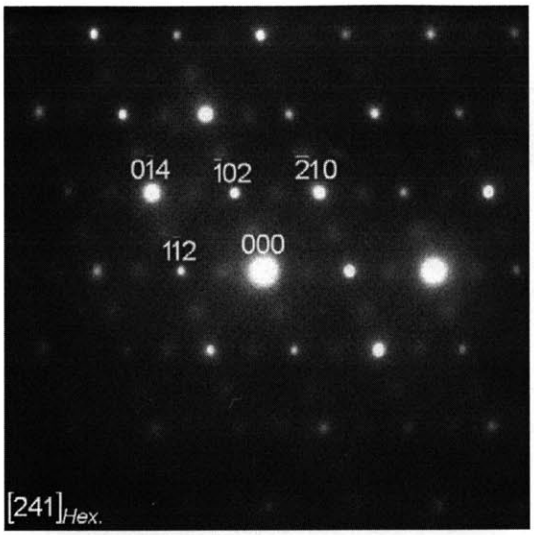

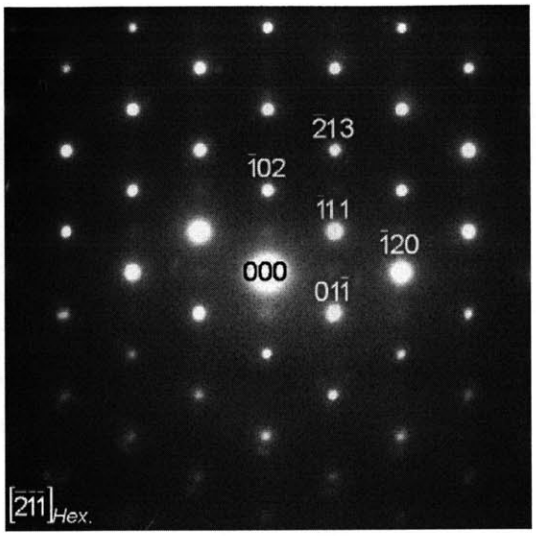

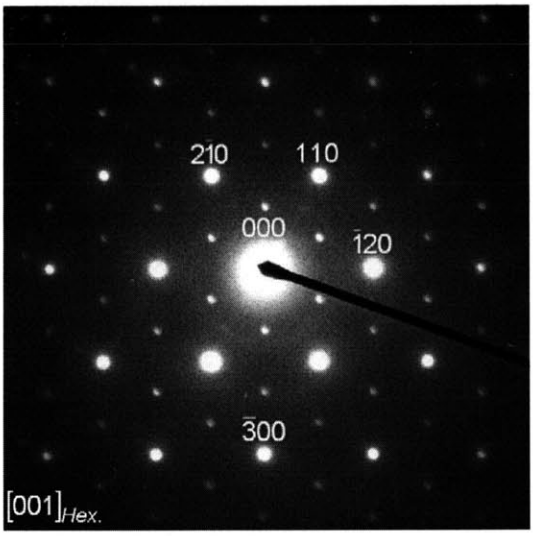

4.5 V Discharged $Li_{0.9}Ni_{0.5}Mn_{0.5}O_2$ Sample Cycled Between 4.5 V and 2.0 V for 5 Complete Cycles at C/50:

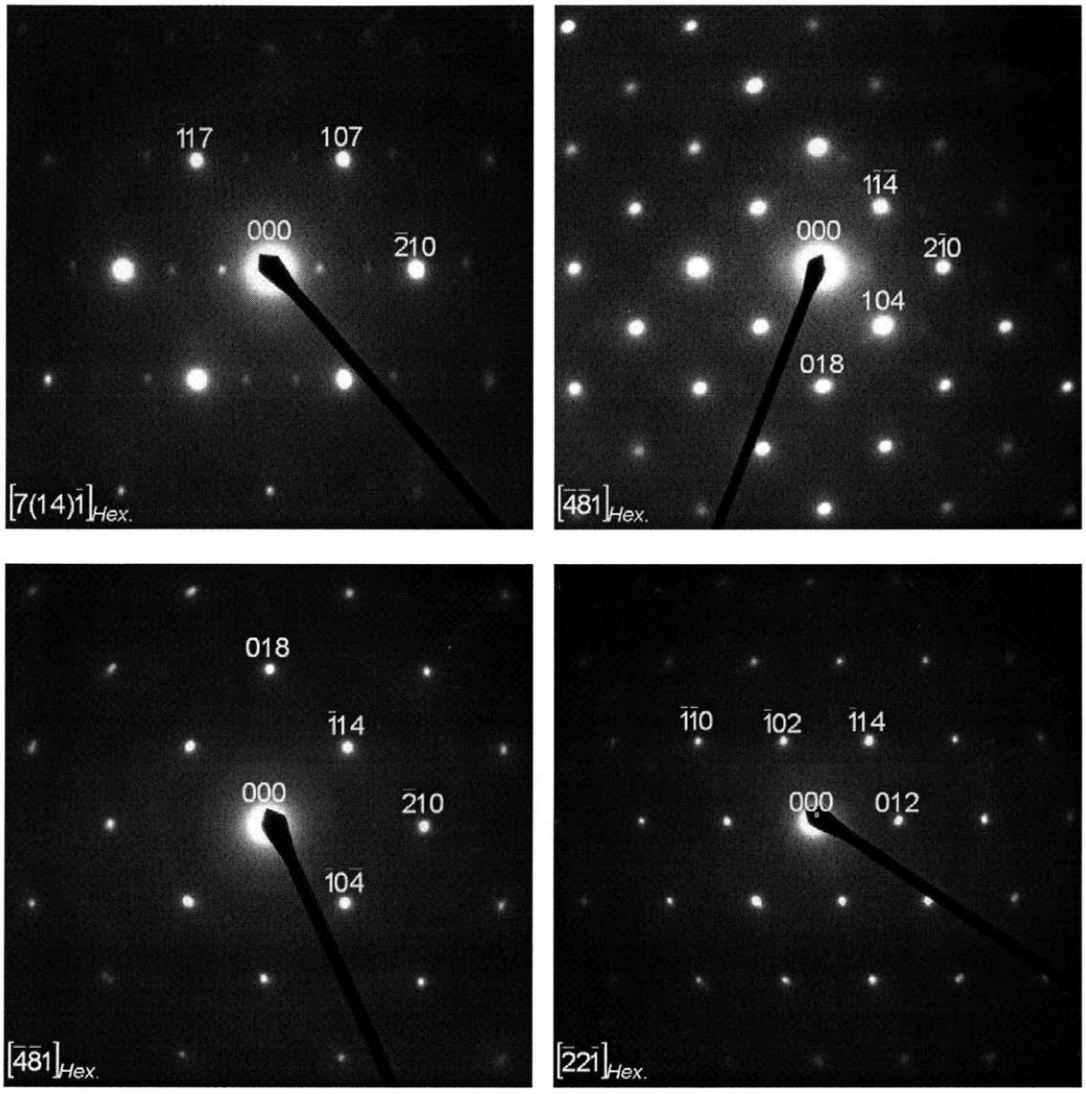

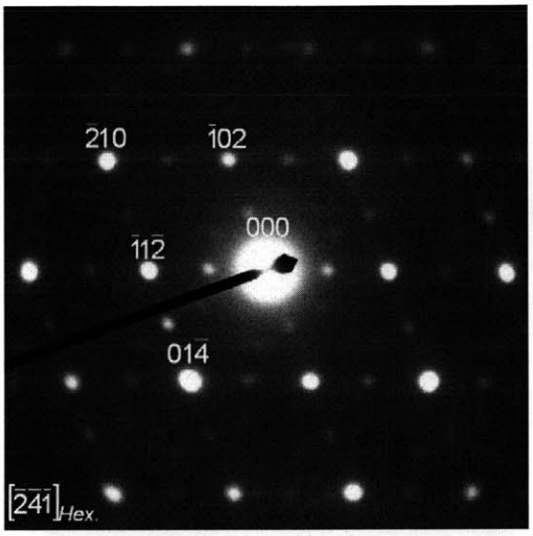
$\bar{2}10$
$\bar{1}02$
000
$\bar{1}1\bar{2}$
$01\bar{4}$
$[\bar{2}4\bar{1}]_{Hex.}$

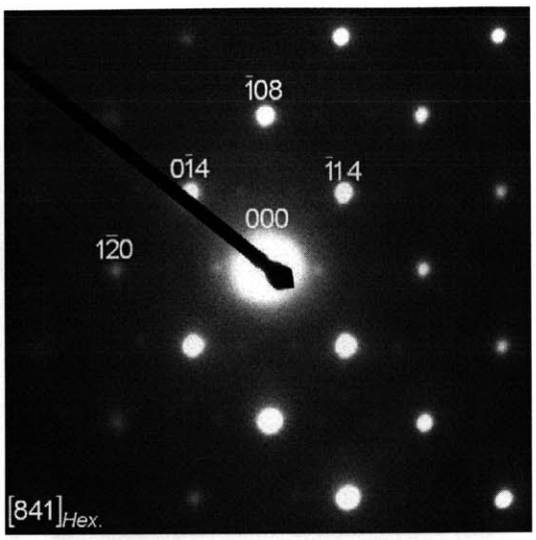
$\bar{1}08$
$01\bar{4}$
$\bar{1}14$
000
$1\bar{2}0$
$[841]_{Hex.}$

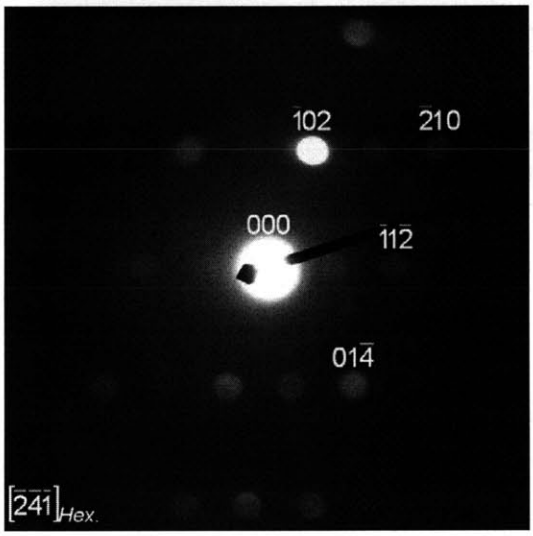
$\bar{1}02$
210
000
$\bar{1}1\bar{2}$
$01\bar{4}$
$[\bar{2}4\bar{1}]_{Hex.}$

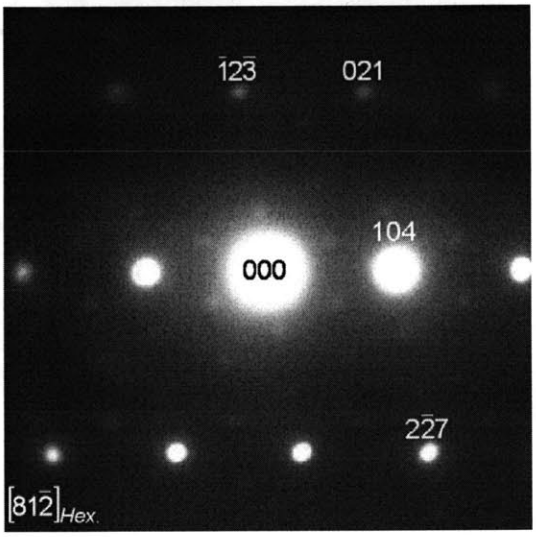
$\bar{1}2\bar{3}$
021
104
000
$2\bar{2}7$
$[81\bar{2}]_{Hex.}$

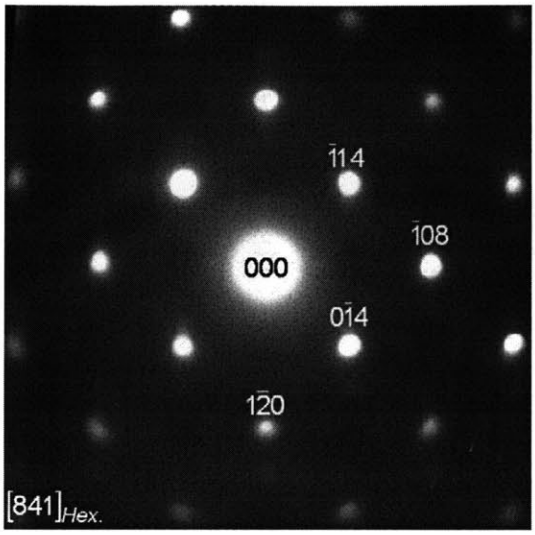
$\bar{1}14$
$\bar{1}08$
000
$0\bar{1}4$
$1\bar{2}0$
$[841]_{Hex.}$

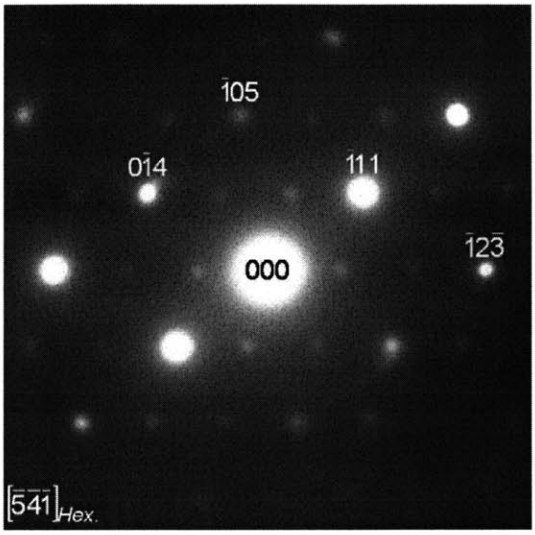
$\bar{1}05$
$0\bar{1}4$
$\bar{1}11$
$\bar{1}2\bar{3}$
000
$[\bar{5}\bar{4}\bar{1}]_{Hex.}$

5.3 V Discharged $Li_{x>0.76}Ni_{0.5}Mn_{0.5}O_2$ Sample Cycled Between 5.3 V and 2.0 V for 5 Complete Cycles at C/50:

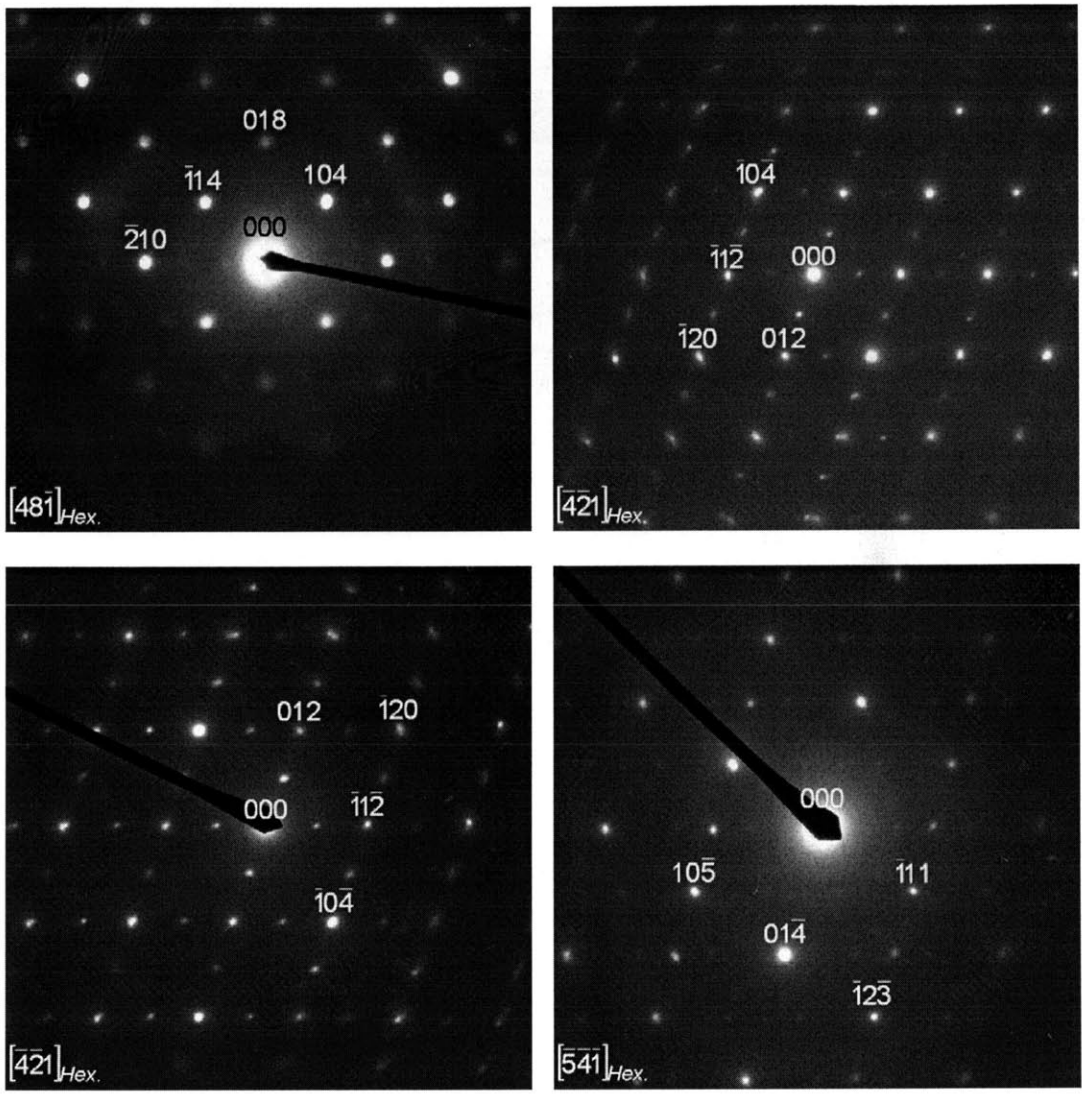

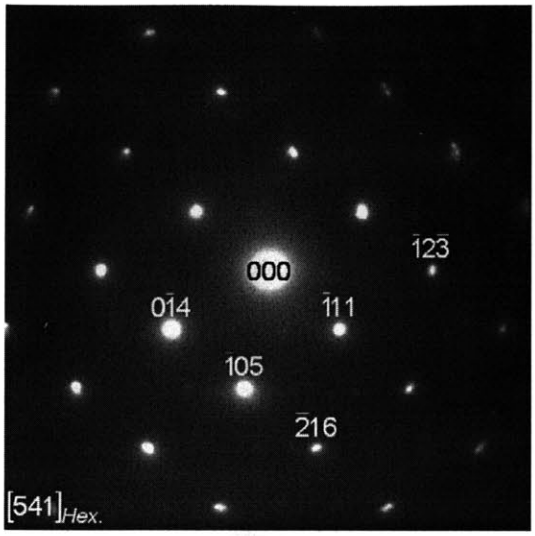
000
$\bar{1}\bar{2}\bar{3}$
$0\bar{1}4$
$\bar{1}11$
105
$\bar{2}16$
$[541]_{Hex.}$

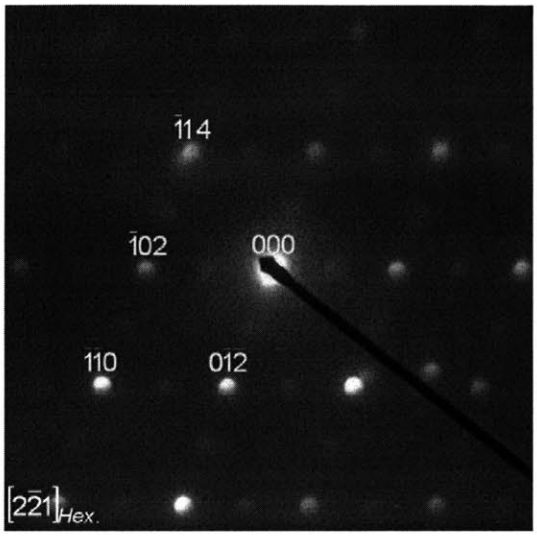
$\bar{1}14$
$\bar{1}02$
000
110
012
$[2\bar{2}\bar{1}]_{Hex.}$

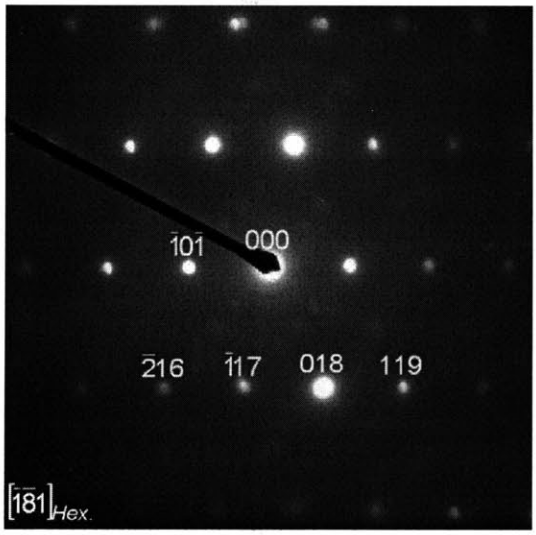
$\bar{1}0\bar{1}$
000
$\bar{2}16$
$\bar{1}17$
018
119
$[\bar{1}\bar{1}\bar{1}]_{Hex.}$

4.5 V Extensively Cycled $Li_{0.8}Ni_{0.5}Mn_{0.5}O_2$ Sample in the Discharged State Cycled Between 4.5 V and 2.0 V for 5 Cycles at C/50, 5 Cycles at C/20, 5 Cycles at C/5, 5 Cycles at C/2, and 1 Cycle at C/50:

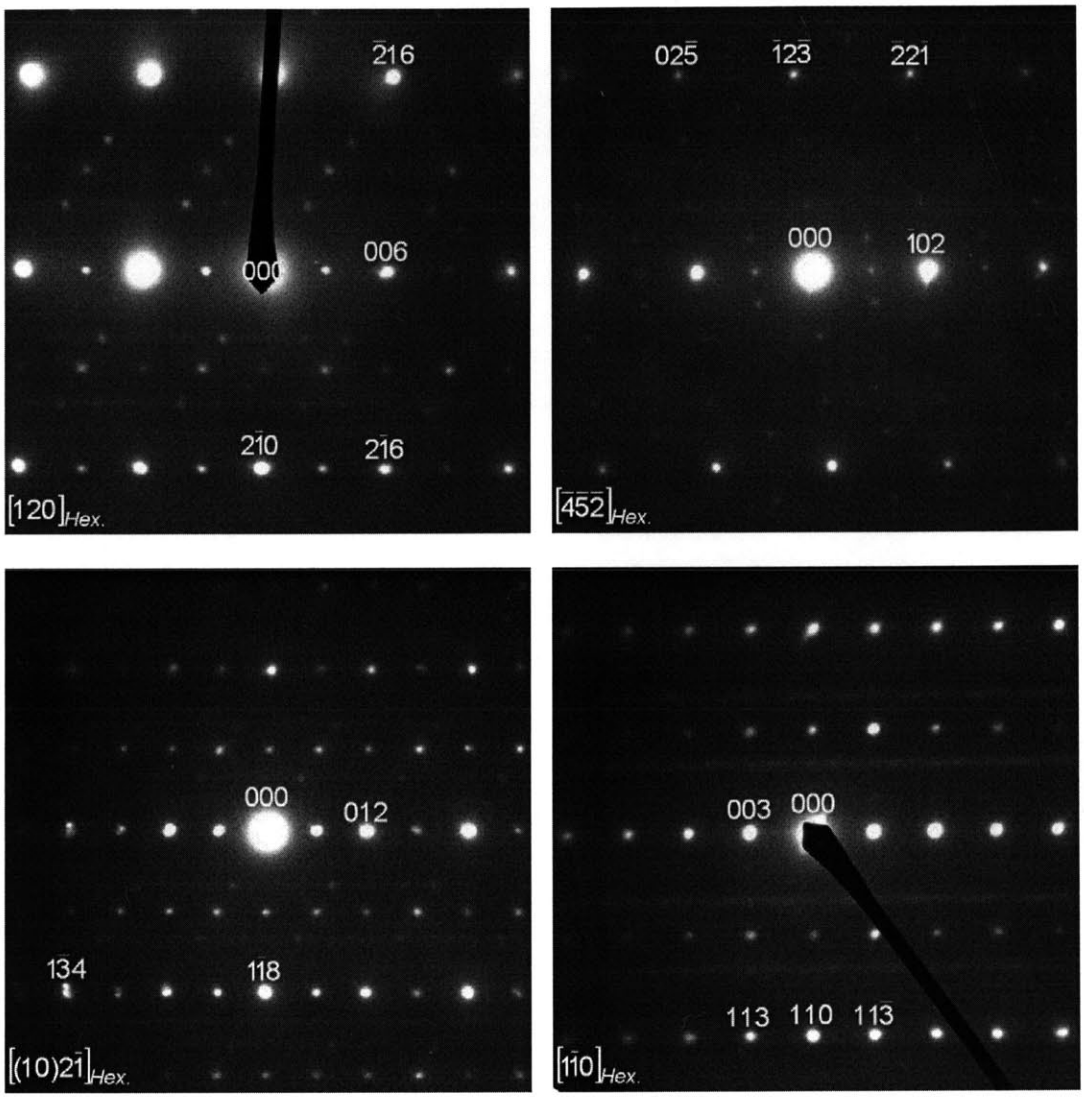

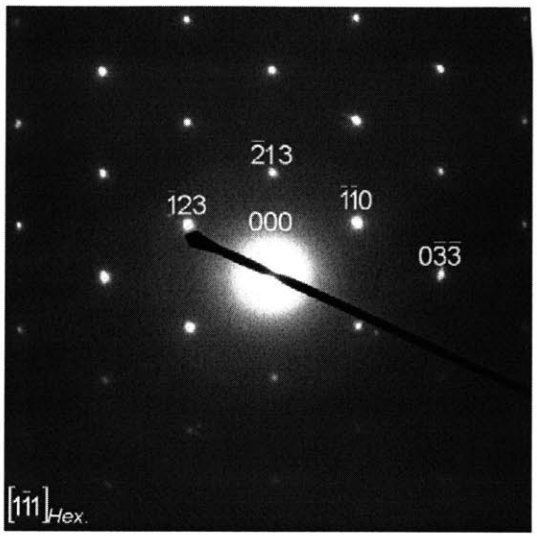
$\bar{2}13$
$\bar{1}23$
000
$\bar{1}\bar{1}0$
$0\bar{3}\bar{3}$
$[1\bar{1}1]_{Hex.}$